INSTITUTE OF PHYSICS PUBLISHING REPORTS ON PROGRESS IN PHYSICS

Rep. Prog. Phys. **70** (2007) 1–87 doi:10.1088/0034-4885/70/1/R01

Theory of surface plasmons and surface-plasmon polaritons

J M Pitarke[1,2], V M Silkin[2], E V Chulkov[2,3] and P M Echenique[2,3]

[1] Materia Kondentsatuaren Fisika Saila, Zientzi Fakultatea, Euskal Herriko Unibertsitatea, 644 Posta kutxatila, E-48080 Bilbo, Basque Country, Spain
[2] Donostia International Physics Center (DIPC) and Unidad de Física de Materiales CSIC-UPV/EHU, Manuel de Lardizabal Pasealekua, E-20018 Donostia, Basque Country, Spain
[3] Materialen Fisika Saila, Kimika Fakultatea, Euskal Herriko Unibertsitatea, 1072 Posta kutxatila, E-20080 Donostia, Basque Country, Spain

Received 2 August 2006, in final form 9 October 2006
Published 7 December 2006
Online at stacks.iop.org/RoPP/70/1

Abstract

Collective electronic excitations at metal surfaces are well known to play a key role in a wide spectrum of science, ranging from physics and materials science to biology. Here we focus on a theoretical description of the many-body dynamical electronic response of solids, which underlines the existence of various collective electronic excitations at metal surfaces, such as the conventional surface plasmon, multipole plasmons and the recently predicted acoustic surface plasmon. We also review existing calculations, experimental measurements and applications.

This article was invited by Professor M Finnis.

Contents

1. Introduction

In his pioneering treatment of characteristic energy losses of fast electrons passing through thin metal films, Ritchie predicted the existence of self-sustained collective excitations at metal surfaces [1]. It had already been pointed out by Pines and Bohm [2, 3] that the long-range nature of the Coulomb interaction between valence electrons in metals yields collective plasma oscillations similar to the electron-density oscillations observed by Tonks and Langmuir in electrical discharges in gases [4], thereby explaining early experiments by Ruthemann [5] and Lang [6] on the bombardment of thin metallic films by fast electrons. Ritchie investigated the impact of the film boundaries on the production of collective excitations and found that the boundary effect is to cause the appearance of a new *lowered* loss due to the excitation of *surface* collective oscillations [1]. Two years later, in a series of electron energy-loss experiments Powell and Swan [7] demonstrated the existence of these collective excitations, the quanta of which Stern and Ferrell called the *surface plasmon* [8].

Since then, there has been a significant advance in both theoretical and experimental investigations of surface plasmons, which for researches in the field of condensed matter and surface physics have played a key role in the interpretation of a great variety of experiments and the understanding of various fundamental properties of solids. These include the nature of Van der Waals forces [9–11], the classical image potential acting between a point classical charge and a metal surface [12–15], the energy transfer in gas–surface interactions [16], surface energies [17–19], the damping of surface vibrational modes [20, 21], the energy loss of charged particles moving outside a metal surface [22, 23] and the de-excitation of adsorbed molecules [24]. Surface plasmons have also been employed in a wide spectrum of studies ranging from electrochemistry [25], wetting [26] and biosensing [27–29] to scanning tunnelling microscopy [30], the ejection of ions from surfaces [31], nanoparticle growth [32, 33], surface-plasmon microscopy [34, 35] and surface-plasmon resonance technology [36–42]. Renewed interest in surface plasmons has come from recent advances in the investigation of the electromagnetic properties of nanostructured materials [43, 44], one of the most attractive aspects of these collective excitations now being their use to concentrate light in subwavelength structures and to enhance transmission through periodic arrays of subwavelength holes in optically thick metallic films [45, 46].

The so-called field of plasmonics represents an exciting new area for the application of surface and interface plasmons, an area in which surface-plasmon based circuits merge the fields of photonics and electronics at the nanoscale [47]. Indeed, surface-plasmon polaritons can serve as a basis for constructing nanoscale photonic circuits that will be able to carry optical signals and electric currents [48, 49]. Surface plasmons can also serve as a basis for the design, fabrication and characterization of subwavelength waveguide components [50–64]. In the framework of plasmonics, modulators and switches have also been investigated [65, 66], as well as the use of surface plasmons as mediators in the transfer of energy from donor to acceptors molecules on opposite sides of metal films [67].

According to the work of Pines and Bohm, the quantum energy collective plasma oscillations in a free electron gas with equilibrium density n is $\hbar\omega_{\rm p} = \hbar(4\pi ne^2/m_{\rm e})^{1/2}$, $\omega_{\rm p}$ being the so-called plasmon frequency[4]. In the presence of a planar boundary, there is a new mode (the *surface* plasmon), the frequency of which equals in the nonretarded region (where the speed of light can be taken to be infinitely large) Ritchie's frequency $\omega_{\rm s} = \omega_{\rm p}/\sqrt{2}$ at wave vectors $\boldsymbol{q}$ in the range $\omega_{\rm s}/c \ll q \ll q_{\rm F}$ ($q_{\rm F}$ being the magnitude of the Fermi wave

[4] The electron density n is usually characterized by the density parameter $r_{\rm s} = (3/4\pi n)^{1/3}/a_0$, a_0 being the Bohr radius, $a_0 = 0.529$ Å. In metals the electron-density parameter of valence electrons is typically in the range $2 < r_{\rm s} < 6$, which corresponds to plasmon energies on the order of 10 eV and frequencies that lie in the optical regime.

vector) and exhibits some dispersion as the wave vector is increased. In the retarded region, where the phase velocity ω_s/q of the surface plasmon is comparable to the velocity of light, surface plasmons couple with the free electromagnetic field. These surface-plasmon polaritons propagate along the metal surface with frequencies ranging from zero (at $q = 0$) towards the asymptotic value $\omega_s = \omega_p/\sqrt{2}$, the dispersion relation $\omega(q)$ lying to the right of the light line and the propagating vector being, therefore, larger than that of bare light waves of the same energy. Hence, surface-plasmon polaritons in an ideal semi-infinite medium are nonradiative in nature, i.e. cannot decay by emitting a photon and, conversely, light incident on an ideal surface cannot excite surface plasmons.

In the case of thin films, the electric fields of both surfaces interact. As a result, there are (i) *tangential* oscillations characterized by a symmetric disposition of charge deficiency or excess at opposing points on the two surfaces and (ii) *normal* oscillations in which an excess of charge density at a point on one surface is accompanied by a deficiency at the point directly across the thin film. The phase velocity of the *tangential* surface plasmon is always less than the speed of light, as it occurs in the case of a semi-infinite electron system. However, the phase velocity of *normal* oscillations may surpass that of light, thereby becoming a radiative surface plasmon that should be responsible for the emission of light [68]. This radiation was detected using electron beam bombardment of thin films of Ag, Mg and Al with thicknesses ranging between 500 and 1000 Å [69, 70]. More recently, light emission was observed in the ultraviolet from a metal–oxide–metal tunnel diode and was attributed to the excitation of the radiative surface plasmon [71].

Nonradiative surface plasmons in both thin and thick films can couple to electromagnetic radiation in the presence of surface roughness or a grating, as suggested by Teng and Stern [72]. Alternatively, prism coupling can be used to enhance the momentum of incident light, as demonstrated by Otto [73] and by Kretchmann and Raether [74]. Since then, this so-called attenuated reflection (ATR) method and variations upon it have been used by several workers in a large variety of applications [75–81].

During the last decades, there has also been a significant advance in our understanding of surface plasmons in the *nonretarded* regime. Ritchie [82] and Kanazawa [83] were the first to attack the problem of determining the dispersion $\omega(q)$ of the nonretarded surface plasmon. Bennett [84] used a hydrodynamical model with a continuous decrease of the electron density at the metal surface and found that a continuous electron-density variation yields two collective electronic excitations: Ritchie's surface plasmon at $\omega \sim \omega_s$, with a *negative* energy dispersion at low wave vectors, and an upper surface plasmon at higher energies. In the direction normal to the surface, the distribution of Ritchie's surface plasmon consists of a single peak, i.e. it has a *monopole* character; however, the charge distribution of the upper mode has a node, i.e. it has a *dipole* character and is usually called multipole surface plasmon.

Bennett's qualitative conclusions were generally confirmed by microscopic descriptions of the electron gas. On the one hand, Feibelman showed that in the long-wavelength limit the classical result $\omega_s = \omega_p/\sqrt{2}$ is correct for a semi-infinite plane-bounded electron gas, irrespective of the exact variation of the electron density in the neighbourhood of the surface [85]. On the other hand, explicit expressions for the *linear* momentum dispersion of the conventional monopole surface plasmon that are sensitive to the actual form of the electron-density fluctuation at the surface were derived by Harris and Griffin [86] using the equation of motion for the Wigner distribution function in the random-phase approximation (RPA) and by Flores and García-Moliner [87] solving Maxwell's equations in combination with an integration of the field components over the surface region. Quantitative RPA calculations of the linear dispersion of the monopole surface plasmon were carried out by several authors using the infinite-barrier model (IBM) of the surface [88], a step potential [89, 90], and the

more realistic Lang–Kohn [91] self-consistent surface potential [92]. Feibelman's calculations showed that for the typical electron densities in metals ($2 < r_s < 6$) the initial slope of the momentum dispersion of monopole surface plasmons of jellium surfaces is negative [92], as anticipated by Bennett [84].

Negative values of the momentum dispersion had been observed by high-energy electron transmission on uncharacterized Mg surfaces [93] and later by inelastic low-energy electron diffraction on the (100) and (111) surfaces of Al [94,95]. Nevertheless, Klos and Raether [96] and Krane and Raether [97] did not observe a negative dispersion for Mg and Al films. Conclusive experimental confirmation of the negative surface plasmon dispersion of a variety of simple metals (Li, Na, K, Cs, Al and Mg) did not come about until several years later [98–101], in a series of experiments based on angle-resolved low-energy inelastic electron scattering[5]. These experiments showed good agreement with self-consistent dynamical-response calculations carried out for a jellium surface[6] in a time-dependent adiabatic extension of the density-functional theory (DFT) of Hohenberg, Kohn and Sham [102]. Furthermore, these experiments also showed that the multipole surface plasmon was observable, its energy and dispersion being in quantitative agreement with the self-consistent jellium calculations that had been reported by Liebsch [103].

Significant deviations from the dispersion of surface plasmons at jellium surfaces occur on Ag [104–107] and Hg [108], due to the presence of filled 4d and 5d bands, respectively, which in the case of Ag yields an anomalous positive dispersion. In order to describe the observed features of Ag surface plasmons, various simplified models for the screening of d electrons have been developed [109–113]. Most recently, calculations have been found to yield a qualitative understanding of the existing electron energy-loss measurements by combining a self-consistent jellium model for valence 5s electrons with a so-called dipolium model in which the occupied 4d bands are represented in terms of polarizable spheres located at the sites of a semi-infinite face-cubic-centred (fcc) lattice [114].

Ab initio bulk calculations of the dynamical response and plasmon dispersions of *noble* metals with occupied d bands have been carried out recently [115–117]. However, first-principles calculations of the surface-plasmon energy and linewidth dispersion of real solids have been carried out only in the case of the simple-metal prototype surfaces Mg(0001) and Al(111) [118,119]. These calculations lead to an accurate description of the measured surface-plasmon energy dispersion that is superior to that obtained in the jellium model, and they show that the band structure is of paramount importance for a correct description of the surface-plasmon linewidth.

The multipole surface plasmon, which is originated in the selvage electronic structure at the surface, has been observed in a variety of simple metals at $\omega \sim 0.8\omega_p$ [98–101], in agreement with theoretical predictions. Nevertheless, electron energy-loss spectroscopy (EELS) measurements of Ag, Hg and Li revealed no clear evidence of the multipole surface plasmon. In the case of Ag, high-resolution energy-loss spectroscopy low-energy electron diffraction (ELS-LEED) measurements indicated that a peak was obtained at 3.72 eV by subtracting the data for two different impact energies [120], which was interpreted to be the Ag multipole plasmon. However, Liebsch argued that the frequency of the Ag multipole surface plasmon should be in the 6–8 eV range *above* rather than *below* the bulk plasma frequency and suggested that the observed peak at 3.72 eV might not be associated with a multipole surface plasmon [121].

[5] Since the finite angular acceptance of typical energy-loss spectrometers guarantees that the momentum transfer is associated with a plasmon wavelength larger than the wavelength of light at $\omega = \omega_s$ ($2\pi c/\omega_s \sim 10^3$ Å), only the nonretarded region is observed in these experiments.

[6] A jellium surface consists of a fixed uniform positive background occupying a halfspace plus a neutralizing cloud of interacting electrons.

An alternative spectroscopy technique to investigate multipole surface plasmons is provided by angle- and energy-resolved photoyield experiments (AERPY) [122]. In fact, AERPY is more suitable than electron energy-loss spectroscopy to identify the multipole surface plasmon, since the monopole surface plasmon of clean flat surfaces (which is the dominant feature in electron energy-loss spectra) is not excited by photons and thus the weaker multipole surface mode (which intersects the radiation line in the retardation regime) can be observed. A large increase in the surface photoyield was observed at $\omega = 0.8\omega_p$ from Al(100) [122] and Al(111) [123]. Recently, the surface electronic structure and optical response of Ag has been studied using this technique [124]. In these experiments, the Ag multipole surface plasmon is observed at 3.7 eV, while no signature of the multipole surface plasmon is observed above the plasma frequency ($\omega_p = 3.8$ eV) in disagreement with the existing theoretical prediction [121]. Hence, further theoretical work is needed on the surface electronic response of Ag that go beyond the s–d polarization model described in [121].

Another collective electronic excitation at metal surfaces is the so-called acoustic surface plasmon that has been predicted to exist at solid surfaces where a partially occupied quasi-two-dimensional surface-state band coexists with the underlying three-dimensional continuum [125, 126]. This *new* low-energy collective excitation exhibits linear dispersion at low wave vectors and might therefore affect electron–hole (e–h) and phonon dynamics near the Fermi level[7]. It has been demonstrated that it is a combination of the nonlocality of the 3D dynamical screening and the spill out of the 3D electron density into the vacuum which allows the formation of 2D electron-density acoustic oscillations at metal surfaces, since these oscillations would otherwise be completely screened by the surrounding 3D substrate [127]. This *novel* surface-plasmon mode has been observed recently at the (0001) surface of Be, showing a linear energy dispersion that is in very good agreement with first-principles calculations [128].

Finally, we note that metal–dielectric interfaces of arbitrary geometries also support charge density oscillations similar to the surface plasmons characteristic of planar interfaces. These are *localized* Mie plasmons occurring at frequencies which are characteristic of the interface geometry [129]. The excitation of localized plasmons on small particles has attracted great interest over the years in scanning transmission electron microscopy [130–135] and near-field optical spectroscopy [136]. Recently, new advances in structuring and manipulating on the nanometre scale have rekindled interest in this field [137]. In nanostructured metals and carbon-based structures, such as fullerenes and carbon nanotubes, localized plasmons can be excited by light and can therefore be easily detected as pronounced optical resonances [138–140]. Furthermore, very localized dipole and multipole modes in the vicinity of highly coupled structures are responsible for surface-enhanced Raman scattering [141, 142] and other striking properties like, for example, the blackness of colloidal silver [143].

Collective electronic excitations in thin adsorbed overlayers, semiconductor heterostructures, and parabolic quantum wells have also attracted attention over the last years. The adsorption of thin films is important, because of the drastic changes that they produce in the electronic properties of the substrate and also because of related phenomena such as catalytic promotion [144]; however, the understanding of adsorbate-induced collective excitations is still incomplete [145–152]. The excitation spectrum of collective modes in semiconductor quantum wells has been described by several authors [153–157]. These systems, which have been grown in semiconductor heterostructures with the aid of molecular beam epitaxy [158],

[7] The sound velocity of this acoustic mode is, however, close to the Fermi velocity of the 2D surface-state band, which is typically a few orders of magnitude larger than the sound velocity of acoustic phonons in metals but still about three orders of magnitude smaller than the velocity of light.

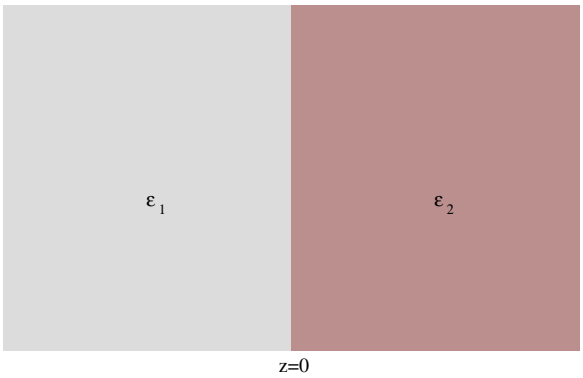

Figure 1. Two semi-infinite media with dielectric functions ϵ_1 and ϵ_2 separated by a planar interface at $z = 0$.

form a nearly ideal free-electron gas and have been, therefore, a playground on which to test existing many-body theories [159, 160].

Major reviews on the theory of collective electronic excitations at metal surfaces have been given by Ritchie [161], Feibelman [162] and Liebsch [163]. Experimental reviews are also available, which focus on high-energy EELS experiments [164], surface plasmons on smooth and rough surfaces and on gratings [165] and angle-resolved low-energy EELS investigations [166, 167]. An extensive review on plasmons and magnetoplasmons in semiconductor heterostructures has been given recently given by Kushwaha [168].

This review will focus on a unified theoretical description of the many-body dynamical electronic response of solids, which underlines the existence of various collective electronic excitations at metal surfaces, such as the conventional surface plasmon, multipole plasmons and the acoustic surface plasmon. We also review existing calculations, experimental measurements and some of the most recent applications including particle–solid interactions, scanning transmission electron microscopy and surface-plasmon based photonics, i.e. plasmonics.

2. Surface-plasmon polariton: classical approach

2.1. Semi-infinite system

2.1.1. The surface-plasmon condition. We consider a classical model consisting of two semi-infinite nonmagnetic media with local (frequency-dependent) dielectric functions ϵ_1 and ϵ_2 separated by a planar interface at $z = 0$ (see figure 1). The full set of Maxwell's equations in the absence of external sources can be expressed as follows [169]:

$$\boldsymbol{\nabla} \times \boldsymbol{H}_i = \epsilon_i \frac{1}{c} \frac{\partial}{\partial t} \boldsymbol{E}_i, \tag{2.1}$$

$$\boldsymbol{\nabla} \times \boldsymbol{E}_i = -\frac{1}{c} \frac{\partial}{\partial t} \boldsymbol{H}_i, \tag{2.2}$$

$$\boldsymbol{\nabla} \cdot (\epsilon_i \boldsymbol{E}_i) = 0 \tag{2.3}$$

and

$$\boldsymbol{\nabla} \cdot \boldsymbol{H}_i = 0, \tag{2.4}$$

where the index i describes the media: $i = 1$ at $z < 0$, and $i = 2$ at $z > 0$.

Solutions of equations (2.1)–(2.4) can generally be classified into s-polarized and p-polarized electromagnetic modes, the electric field $\boldsymbol{E}$ and the magnetic field $\boldsymbol{H}$ being parallel to the interface, respectively. For an ideal surface, if waves are to be formed that propagate along the interface there must necessarily be a component of the electric field normal to the surface. Hence, s-polarized surface oscillations (whose electric field $\boldsymbol{E}$ is parallel to the interface) do not exist; instead, we seek conditions under which a travelling wave with the magnetic field $\boldsymbol{H}$ parallel to the interface (p-polarized wave) may propagate along the surface ($z = 0$), with the fields tailing off into the positive ($z > 0$) and negative ($z < 0$) directions. Choosing the x-axis along the propagating direction, we write

$$\boldsymbol{E}_i = (E_{i_x}, 0, E_{i_z})\, \mathrm{e}^{-\kappa_i |z|}\, \mathrm{e}^{\mathrm{i}(q_i x - \omega t)} \tag{2.5}$$

and

$$\boldsymbol{H}_i = (0, E_{i_y}, 0)\, \mathrm{e}^{-\kappa_i |z|}\, \mathrm{e}^{\mathrm{i}(q_i x - \omega t)}, \tag{2.6}$$

where q_i represents the magnitude of a wave vector that is parallel to the surface. Introducing equations (2.5) and (2.6) into equations (2.1)–(2.4), one finds

$$\mathrm{i}\,\kappa_1\, H_{1_y} = +\frac{\omega}{c}\,\epsilon_1\, E_{1_x}, \tag{2.7}$$

$$\mathrm{i}\,\kappa_2\, H_{2_y} = -\frac{\omega}{c}\,\epsilon_2\, E_{2_x} \tag{2.8}$$

and

$$\kappa_i = \sqrt{q_i^2 - \epsilon_i\,\frac{\omega^2}{c^2}}. \tag{2.9}$$

The boundary conditions imply that the component of the electric and magnetic fields parallel to the surface must be continuous. Using equations (2.7) and (2.8), one writes the following system of equations:

$$\frac{\kappa_1}{\epsilon_1}\, H_{1_y} + \frac{\kappa_2}{\epsilon_2}\, H_{2_y} = 0 \tag{2.10}$$

and

$$H_{1_y} - H_{2_y} = 0, \tag{2.11}$$

which has a solution only if the determinant is zero, i.e.

$$\frac{\epsilon_1}{\kappa_1} + \frac{\epsilon_2}{\kappa_2} = 0. \tag{2.12}$$

This is the surface-plasmon condition.

From the boundary conditions also follows the continuity of the 2D wave vector $\boldsymbol{q}$ entering equation (2.9), i.e. $q_1 = q_2 = q$. Hence, the surface-plasmon condition (equation (2.12)) can also be expressed as follows [170]:

$$q(\omega) = \frac{\omega}{c}\sqrt{\frac{\epsilon_1\,\epsilon_2}{\epsilon_1 + \epsilon_2}}, \tag{2.13}$$

where ω/c represents the magnitude of the light wave vector. For a metal–dielectric interface with the dielectric characterized by ϵ_2, the solution $\omega(q)$ of equation (2.13) has slope equal to $c/\sqrt{\epsilon_2}$ at the point $q = 0$ and is a monotonic increasing function of q, which is always smaller than $c\,q/\sqrt{\epsilon_2}$ and for large q is asymptotic to the value given by the solution of

$$\epsilon_1 + \epsilon_2 = 0. \tag{2.14}$$

This is the *nonretarded* surface-plasmon condition (equation (2.12) with $\kappa_1 = \kappa_2 = q$), which is valid as long as the phase velocity ω/q is much smaller than the speed of light.

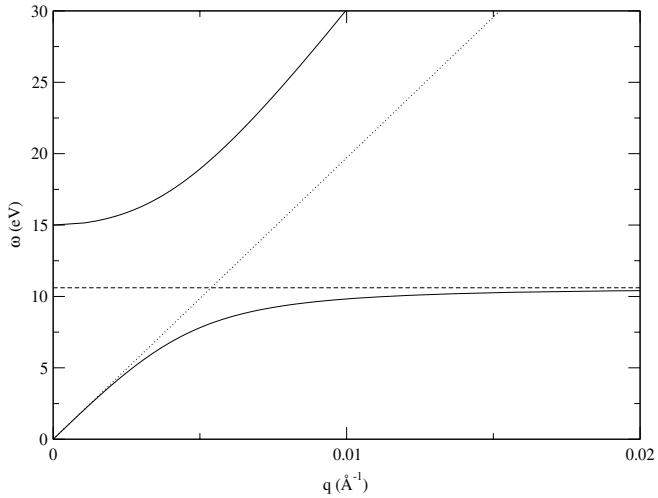

Figure 2. The solid lines represent the solutions of equation (2.16) with $\omega_p = 15$ eV: the dispersion of light in the solid (upper line) and the surface-plasmon polariton (lower line). In the retarded region ($q < \omega_s/c$), the surface-plasmon polariton dispersion curve approaches the light line $\omega = cq$ ($\cdots\cdots$). At short wave lengths ($q \gg \omega_s/c$), the surface-plasmon polariton approaches asymptotically the nonretarded surface-plasmon frequency $\omega_s = \omega_p/\sqrt{2}$ (- - - -).

2.1.2. Energy dispersion. In the case of a Drude semi-infinite metal in vacuum, one has $\epsilon_2 = 1$ and [171]

$$\epsilon_1 = 1 - \frac{\omega_p^2}{\omega(\omega + i\eta)}, \tag{2.15}$$

η being a positive infinitesimal. Hence, in this case equation (2.13) yields

$$q(\omega) = \frac{\omega}{c}\sqrt{\frac{\omega^2 - \omega_p^2}{2\omega^2 - \omega_p^2}}. \tag{2.16}$$

We have represented in figure 2 by solid lines the dispersion relation of equation (2.16), together with the light line $\omega = c\,q$ (dotted line). The upper solid line represents the dispersion of light in the solid. The lower solid line is the surface-plasmon polariton

$$\omega^2(q) = \omega_p^2/2 + c^2q^2 - \sqrt{\omega_p^4/4 + c^4q^4}, \tag{2.17}$$

which in the retarded region (where $q < \omega_s/c$) couples with the free electromagnetic field and in the nonretarded limit ($q \gg \omega_s/c$) yields the *classical* nondispersive surface-plasmon frequency $\omega_s = \omega_p/\sqrt{2}$.

We note that the wave vector $\boldsymbol{q}$ entering the dispersion relation of equation (2.17) (lower solid line of figure 2) is a 2D wave vector in the plane of the surface. Hence, if light hits the surface in an arbitrary direction the external radiation dispersion line will always lie somewhere between the light line $c\,q$ and the vertical line, in such a way that it will not intersect the surface-plasmon polariton line, i.e. light incident on an ideal surface cannot excite surface plasmons. Nevertheless, there are two mechanisms that allow external radiation to be coupled to surface-plasmon polaritons: surface roughness or gratings, which can provide the requisite momentum via *umklapp* processes [72], and attenuated total reflection (ATR) which provides the external radiation with an imaginary wave vector in the direction perpendicular to the surface [73, 74].

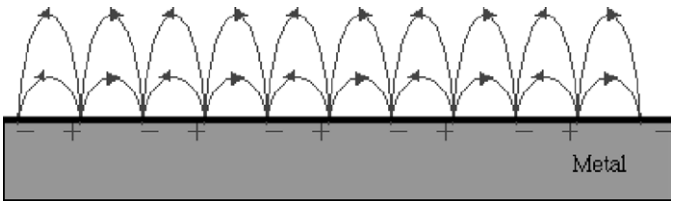

Figure 3. Schematic representation of the electromagnetic field associated with a surface-plasmon polariton propagating along a metal–dielectric interface. The field strength $\boldsymbol{E}_i$ (see equation (2.5)) decreases exponentially with the distance $|z|$ from the surface, the decay constant κ_i being given by equation (2.18). + and − represent the regions with lower and higher electron density, respectively.

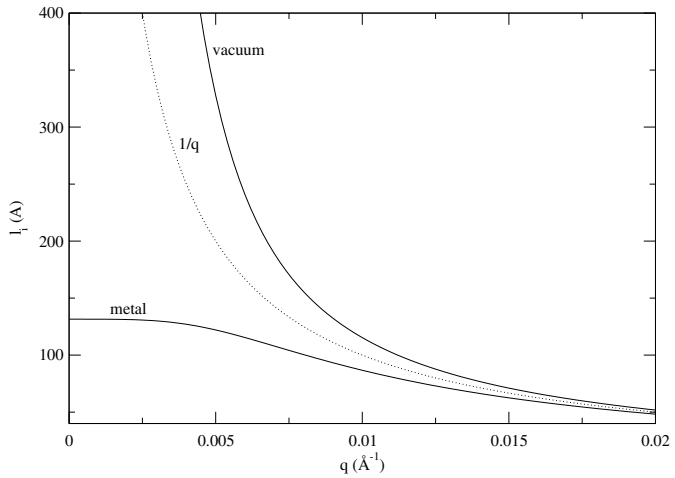

Figure 4. Attenuation length $l_i = 1/\kappa_i$, versus q, as obtained from equation (2.18) at the surface-plasmon polariton condition (equation (2.17)) for a Drude metal in vacuum. ϵ_1 has been taken to be of the form of equation (2.15) with $\omega_p = 15\,\text{eV}$ and ϵ_2 has been set up to unity. The dotted line represents the large-q limit of both l_1 and l_2, i.e. $1/q$.

2.1.3. Skin depth. Finally, we look at the spatial extension of the electromagnetic field associated with the surface-plasmon polariton (see figure 3). Introducing the surface-plasmon condition of equation (2.13) into equation (2.9) (with $q_1 = q_2 = q$), one finds the following expression for the surface-plasmon decay constant κ_i perpendicular to the interface:

$$\kappa_i = \frac{\omega}{c}\sqrt{\frac{-\epsilon_i^2}{\epsilon_1 + \epsilon_2}}, \tag{2.18}$$

which allows to define the attenuation length $l_i = 1/\kappa_i$ at which the electromagnetic field falls to 1/e. Figure 4 shows l_i as a function of the magnitude q of the surface-plasmon polariton wave vector for a Drude metal [ϵ_1 of equation (2.15)] in vacuum ($\epsilon_2 = 1$). In the vacuum side of the interface, the attenuation length is over the wavelength involved ($l_2 > 1/q$), whereas the attenuation length into the metal is determined at long-wavelengths ($q \to 0$) by the so-called skin depth. At large q (where the nonretarded surface-plasmon condition of equation (2.14) is fulfilled), the skin depth is $l_i \sim 1/q$ thereby leading to a strong concentration of the electromagnetic surface-plasmon field near the interface.

2.2. *Thin films*

Thin films are also known to support surface collective oscillations. For this geometry, the electromagnetic fields of both surfaces interact in such a way that the *retarded* surface-plasmon condition of equation (2.12) splits into two new conditions (we only consider nonradiative surface plasmons), depending on whether electrons in the two surfaces oscillate in phase or not. In the case of a thin film of thickness a and dielectric function ϵ_1 in a medium of dielectric function ϵ_2, one finds [165]:

$$\frac{\epsilon_1}{\kappa_1 \tanh(\kappa_1 a/2)} + \frac{\epsilon_2}{\kappa_2} = 0 \tag{2.19}$$

and

$$\frac{\epsilon_1}{\kappa_1 \coth(\kappa_1 a/2)} + \frac{\epsilon_2}{\kappa_2} = 0. \tag{2.20}$$

Instead, if the film is surrounded by dielectric layers of dielectric constant ϵ_0 and equal thickness t on either side, one finds

$$\frac{\epsilon_1}{\kappa_1 \nu \tanh(\kappa_1 a/2)} + \frac{\epsilon_0}{\kappa_0} = 0 \tag{2.21}$$

and

$$\frac{\epsilon_1}{\kappa_1 \nu \coth(\kappa_1 a/2)} + \frac{\epsilon_0}{\kappa_0} = 0, \tag{2.22}$$

where

$$\nu = \frac{1 - \Delta\, \mathrm{e}^{-2\kappa_0 t}}{1 + \Delta\, \mathrm{e}^{-2\kappa_0 t}}, \tag{2.23}$$

with

$$\Delta = \frac{\kappa_2 \epsilon_0 - \kappa_0 \epsilon_2}{\kappa_2 \epsilon_0 + \kappa_0 \epsilon_2} \tag{2.24}$$

and

$$\kappa_0 = \sqrt{q^2 - \epsilon_0 \frac{\omega^2}{c^2}}. \tag{2.25}$$

Electron spectrometry measurements of the dispersion of the surface-plasmon polariton in oxidized Al films were reported by Pettit *et al* [172], spanning the energy range from the short-wavelength limit where $\omega \sim \omega_{\mathrm{p}}/\sqrt{2}$ all the way to the long-wavelength limit where $\omega \sim c\,q$. The agreement between the experimental measurements and the prediction of equations (2.21)–(2.25) (with a Drude dielectric function for the Al film and a dielectric constant $\epsilon_0 = 4$ for the surrounding oxide) is found to be very good, as shown in figure 5.

In the nonretarded regime ($q \gg \omega_{\mathrm{s}}/c$), where $\kappa_1 = \kappa_2 = q$, equations (2.19) and (2.20) take the form

$$\frac{\epsilon_1 + \epsilon_2}{\epsilon_1 - \epsilon_2} = \mp \mathrm{e}^{-qa}, \tag{2.26}$$

which for a Drude thin slab (ϵ_1 of equation (2.15)) in vacuum ($\epsilon_2 = 1$) yields [1]

$$\omega = \frac{\omega_{\mathrm{p}}}{\sqrt{2}} (1 \pm \mathrm{e}^{-qa})^{1/2}. \tag{2.27}$$

This equation has two limiting cases, as discussed by Ferrell [68]. At short wavelengths ($qa \gg 1$), the surface waves become decoupled and each surface sustains independent oscillations at the reduced frequency $\omega_{\mathrm{s}} = \omega_{\mathrm{p}}/\sqrt{2}$ characteristic of a semi-infinite electron gas

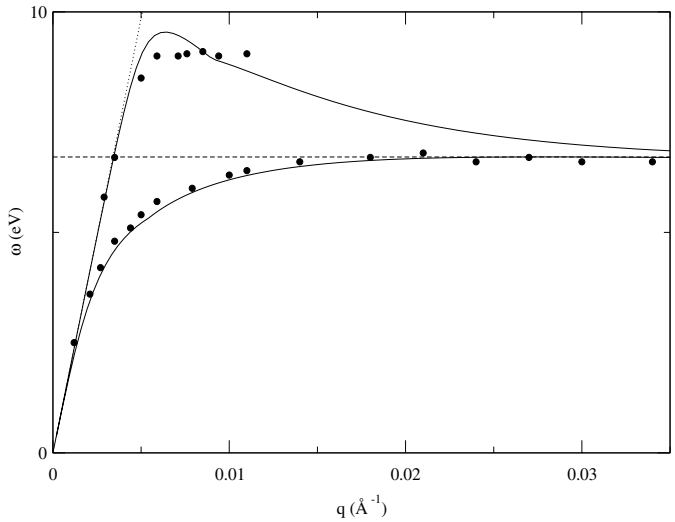

Figure 5. Dispersion $\omega(q)$ of the surface-plasmon polariton of an Al film of thickness $a = 120$ Å surrounded by dielectric layers of equal thickness $t = 40$ Å. The solid lines represent the result obtained from equations (2.21)–(2.25) with $\epsilon_2 = 1$, $\epsilon_0 = 4$ and a frequency-dependent Drude dielectric function ϵ_1 (see equation (2.15)) with $\omega_p = 15\,\text{eV}$ and $\eta = 0.75\,\text{eV}$[8]. The solid circles represent the electron spectrometry measurements reported by Petit *et al* [172]. The dashed line represents the nonretarded surface-plasmon frequency $\omega_p/\sqrt{5}$, which is the solution of equation (2.14) with $\epsilon_2 = 4$ and a Drude dielectric function ϵ_1. The dotted line represents the light line $\omega = cq$.

with a single plane boundary. At long wavelengths ($qa \ll 1$), there are *normal* oscillations at ω_p and *tangential* 2D oscillations at

$$\omega_{2D} = (2\pi naq)^{1/2}, \tag{2.28}$$

which were later discussed by Stern [173] and observed in artificially structured semiconductors [174] and more recently in a metallic surface-state band on a silicon surface [175].

3. Nonretarded surface plasmon: simplified models

The classical picture leading to the retarded equation (2.12) and nonretarded equation (2.14) ignores both the nonlocality of the electronic response of the system and the microscopic spatial distribution of the electron density near the surface. This microscopic effects can generally be ignored at long wavelengths where $q \ll q_F$; however, as the excitation wavelength approaches atomic dimensions nonlocal effects can be important.

As nonlocal effects can generally be ignored in the retarded region where $q < \omega_s/c$ (since $\omega_s/c \ll q_F$), here we focus our attention on the nonretarded regime where $\omega_s/c < q$. In this regime and in the absence of external sources, the ω-components of the time-dependent electric and displacement fields associated with collective oscillations at a metal surface satisfy

[8] Although in the case of an ideal damping-free electron gas the quantity η entering the Drude dielectric function of equation (2.15) should be a positive infinitesimal, a phenomenological finite parameter η is usually introduced in order to account for the actual electron damping occurring in real solids.

the quasi-static Maxwell's equations

$$\boldsymbol{\nabla} \cdot \boldsymbol{E}(\boldsymbol{r}, \omega) = -4\pi\, \delta n(\boldsymbol{r}, \omega), \tag{3.1}$$

or, equivalently,

$$\nabla^2 \phi(\boldsymbol{r}, \omega) = 4\pi\, \delta n(\boldsymbol{r}, \omega) \tag{3.2}$$

and

$$\boldsymbol{\nabla} \cdot \boldsymbol{D}(\boldsymbol{r}, \omega) = 0, \tag{3.3}$$

$\delta n(\boldsymbol{r}, \omega)$ being the fluctuating electron density associated with the surface plasmon and $\phi(\boldsymbol{r}, \omega)$ being the ω component of the time-dependent scalar potential.

3.1. Planar surface plasmon

3.1.1. Classical model. In the classical limit, we consider two semi-infinite media with local (frequency-dependent) dielectric functions ϵ_1 and ϵ_2 separated by a planar interface at $z = 0$, as in section 2.1 (see figure 1). In this case, the fluctuating electron density $\delta n(\boldsymbol{r}, \omega)$ corresponds to a delta-function sheet at $z = 0$:

$$\delta n(\boldsymbol{r}, \omega) = \delta n(\boldsymbol{r}_\parallel, \omega)\, \delta(z), \tag{3.4}$$

where $\boldsymbol{r}_\parallel$ defines the position vector in the surface plane, and the displacement field $\boldsymbol{D}(\boldsymbol{r}, \omega)$ takes the following form:

$$\boldsymbol{D}(\boldsymbol{r}, \omega) = \begin{cases} \epsilon_1\, \boldsymbol{E}(\boldsymbol{r}, \omega), & z < 0, \\ \\ \epsilon_2\, \boldsymbol{E}(\boldsymbol{r}, \omega), & z > 0. \end{cases} \tag{3.5}$$

Introducing equation (3.4) into equation (3.2), one finds that self-sustained solutions of Poisson's equation take the form

$$\phi(\boldsymbol{r}, \omega) = \phi_0\, \mathrm{e}^{\boldsymbol{q}\cdot\boldsymbol{r}_\parallel}\, \mathrm{e}^{-q|z|}, \tag{3.6}$$

where $\boldsymbol{q}$ is a 2D wave vector in the plane of the surface, and $q = |\boldsymbol{q}|$. A combination of equations (3.3), (3.5) and (3.6) with $\boldsymbol{E}(\boldsymbol{r}, \omega) = -\boldsymbol{\nabla}\phi(\boldsymbol{r}, \omega)$ yields the *nonretarded* surface-plasmon condition of equation (2.14), i.e.

$$\epsilon_1 + \epsilon_2 = 0. \tag{3.7}$$

3.1.2. Nonlocal corrections. Now we consider a more realistic *jellium* model of the solid surface consisting of a fixed semi-infinite uniform positive background at $z \leqslant 0$ plus a neutralizing *nonuniform* cloud of interacting electrons. Within this model, there is translational invariance in the plane of the surface; hence, we can define 2D Fourier transforms $\boldsymbol{E}(z; q, \omega)$ and $\boldsymbol{D}(z; q, \omega)$, the most general linear relation between them being

$$\boldsymbol{D}(z; q, \omega) = \int \mathrm{d}z' \boldsymbol{\epsilon}(z, z'; q, \omega) \cdot \boldsymbol{E}(z'; q, \omega), \tag{3.8}$$

where the tensor $\boldsymbol{\epsilon}(z, z'; q, \omega)$ represents the dielectric function of the medium.

In order to avoid an explicit calculation of $\boldsymbol{\epsilon}(z, z'; q, \omega)$, one can assume that far from the surface and at low wave vectors (but still in the nonretarded regime, i.e. $\omega_\mathrm{s}/c < q < q_\mathrm{F}$) equation (3.8) reduces to an expression of the form of equation (3.5):

$$\boldsymbol{D}(z; q, \omega) = \begin{cases} \epsilon_1\, \boldsymbol{E}(z; q, \omega), & z < z_1, \\ \\ \epsilon_2\, \boldsymbol{E}(z; q, \omega), & z > z_2, \end{cases} \tag{3.9}$$

where $z_1 \ll 0$ and $z_2 \gg 0$. Equations (3.2) and (3.3) with $\boldsymbol{E}(\boldsymbol{r},\omega) = -\boldsymbol{\nabla}\phi(\boldsymbol{r},\omega)$ then yield the following integration of the field components E_z and D_x in terms of the potential $\phi(z)$ at z_1 and z_2 [where it reduces to the classical potential of equation (3.6)]:

$$\int_{z_1}^{z_2} \mathrm{d}z\, E_z(z;q,\omega) = \phi(z_2;q,\omega) - \phi(z_1;q,\omega) \tag{3.10}$$

and

$$-\,\mathrm{i}\int_{z_1}^{z_2} \mathrm{d}z\, D_z(z;q,\omega) = \epsilon_2\,\phi(z_2;q,\omega) - \epsilon_1\,\phi(z_1;q,\omega). \tag{3.11}$$

Neglecting quadratic and higher-order terms in the wave vector, equations (3.10) and (3.11) are found to be compatible under the surface-plasmon condition [87]

$$\frac{\epsilon_1+\epsilon_2}{\epsilon_1-\epsilon_2} = q[d_\perp(\omega) - d_\parallel(\omega)], \tag{3.12}$$

$d_\perp(\omega)$ and $d_\parallel(\omega)$ being the so-called d-parameters introduced by Feibelman [162]:

$$d_\perp(\omega) = \int \mathrm{d}z\, z\,\frac{\mathrm{d}}{\mathrm{d}z}E_z(z,\omega) \Big/ \int \mathrm{d}z\,\frac{\mathrm{d}}{\mathrm{d}z}E_z(z,\omega) = \int \mathrm{d}z\, z\,\delta n(z,\omega) \Big/ \int \mathrm{d}z\,\delta n(z,\omega) \tag{3.13}$$

and

$$d_\parallel(\omega) = \int \mathrm{d}z\, z\,\frac{\mathrm{d}}{\mathrm{d}z}D_z(z,\omega) \Big/ \int \mathrm{d}z\,\frac{\mathrm{d}}{\mathrm{d}z}D_z(z,\omega), \tag{3.14}$$

where $E_z(z,\omega)$, $D_x(z,\omega)$ and $\delta n(z,\omega)$ represent the fields and the induced density evaluated in the $q \to 0$ limit.

For a Drude semi-infinite metal in vacuum [$\epsilon_2 = 1$ and equation (2.15) for ϵ_1], the nonretarded surface-plasmon condition of equation (3.12) yields the nonretarded dispersion relation

$$\omega = \omega_\mathrm{s}\{1 - q\mathrm{Re}[d_\perp(\omega_\mathrm{s}) - d_\parallel(\omega_\mathrm{s})]/2 + \ldots\}, \tag{3.15}$$

where ω_s is Ritchie's frequency: $\omega_\mathrm{s} = \omega_\mathrm{p}/\sqrt{2}$. For neutral jellium surfaces, $d_\parallel(\omega)$ coincides with the jellium edge and the linear coefficient of the surface-plasmon dispersion $\omega(q)$, therefore, only depends on the position $d_\perp(\omega_\mathrm{s})$ of the centroid of the induced electron density at ω_s (see equation (3.13)) with respect to the jellium edge.

3.1.3. Hydrodynamic approximation. In a hydrodynamic model, the collective motion of electrons in an arbitrary inhomogeneous system is expressed in terms of the electron density $n(\boldsymbol{r},t)$ and the hydrodynamical velocity $\boldsymbol{v}(\boldsymbol{r},t)$, which assuming irrotational flow we express as the gradient of a velocity potential $\psi(\boldsymbol{r},t)$ such that $\boldsymbol{v}(\boldsymbol{r},t) = -\boldsymbol{\nabla}\psi(\boldsymbol{r},t)$. First of all, one writes the basic hydrodynamic Bloch's equations (the continuity equation and the Bernoulli's equation) in the absence of external sources [176]:

$$\frac{\mathrm{d}}{\mathrm{d}t}n(\boldsymbol{r},t) = \boldsymbol{\nabla}\cdot[n(\boldsymbol{r},t)\,\boldsymbol{\nabla}\psi(\boldsymbol{r},t)] \tag{3.16}$$

and

$$\frac{\mathrm{d}}{\mathrm{d}t}\psi(\boldsymbol{r},t) = \frac{1}{2}\,|\boldsymbol{\nabla}\psi(\boldsymbol{r},t)|^2 + \frac{\delta G[n]}{\delta n} + \phi(\boldsymbol{r},t), \tag{3.17}$$

and Poisson's equation:

$$\nabla^2\phi(\boldsymbol{r},t) = 4\pi\, n(\boldsymbol{r},t), \tag{3.18}$$

where $G[n]$ is the internal kinetic energy, which is typically approximated by the Thomas–Fermi functional

$$G[n] = \frac{3}{10}\,(3\pi^2)^{2/3}\,[n(\boldsymbol{r},t)]^{5/3}\,. \tag{3.19}$$

The hydrodynamic equations (equations (3.16)–(3.18)) are nonlinear equations, difficult to solve. Therefore, one typically uses perturbation theory to expand the electron density and the velocity potential as follows:

$$n(\boldsymbol{r},t) = n_0(\boldsymbol{r}) + n_1(\boldsymbol{r},t) + \ldots \tag{3.20}$$

and

$$\psi(\boldsymbol{r},t) = 0 + \psi_1(\boldsymbol{r},t) + \ldots, \tag{3.21}$$

so that equations (3.16)–(3.18) yield the linearized hydrodynamic equations

$$\frac{\mathrm{d}}{\mathrm{d}t} n_1(\boldsymbol{r},t) = \boldsymbol{\nabla}\cdot[n_0(\boldsymbol{r})\,\boldsymbol{\nabla}\psi_1(\boldsymbol{r},t)], \tag{3.22}$$

$$\frac{\mathrm{d}}{\mathrm{d}t}\psi_1(\boldsymbol{r},t) = [\beta(\boldsymbol{r})]^2\,\frac{n_1(\boldsymbol{r},t)}{n_0(\boldsymbol{r})} + \phi_1(\boldsymbol{r},t), \tag{3.23}$$

and

$$\nabla^2\phi_1(\boldsymbol{r},t) = 4\pi\, n_1(\boldsymbol{r},t), \tag{3.24}$$

where $n_0(\boldsymbol{r})$ is the unperturbed electron density and $\beta(\boldsymbol{r}) = \sqrt{1/3}\,[3\pi^2 n_0(\boldsymbol{r})]^{1/3}$ represents the speed of propagation of hydrodynamic disturbances in the electron system[9].

We now consider a semi-infinite metal in vacuum consisting of an abrupt step of the unperturbed electron density at the interface, which we choose to be located at $z = 0$:

$$n_0(z) = \begin{cases} \bar{n}, & z \leqslant 0, \\ \\ 0, & z > 0. \end{cases} \tag{3.25}$$

Hence, within this model $n_0(\boldsymbol{r})$ and $\beta(\boldsymbol{r})$ are constant at $z \leqslant 0$ and vanish at $z > 0$.

Introducing Fourier transforms, equations (3.22)–(3.25) yield the basic differential equation for the plasma normal modes at $z \leqslant 0$:

$$\nabla^2(\omega^2 - \omega_{\mathrm{p}}^2 + \beta^2\nabla^2)\psi_1(\boldsymbol{r},\omega) = 0 \qquad (z \leqslant 0) \tag{3.26}$$

and Laplace's equation at $z > 0$:

$$\nabla^2\phi_1(\boldsymbol{r},\omega) = 0 \qquad (z > 0), \tag{3.27}$$

where both $n_1(\boldsymbol{r},\omega)$ and $\psi_1(\boldsymbol{r},\omega)$ vanish. Furthermore, translational invariance in the plane of the surface allows to introduce the 2D Fourier transform $\psi_1(z;\boldsymbol{q},\omega)$, which according to equation (3.26) must satisfy the following equation at $z \leqslant 0$:

$$(-q^2 + \mathrm{d}^2/\mathrm{d}z^2)[\omega^2 - \omega_{\mathrm{p}}^2 - \beta(-q^2 + \mathrm{d}^2/\mathrm{d}z^2)]\psi_1(z;\boldsymbol{q},\omega) = 0, \tag{3.28}$$

where $\boldsymbol{q}$ represents a 2D wave vector in the plane of the surface.

Now we need to specify the boundary conditions. Ruling out exponential increase at $z \to \infty$ and noting that the normal component of the hydrodynamical velocity should

[9] While the use of the Thomas–Fermi functional $G[n]$ of equation (3.19), which assumes static screening, predicts $\beta = \sqrt{1/3}\,(3\pi^2 n_0)^{1/3}$, the value $\beta = \sqrt{3/5}\,(3\pi^2 n_0)^{1/3}$ should be more appropriate when high-frequencies of the order of the plasma frequency are involved; see, e.g. [176].

vanish at the interface, for each value of q one finds solutions to equation (3.28) with frequencies [177, 178]

$$\omega^2 \geqslant \omega_{\rm p}^2 + \beta^2 q^2 \tag{3.29}$$

and

$$\omega^2 = \frac{1}{2}\left[\omega_{\rm p}^2 + \beta^2 q^2 + \beta q\sqrt{2\omega_{\rm p}^2 + \beta^2 q^2}\right]. \tag{3.30}$$

Equations (3.29) and (3.30) represent a continuum of bulk normal modes and a surface normal mode, respectively. At long wavelengths, where $\beta\, q/\omega_{\rm p} \ll 1$ (but still in the nonretarded regime where $\omega_{\rm s}/c < q$), equation (3.30) yields the surface-plasmon dispersion relation

$$\omega = \omega_{\rm p}/\sqrt{2} + \beta\, q/2, \tag{3.31}$$

which was first derived by Ritchie [82] using Bloch's equations, and later by Wagner [179] and by Ritchie and Marusak [180] by assuming, within a Boltzmann transport-equation approach, specular reflection at the surface.

3.2. Localized surface plasmons: classical approach

Metal–dielectric interfaces of arbitrary geometries also support charge density oscillations similar to the surface plasmons characteristic of planar interfaces. In the long-wavelength (or classical) limit, in which the interface separates two media with local (frequency-dependent) dielectric functions ϵ_1 and ϵ_2, one writes

$$\boldsymbol{D}_i(\boldsymbol{r}, \omega) = \epsilon_i\, \boldsymbol{E}_i(\boldsymbol{r}, \omega), \tag{3.32}$$

where the index i refers to the media 1 and 2 separated by the interface. In the case of simple geometries, such as spherical and cylindrical interfaces, equations (3.1)–(3.3) can be solved explicitly with the aid of equation (3.32) to find explicit expressions for the nonretarded surface-plasmon condition.

3.2.1. Simple geometries.

Spherical interface. In the case of a sphere of dielectric function ϵ_1 in a host medium of dielectric function ϵ_2, the classical (long-wavelength) planar surface-plasmon condition of equation (3.7) is easily found to be replaced by [129]

$$l\,\epsilon_1 + (l+1)\,\epsilon_2 = 0, \qquad l = 1, 2, \ldots, \tag{3.33}$$

which in the case of a Drude metal sphere (ϵ_1 of equation (2.15)) in vacuum ($\epsilon_2 = 1$) yields the Mie plasmons at frequencies

$$\omega_l = \omega_{\rm p}\sqrt{\frac{l}{2l+1}}. \tag{3.34}$$

Cylindrical interface. In the case of an infinitely long cylinder of dielectric function ϵ_1 in a host medium of dielectric function ϵ_2, the classical (long-wavelength) surface-plasmon condition depends on the direction of the electric field. For electromagnetic waves with the electric field normal to the interface (p-polarization), the corresponding long-wavelength (and nonretarded) surface-plasmon condition coincides with that of a planar surface, i.e. [181, 182, 183]

$$\epsilon_1 + \epsilon_2 = 0, \tag{3.35}$$

which for Drude cylinders (ϵ_1 of equation (2.15)) in vacuum ($\epsilon_2 = 1$) yields the planar surface-plasmon frequency $\omega_s = \omega_p/\sqrt{2}$.

For electromagnetic waves with the electric field parallel to the axis of the cylinder (s-polarization), the presence of the interface does not modify the electric field and one easily finds that only the bulk mode of the host medium is present, i.e. one finds the plasmon condition

$$\epsilon_2 = 0. \tag{3.36}$$

In some situations, instead of having one single cylinder in a host medium, an array of parallel cylinders may be present with a filling fraction f. In this case and for electromagnetic waves polarized along the cylinders (s-polarization), the plasmon condition of equation (3.36) must be replaced by [184][10]

$$f\,\epsilon_1 + (1-f)\,\epsilon_2 = 0, \tag{3.37}$$

which for Drude cylinders (ϵ_1 of equation (2.15)) in vacuum ($\epsilon_2 = 1$) yields the reduced plasmon frequency $\omega = \sqrt{f}\,\omega_p$.

3.2.2. Boundary-charge method. In the case of more complex interfaces, a so-called boundary-charge method (BCM) has been used by several authors to determine numerically the classical (long-wavelength) frequencies of localized surface plasmons. In this approach, one first considers the ω-component of the time-dependent surface charge density arising from the difference between the normal components of the electric fields inside and outside the surface:

$$\sigma_s(\boldsymbol{r},\omega) = \frac{1}{4\pi}\left[\boldsymbol{E}(\boldsymbol{r},\omega)\cdot\boldsymbol{n}|_{\boldsymbol{r}=\boldsymbol{r}^-} + \boldsymbol{E}(\boldsymbol{r},\omega)\cdot\boldsymbol{n}|_{\boldsymbol{r}=\boldsymbol{r}^+}\right], \tag{3.38}$$

which noting that the normal component of the displacement vector (see equation (3.32)) must be continuous yields the following expression:

$$\sigma_s(\boldsymbol{r},\omega) = \frac{1}{4\pi}\,\frac{\epsilon_1-\epsilon_2}{\epsilon_1}\,\boldsymbol{E}(\boldsymbol{r},\omega)\cdot\boldsymbol{n}|_{\boldsymbol{r}=\boldsymbol{r}^+}, \tag{3.39}$$

where $\boldsymbol{n}$ represents a unit vector in the direction perpendicular to the interface.

An explicit expression for the normal component of the electric field at a point of medium 2 that is infinitely close to the interface ($\boldsymbol{r} = \boldsymbol{r}^+$) can be obtained with the use of Gauss' theorem. One finds

$$\boldsymbol{E}(\boldsymbol{r},\omega)\cdot\boldsymbol{n}|_{\boldsymbol{r}=\boldsymbol{r}^+} = -\boldsymbol{n}\cdot\boldsymbol{\nabla}\phi(\boldsymbol{r},\omega) + 2\pi\sigma_s(\boldsymbol{r},\omega), \tag{3.40}$$

where $\phi(\boldsymbol{r},\omega)$ represents the scalar potential. In the absence of external sources, this potential is entirely due to the surface charge density itself:

$$\phi(\boldsymbol{r},\omega) = \int \mathrm{d}^2\boldsymbol{r}'\,\frac{\sigma_s(\boldsymbol{r}',\omega)}{|\boldsymbol{r}-\boldsymbol{r}'|}. \tag{3.41}$$

Combining equations (3.39)–(3.41), one finds the following integral equation:

$$2\pi\,\frac{\epsilon_1+\epsilon_2}{\epsilon_1-\epsilon_2}\,\sigma_s(\boldsymbol{r},\omega) - \int \mathrm{d}^2\boldsymbol{r}'\,\frac{\boldsymbol{r}-\boldsymbol{r}'}{|\boldsymbol{r}-\boldsymbol{r}'|^3}\cdot\boldsymbol{n}\,\sigma_s(\boldsymbol{r}',\omega) = 0, \tag{3.42}$$

which describes the self-sustained oscillations of the system.

The boundary-charge method has been used by several authors to determine the normal-mode frequencies of a cube [185, 186] and of bodies of arbitrary shape [187, 188]. More recent applications of this method include investigations of the surface modes of channels cut on planar surfaces [189], the surface modes of coupled parallel wires [190] and the electron energy loss near inhomogeneous dielectrics [191, 192]. A generalization of this procedure that includes relativistic corrections has been reported as well [193].

[10] It is not necessary that the cylinders are circular and the same result is found in the case of plane parallel layers aligned along the electric field.

3.2.3. Composite systems: effective-medium approach. Composite systems with a large number of interfaces can often be replaced by an effective homogeneous medium that in the long-wavelength limit is characterized by a local effective dielectric function $\epsilon_{\rm eff}(\omega)$. Bergman [194] and Milton [195] showed that in the case of a two-component system with local (frequency-dependent) dielectric functions ϵ_1 and ϵ_2 and volume fractions f and $1-f$, respectively, the long-wavelength effective dielectric function of the system can be expressed as a sum of simple poles that only depend on the microgeometry of the composite material and not on the dielectric functions of the components:

$$\epsilon_{\rm eff}(\omega) = \epsilon_2\left[1 - f\sum_\nu \frac{B_\nu}{u - m_\nu}\right], \tag{3.43}$$

where u is the spectral variable

$$u = [1 - \epsilon_1/\epsilon_2]^{-1}, \tag{3.44}$$

m_ν are depolarization factors and B_ν are the strengths of the corresponding normal modes, which all add up to unity:

$$\sum_\nu B_\nu = 1. \tag{3.45}$$

Similarly,

$$\epsilon_{\rm eff}^{-1}(\omega) = \epsilon_2^{-1}\left[1 + f\sum_\nu \frac{C_\nu}{u - n_\nu}\right], \tag{3.46}$$

with

$$\sum_\nu C_\nu = 1. \tag{3.47}$$

The optical absorption and the long-wavelength energy loss of moving charged particles are known to be dictated by the poles of the *local* effective dielectric function $\epsilon_{\rm eff}(\omega)$ and inverse dielectric function $\epsilon_{\rm eff}^{-1}(\omega)$, respectively. If there is one single interface, these poles are known to coincide.

In particular, in the case of a two-component isotropic system composed of *identical* inclusions of dielectric function ϵ_1 in a host medium of dielectric function ϵ_2, the effective dielectric function $\epsilon_{\rm eff}(\omega)$ can be obtained from the following relation:

$$(\epsilon_{\rm eff} - \epsilon_2)\,\boldsymbol{E} = f(\epsilon_1 - \epsilon_2)\,\boldsymbol{E}_{\rm in}, \tag{3.48}$$

where $\boldsymbol{E}$ is the macroscopic electric field averaged over the composite:

$$\boldsymbol{E} = f\boldsymbol{E}_{\rm in} + (1-f)\boldsymbol{E}_{\rm out}, \tag{3.49}$$

$\boldsymbol{E}_{\rm in}$ and $\boldsymbol{E}_{\rm out}$ representing the average electric field inside and outside the inclusions, respectively[11].

Simple geometries. If there is only one mode with strength different from zero, as occurs (in the long-wavelength limit) in the case of one single sphere or cylinder in a host medium, equations (3.43) and (3.46) yield

$$\epsilon_{\rm eff}(\omega) = \epsilon_2\left[1 - f\frac{1}{u - m}\right] \tag{3.50}$$

[11] In the case of identical inclusions composed of an anisotropic material, as occurs in the case of an array of fullerenes or carbon nanotubes, equation (3.48) still holds, as long as the scalar dielectric function ϵ_1 is replaced by its tensorial counterpart. In this case, the electric fields $\mathbf{E}$ and $\mathbf{E}_{\rm in}$ would have, in general, different directions.

and

$$\epsilon_{\rm eff}^{-1}(\omega) = \epsilon_2^{-1}\left[1 + f\frac{1}{u-n}\right], \tag{3.51}$$

normal modes occurring, therefore, at the frequencies dictated by the following conditions:

$$m\,\epsilon_1 + (1-m)\,\epsilon_2 = 0 \tag{3.52}$$

and

$$n\,\epsilon_1 + (1-n)\,\epsilon_2 = 0. \tag{3.53}$$

For Drude particles (ϵ_1 of equation (2.15)) in vacuum ($\epsilon_2 = 1$), these frequencies are easily found to be $\omega = \sqrt{m}\,\omega_{\rm p}$ and $\omega = \sqrt{n}\,\omega_{\rm p}$, respectively.

Indeed, for a *single* 3D spherical or 2D circular[12] inclusion in a host medium, an elementary analysis shows that the electric field $\boldsymbol{E}_{\rm in}$ in the interior of the inclusion is

$$\boldsymbol{E}_{\rm in} = \frac{u}{u-m}\,\boldsymbol{E}, \tag{3.54}$$

where $m = 1/D$, D representing the dimensionality of the inclusions, i.e. $D = 3$ for spheres and $D = 2$ for cylinders. Introduction of equation (3.54) into equation (3.48) leads to an effective dielectric function of the form of equation (3.50) with $m = 1/D$, which yields (see equation (3.52)) the surface-plasmon condition dictated by equation (3.33) with $l = 1$ in the case of spheres ($D = 3$) and the surface-plasmon condition of equation (3.35) in the case of cylinders ($D = 2$). This result indicates that in the nonretarded long-wavelength limit (which holds for wave vectors $\boldsymbol{q}$ such that $\omega_{\rm s}a/c < q\,a \ll 1$, a being the radius of the inclusions) both the absorption of light and the energy-loss spectrum of a single 3D spherical or 2D circular inclusion exhibit one single strong maximum at the dipole resonance where $\epsilon_1 + 2\epsilon_2 = 0$ and $\epsilon_1 + \epsilon_2 = 0$, respectively, which for a Drude sphere and cylinder (ϵ_1 of equation (2.15)) in vacuum ($\epsilon_2 = 1$) yield $\omega = \omega_{\rm p}/\sqrt{3}$ and $\omega = \omega_{\rm p}/\sqrt{2}$.

In the case of electromagnetic waves polarized along one single cylinder or array of parallel cylinders (s-polarization), the effective dielectric function of the composite is simply the average of the dielectric functions of its constituents, i.e.

$$\epsilon_{\rm eff} = f\,\epsilon_1 + (1-f)\,\epsilon_2, \tag{3.55}$$

which can also be written in the form of equations (3.50) and (3.51), but now with $m = 0$ and $n = f$, respectively. Hence, for this polarization the absorption of light exhibits no maxima (in the case of a dielectric host medium with constant dielectric function ϵ_2) and the long-wavelength energy-loss spectrum exhibits a strong maximum at frequencies dictated by the plasmon condition of equation (3.37), which in the case of Drude cylinders (ϵ_1 of equation (2.15)) in vacuum ($\epsilon_2 = 1$) yields the reduced plasmon frequency $\omega = \sqrt{f}\,\omega_{\rm p}$.

Maxwell–Garnett approximation. The interaction among spherical (or circular) inclusions in a host medium can be introduced approximately in the framework of the well-known Maxwell–Garnett (MG) approximation [129].

The basic assumption of this approach is that the average electric field $\boldsymbol{E}_{\rm in}$ within a particle located in a system of identical particles is related to the average field $\boldsymbol{E}_{\rm out}$ in the medium *outside* as in the case of a single isolated (noninteracting) particle, thereby only dipole interactions being taken into account. Hence, in this approach the electric field $\boldsymbol{E}_{\rm in}$ is taken to be of the form of equation (3.54) but with the macroscopic electric field $\boldsymbol{E}$ replaced by the electric field $\boldsymbol{E}_{\rm out}$

[12] In the case of p-polarized electromagnetic waves, infinitely long cylinders can be represented by 2D circular inclusions.

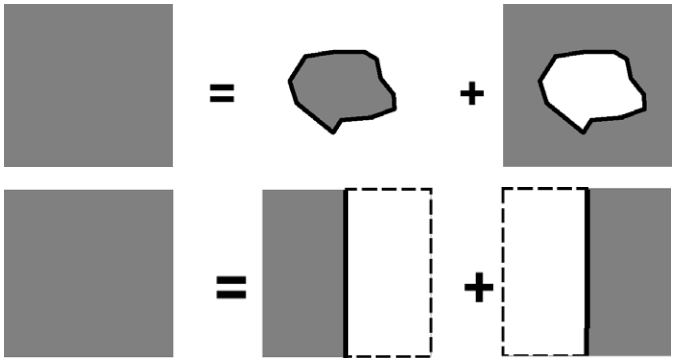

Figure 6. Complementary systems in which the regions of plasma and vacuum are interchanged. The top panel represents the general situation. The bottom panel represents a half-space filled with metal and interfaced with vacuum. The surface-mode frequencies ω_{s_1} and ω_{s_2} of these systems fulfil the sum rule of equation (3.58).

outside, which together with equations (3.48) and (3.49) yields the effective dielectric function and effective inverse dielectric function of equations (3.50) and (3.51) with the depolarization factors $m = n = 1/D$ (corresponding to the dilute limit, where $f \to 0$) replaced by

$$m = \frac{1}{D}(1 - f) \tag{3.56}$$

and

$$n = \frac{1}{D}[1 + (D - 1)f]. \tag{3.57}$$

3.2.4. Periodic structures. Over the years, theoretical studies of the normal modes of complex composite systems had been generally restricted to mean-field theories of the Maxwell–Garnett type, which approximately account for the behaviour of localized dipole plasmons [129]. Nevertheless, a number of methods have been developed recently for a full solution of Maxwell's equations in periodic structures [196–201]. The transfer matrix method has been used to determine the normal-mode frequencies of a lattice of metallic cylinders [202] and rods [203], a so-called on-shell method has been employed by Yannopapas *et al* to investigate the plasmon modes of a lattice of metallic spheres in the low filling fraction regime [204] and a finite difference time domain (FDTD) scheme has been adapted to extract the effective response of metallic structures [201].

Most recently, an embedding method [199] has been employed to solve Maxwell's equations, which has allowed to calculate the photonic band structure of three- and two-dimensional lattices of nanoscale metal spheres and cylinders in the frequency range of the Mie plasmons [143]. For small filling fractions, there is a surface-plasmon polariton which in the nonretarded region yields the nondispersive Mie plasmon with frequency $\omega_p/\sqrt{D}$. As the filling fraction increases, a continuum of plasmon modes is found to exist between zero frequency and the bulk metal plasmon frequency [143], which yield strong absorption of incident light and whose energies can be tuned according to the particle–particle separation [205].

3.2.5. Sum rules. Sum rules have played a key role in providing insight in the investigation of a variety of physical situations. A useful sum rule for the surface modes in complementary

media with arbitrary geometry was introduced by Apell *et al* [206], which in the special case of a metal/vacuum interface implies that [207]

$$\omega_{s_1}^2 + \omega_{s_2}^2 = \omega_p^2, \tag{3.58}$$

where ω_{s_1} is the surface-mode frequency of a given system and ω_{s_2} represents the surface mode of a second complementary system in which the regions of plasma and vacuum are interchanged (see figure 6).

For example, a half-space filled with a metal of bulk plasma frequency ω_p and interfaced with vacuum maps into itself (see bottom panel of figure 6), and therefore equation (3.58) yields

$$\omega_{s_1} = \omega_{s_2} = \omega_p/\sqrt{2}, \tag{3.59}$$

which is Ritchie's frequency of plasma oscillations at a metal/vacuum planar interface.

Other examples are a Drude metal sphere in vacuum, which sustains *localized* Mie plasmons at frequencies given by equation (3.34), and a spherical void in a Drude metal, which shows Mie plasmons at frequencies

$$\omega_l = \omega_p \sqrt{\frac{l+1}{2l+1}}. \tag{3.60}$$

The squared surface-mode frequencies of the sphere (equation (3.34)) and the void (equation (3.60)) add up to ω_p^2 for all l, as required by equation (3.58).

The splitting of surface modes that occurs in thin films due to the coupling of the electromagnetic fields in the two surfaces (see equation (2.26)) also occurs in the case of localized modes. Apell *et al* [206] proved a second sum rule, which relates the surface modes corresponding to the in-phase and out-of-phase linear combinations of the screening charge densities at the interfaces. In the case of metal/vacuum interfaces this sum rule takes the form of equation (3.58) but now ω_{s_1} and ω_{s_2} being in-phase and out-of-phase modes of the same system.

For a Drude metal film with equal and abrupt planar surfaces, the actual values of the *nonretarded* ω_{s_1} and ω_{s_2} are those given by equation (2.27), which fulfil the sum rule dictated by equation (3.58). For a spherical fullerene molecule described by assigning a Drude dielectric function to every point between the inner and outer surfaces of radii r_1 and r_2, one finds the following frequencies for the in-phase and out-of-phase surface modes [208]:

$$\omega_s^2 = \frac{\omega_p^2}{2}\left[1 \pm \frac{1}{2l+1}\sqrt{1 + 4l(l+1)(r_1/r_2)^{2l+1}}\right], \tag{3.61}$$

also fulfilling the sum rule of equation (3.58).

Another sum rule has been reported recently [202, 203], which relates the frequencies of the modes that can be excited by light (as dictated by the poles of the effective dielectric function of equation (3.43)) and those modes that can be excited by moving charged particles (as dictated by the poles of the effective inverse dielectric function of equation (3.46)). Numerical calculations for various geometries have shown that the depolarization factors m_ν and n_ν entering equations (3.43) and (3.46) satisfy the relation [202, 203]

$$n_\nu = 1 - (D-1)\, m_\nu, \tag{3.62}$$

where D represents the dimensionality of the inclusions.

Furthermore, combining equations (3.50) and (3.51) (and assuming, therefore, that only dipole interactions are present) with the sum rule of equation (3.62) yields equations (3.56) and (3.57), i.e. the MG approximation. Conversely, as long as multipolar modes contribute to the spectral representation of the effective response (see equations (3.43) and (3.46)), the

strength of the dipolar modes decreases (see equations (3.45) and (3.47)) and a combination of equations (3.43) and (3.46) with equation (3.62) leads to the conclusion that the dipolar resonances must necessarily deviate from their MG counterparts dictated by equations (3.56) and (3.57). That a nonvanishing contribution from multipolar modes appears together with a deviation of the frequencies of the dipolar modes with respect to their MG counterparts was shown explicitly in [202].

4. Dynamical structure factor

The dynamical structure factor $S(\boldsymbol{r}, \boldsymbol{r}'; \omega)$ represents a key quantity in the description of both single-particle and collective electronic excitations in a many-electron system [209]. The rate for the generation of electronic excitations by an external potential, the inelastic differential cross section for external particles to scatter in a given direction, the inelastic lifetime of excited hot electrons, the so-called stopping power of a many-electron system for moving charged particles and the ground-state energy of an arbitrary many-electron system (which is involved in, for example the surface energy and the understanding of Van der Waals interactions) are all related to the dynamical structure factor of the system.

The dynamical structure factor, which accounts for the particle-density fluctuations of the system, is defined as follows:

$$S(\boldsymbol{r}, \boldsymbol{r}'; \omega) = \sum_n \delta\hat{\rho}_{0n}(\boldsymbol{r}_1)\, \delta\hat{\rho}_{n0}(\boldsymbol{r}_2)\, \delta(\omega - E_n + E_0). \tag{4.1}$$

Here, $\delta\hat{\rho}_{n0}(\boldsymbol{r})$ represent matrix elements, taken between the many-particle ground state $|\Psi_0\rangle$ of energy E_0 and the many-particle excited state $|\Psi_n\rangle$ of energy E_n, of the operator $\hat{\rho}(\boldsymbol{r}) - n_0(\boldsymbol{r})$, where $\hat{\rho}(\boldsymbol{r})$ is the electron-density operator [210]:

$$\hat{\rho}(\boldsymbol{r}) = \sum_{i=1}^{N} \hat{\delta}(\boldsymbol{r} - \boldsymbol{r}_i), \tag{4.2}$$

with $\hat{\delta}$ and $\boldsymbol{r}_i$ describing the Dirac-delta operator and electron coordinates, respectively, and $n_0(\boldsymbol{r})$ represents the ground-state electron density, i.e.

$$n_0(\boldsymbol{r}) = < \Psi_0 | \hat{\rho}(\boldsymbol{r}) | \Psi_0 > . \tag{4.3}$$

The many-body ground and excited states of a many-electron system are *unknown* and the dynamical structure factor is, therefore, difficult to calculate. Nevertheless, one can use the zero-temperature limit of the fluctuation–dissipation theorem [211], which relates the dynamical structure factor $S(\boldsymbol{r}, \boldsymbol{r}'; \omega)$ to the dynamical density-response function $\chi(\boldsymbol{r}, \boldsymbol{r}'; \omega)$ of linear-response theory. One writes,

$$S(\boldsymbol{r}, \boldsymbol{r}'; \omega) = -\frac{\Omega}{\pi} \operatorname{Im}\chi(\boldsymbol{r}, \boldsymbol{r}'; \omega)\, \theta(\omega), \tag{4.4}$$

where Ω represents the normalization volume and $\theta(x)$ is the Heaviside step function.

5. Density-response function

Take a system of N interacting electrons exposed to a frequency-dependent external potential $\phi^{\text{ext}}(\boldsymbol{r}, \omega)$. Keeping terms of first order in the external perturbation and neglecting *retardation* effects, time-dependent perturbation theory yields the following expression for the induced electron density [210]:

$$\delta n(\boldsymbol{r}, \omega) = \int \mathrm{d}\boldsymbol{r}'\, \chi(\boldsymbol{r}, \boldsymbol{r}'; \omega)\, \phi^{\text{ext}}(\boldsymbol{r}', \omega), \tag{5.1}$$

where $\chi(\boldsymbol{r},\boldsymbol{r}';\omega)$ represents the so-called density-response function of the many-electron system:

$$\chi(\boldsymbol{r},\boldsymbol{r}';\omega)=\sum_n \rho^*_{n0}(\boldsymbol{r})\rho_{n0}(\boldsymbol{r}')\left[\frac{1}{E_0-E_n+\hbar(\omega+\mathrm{i}\eta)}-\frac{1}{E_0+E_n+\hbar(\omega+\mathrm{i}\eta)}\right], \tag{5.2}$$

η being a positive infinitesimal.

The imaginary part of the true density-response function of equation (5.2), which accounts for the creation of both collective and single-particle excitations in the many-electron system, is known to satisfy the so-called f-sum rule:

$$\int_{-\infty}^{\infty} \mathrm{d}\omega\,\omega\,\mathrm{Im}\chi(\boldsymbol{r},\boldsymbol{r}';\omega)=-\pi\boldsymbol{\nabla}\cdot\boldsymbol{\nabla}'\left[n_0(\boldsymbol{r})\delta(\boldsymbol{r},\boldsymbol{r}')\right], \tag{5.3}$$

with $n_0(\boldsymbol{r})$ being the unperturbed ground-state electron density of equation (4.3).

5.1. Random-phase approximation (RPA)

In the so-called random-phase or, equivalently, time-dependent Hartree approximation, the electron density $\delta n(\boldsymbol{r},\omega)$ induced in an *interacting* electron system by a small external potential $\phi^{\mathrm{ext}}(\boldsymbol{r},\omega)$ is obtained as the electron density induced in a *noninteracting* Hartree system (of electrons moving in a self-consistent Hartree potential) by both the external potential $\phi^{\mathrm{ext}}(\boldsymbol{r},\omega)$ and the induced potential

$$\delta\phi^{\mathrm{H}}(\boldsymbol{r},\omega)=\int \mathrm{d}\boldsymbol{r}'\,v(\boldsymbol{r},\boldsymbol{r}')\,\delta n(\boldsymbol{r}',\omega), \tag{5.4}$$

with $v(\boldsymbol{r},\boldsymbol{r}')$ representing the bare Coulomb interaction. Hence, in this approximation one writes

$$\delta n(\boldsymbol{r},\omega)=\int \mathrm{d}\boldsymbol{r}'\,\chi^0(\boldsymbol{r},\boldsymbol{r}';\omega)\times\left[\phi^{\mathrm{ext}}(\boldsymbol{r}',\omega)+\int \mathrm{d}\boldsymbol{r}''\,v(\boldsymbol{r}',\boldsymbol{r}'')\,\delta n(\boldsymbol{r}'',\omega)\right], \tag{5.5}$$

which together with equation (5.1) yields the following Dyson-type equation for the *interacting* density-response function:

$$\chi(\boldsymbol{r},\boldsymbol{r}';\omega)=\chi^\circ(\boldsymbol{r},\boldsymbol{r}';\omega)+\int \mathrm{d}\boldsymbol{r}_1\int \mathrm{d}\boldsymbol{r}_2\,\chi^0(\boldsymbol{r},\boldsymbol{r}_1;\omega)v(\boldsymbol{r}_1,\boldsymbol{r}_2)\,\chi(\boldsymbol{r}_2,\boldsymbol{r}';\omega), \tag{5.6}$$

where $\chi^0(\boldsymbol{r},\boldsymbol{r}';\omega)$ denotes the density-response function of noninteracting Hartree electrons:

$$\chi^0(\boldsymbol{r},\boldsymbol{r}';\omega)=\frac{2}{\Omega}\sum_{i,j}(f_i-f_j)\frac{\psi_i(\boldsymbol{r})\psi^*_j(\boldsymbol{r})\psi_j(\boldsymbol{r}')\psi^*_i(\boldsymbol{r}')}{\omega-\varepsilon_j+\varepsilon_i+\mathrm{i}\eta}. \tag{5.7}$$

Here, f_i are Fermi–Dirac occupation factors, which at zero temperature take the form $f_i=\theta(\varepsilon_{\mathrm{F}}-\varepsilon_i)$, ε_{F} being the Fermi energy and the single-particle states and energies $\psi_i(\boldsymbol{r})$ and ε_i are the eigenfunctions and eigenvalues of a Hartree Hamiltonian, i.e.

$$\left[-\frac{1}{2}\nabla^2+v_{\mathrm{H}}[n_0](\boldsymbol{r})\right]\psi_i(\boldsymbol{r})=\varepsilon_i\,\psi_i(\boldsymbol{r}), \tag{5.8}$$

where

$$v_{\mathrm{H}}[n_0](\boldsymbol{r}) = v_0(\boldsymbol{r}) + \int \mathrm{d}\boldsymbol{r}'\, v(\boldsymbol{r},\boldsymbol{r}')n_0(\boldsymbol{r}'), \tag{5.9}$$

with $v_0(\boldsymbol{r})$ denoting a static external potential and $n_0(\boldsymbol{r})$ being the unperturbed Hartree electron density:

$$n_0(\boldsymbol{r}) = \sum_{i=1}^{N} |\psi_i(\boldsymbol{r})|^2. \tag{5.10}$$

5.2. Time-dependent density-functional theory

In the framework of time-dependent density-functional theory (TDDFT) [212], the *exact* density-response function of an interacting many-electron system is found to obey the following Dyson-type equation:

$$\chi(\boldsymbol{r},\boldsymbol{r}';\omega) = \chi^0(\boldsymbol{r},\boldsymbol{r}';\omega) + \int \mathrm{d}\boldsymbol{r}_1 \int \mathrm{d}\boldsymbol{r}_2\, \chi^0(\boldsymbol{r},\boldsymbol{r}_1;\omega) \times \{v(\boldsymbol{r}_1,\boldsymbol{r}_2) + f_{\mathrm{xc}}[n_0](\boldsymbol{r}_1,\boldsymbol{r}_2;\omega)\}\, \chi(\boldsymbol{r}_2,\boldsymbol{r}';\omega). \tag{5.11}$$

Here, the noninteracting density-response function $\chi^0(\boldsymbol{r},\boldsymbol{r}';\omega)$ is of the form of equation (5.7) but with the single-particle states and energies $\psi_i(\boldsymbol{r})$ and ε_i being now the eigenfunctions and eigenvalues of the Kohn–Sham DFT, i.e:

$$\left[-\frac{1}{2}\nabla^2 + v_{\mathrm{KS}}[n_0](\boldsymbol{r})\right] \psi_i(\boldsymbol{r}) = \varepsilon_i\, \psi_i(\boldsymbol{r}), \tag{5.12}$$

where

$$v_{\mathrm{KS}}[n_0](\boldsymbol{r}) = v_{\mathrm{H}}[n_0](\boldsymbol{r}) + v_{\mathrm{xc}}[n_0](\boldsymbol{r}) \tag{5.13}$$

with

$$v_{\mathrm{xc}}[n_0](\boldsymbol{r}) = \left.\frac{\delta E_{\mathrm{xc}}[n]}{\delta n(\boldsymbol{r})}\right|_{n=n_0}. \tag{5.14}$$

$E_{\mathrm{xc}}[n]$ represents the *unknown* XC energy functional and $n_0(\boldsymbol{r})$ denotes the exact unperturbed electron density of equation (4.3), which the DFT shows to coincide with that of equation (5.10) but with the Hartree eigenfunctions $\psi_i(\boldsymbol{r})$ of equation (5.8) being replaced by their Kohn–Sham counterparts of equation (5.12). The XC kernel $f_{\mathrm{xc}}[n_0](\boldsymbol{r},\boldsymbol{r}';\omega)$ denotes the Fourier transform of

$$f_{\mathrm{xc}}[n_0](\boldsymbol{r},t;\boldsymbol{r}',t') = \left.\frac{\delta v_{\mathrm{xc}}[n](\boldsymbol{r},t)}{\delta n(\boldsymbol{r}',t')}\right|_{n=n_0}, \tag{5.15}$$

with $v_{\mathrm{xc}}[n](\boldsymbol{r},t)$ being the exact time-dependent XC potential of TDDFT.

If short-range XC effects are ignored altogether by setting the *unknown* XC potential $v_{\mathrm{xc}}[n_0](\boldsymbol{r})$ and XC kernel $f_{\mathrm{xc}}[n_0](\boldsymbol{r},\boldsymbol{r}';\omega)$ equal to zero, the TDDFT density-response function of equation (5.11) reduces to the RPA equation (5.6).

5.2.1. The XC kernel. Along the years, several approximations have been used to evaluate the *unknown* XC kernel of equation (5.15).

Random-phase approximation (RPA). Nowadays, one usually refers to the RPA as the result of simply setting the XC kernel $f_{\rm xc}[n_0](\boldsymbol{r},\boldsymbol{r}';\omega)$ equal to zero:

$$f_{\rm xc}^{\rm RPA}[n_0](\boldsymbol{r},\boldsymbol{r}';\omega)=0, \tag{5.16}$$

but still using in equations (5.7) and (5.10) the full single-particle states and energies $\psi_i(\boldsymbol{r})$ and ε_i of DFT (i.e. the solutions of equation (5.12)) with $v_{\rm xc}[n_0](\boldsymbol{r})$ set different from zero. This is sometimes called the DFT-based RPA.

Adiabatic local-density approximation (ALDA). In this approximation, also called time-dependent local-density approximation (TDLDA) [213], one assumes that both the unperturbed $n_0(\boldsymbol{r})$ and the induced $\delta n(\boldsymbol{r},\omega)$ electron densities vary slowly in space and time and, therefore, one replaces the dynamical XC kernel by the long-wavelength ($Q\to 0$) limit of the static XC kernel of a homogeneous electron gas at the local density:

$$f_{\rm xc}^{\rm ALDA}[n_0](\boldsymbol{r},\boldsymbol{r}';\omega)=\left.\frac{{\rm d}^2\left[n\varepsilon_{\rm xc}(n)\right]}{{\rm d}n^2}\right|_{n=n_0(\boldsymbol{r})}\delta(\boldsymbol{r}-\boldsymbol{r}'), \tag{5.17}$$

where $\varepsilon_{\rm xc}(n)$ is the XC energy per particle of a homogeneous electron gas of density n.

PGG and BPG. In the spirit of the optimized effective-potential method [214], Petersilka, Gossmann and Gross (PGG) [215] derived the following frequency-independent exchange-only approximation for inhomogeneous systems:

$$f_x^{\rm PGG}[n_0](\boldsymbol{r},\boldsymbol{r}';\omega)=-\frac{2}{|\boldsymbol{r}-\boldsymbol{r}'|}\,\frac{\left|\sum_i f_i\,\psi_i(\boldsymbol{r})\,\psi_i^*(\boldsymbol{r}')\right|^2}{n_0(\boldsymbol{r})n_0(\boldsymbol{r}')}, \tag{5.18}$$

where $\psi_i(\boldsymbol{r})$ denote the solutions of the Kohn–Sham equation (5.12).

More recently, Burke, Petersilka, and Gross (BPG) [216] devised a hybrid formula for the XC kernel, which combines expressions for symmetric and antisymmetric spin orientations from the exchange-only PGG scheme and the ALDA. For an unpolarized many-electron system, one writes [216]

$$f_{\rm xc}^{\rm BPG}[n_0](\boldsymbol{r},\boldsymbol{r}';\omega)=\frac{1}{2}\left[f_{\rm xc}^{\uparrow\uparrow,{\rm PGG}}+f_{\rm xc}^{\uparrow\downarrow,{\rm ALDA}}\right], \tag{5.19}$$

where $f_{\rm xc}^{\uparrow\uparrow}$ and $f_{\rm xc}^{\uparrow\downarrow}$ represent the XC kernel for electrons with parallel and antiparallel spin, respectively.

Average approximation. The investigation of short-range XC effects in solids has been focused to a great extent onto the simplest possible many-electron system, which is the homogeneous electron gas. Hence, recent attempts to account for XC effects in inhomogeneous systems have adopted the following approximation [217, 218]:

$$f_{\rm xc}^{\rm av}[n_0](\boldsymbol{r},\boldsymbol{r}';\omega)=f_{\rm xc}^{\rm hom}(\tilde{n};|\boldsymbol{r}-\boldsymbol{r}'|;\omega), \tag{5.20}$$

where $\tilde{n}$ represents a function of the electron densities at points $\boldsymbol{r}$ and $\boldsymbol{r}'$, typically the arithmetical average

$$\tilde{n}=\frac{1}{2}\left[n_0(\boldsymbol{r})+n_0(\boldsymbol{r}')\right], \tag{5.21}$$

and $f_{\rm xc}^{\rm hom}(\tilde{n};|\boldsymbol{r}-\boldsymbol{r}'|;\omega)$ denotes the XC kernel of a homogeneous electron gas of density $\tilde{n}$, whose 3D Fourier transform $f_{\rm xc}^{\rm hom}(\tilde{n};Q,\omega)$ is directly connected to the so-called local-field factor $G(\tilde{n};Q,\omega)$:

$$f_{\rm xc}^{\rm hom}(\tilde{n};Q,\omega)=-\frac{4\pi}{Q^2}\,G(\tilde{n};Q,\omega). \tag{5.22}$$

In the ALDA, one writes

$$G^{\mathrm{ALDA}}(\tilde{n};\, Q, \omega) = G(\tilde{n};\, Q \to 0, \omega = 0) = -\frac{Q^2}{4\pi}\left.\frac{\mathrm{d}^2\,[n\varepsilon_{\mathrm{xc}}(n)]}{\mathrm{d}n^2}\right|_{n=\tilde{n}}, \tag{5.23}$$

which in combination with equations (5.20)–(5.22) yields the ALDA XC kernel of equation (5.17). However, more accurate nonlocal dynamical expressions for the local-field factor $G(\tilde{n};\, Q, \omega)$ are available nowdays, which together with equations (5.20)–(5.22) should yield an accurate (beyond the ALDA) representation of the XC kernel of inhomogeneous systems.

During the last decades, much effort has gone into the determination of the static local-field factor $G^{\mathrm{static}}(\tilde{n};\, Q) = G(\tilde{n};\, Q, \omega = 0)$ [219–226], the most recent works including diffusion Monte Carlo (DMC) calculations [227,228] and the parametrization of the DMC data of [228] given by Corradini *et al* [229]:

$$G^{\mathrm{static}}(\tilde{n};\, Q) = C\,\hat{Q}^2 + B\,\hat{Q}^2/(g + \hat{Q}^2) + \alpha\,\hat{Q}^4\,\mathrm{e}^{-\beta\,\hat{Q}^2}, \tag{5.24}$$

where $\hat{Q} = Q/q_{\mathrm{F}}$, and the parameters B, C, g, α and β are the dimensionless functions of $\tilde{n}$ listed in [229].

Calculations of the frequency dependence of the local-field factor $G(\tilde{n};\, Q, \omega)$ have been carried out mainly in the limit of long wavelengths ($Q \to 0$) [230–235], but work has also been done for finite wave vectors [236–239].

6. Inverse dielectric function

In the presence of a many-electron system, the total potential $\phi(\boldsymbol{r}, \omega)$ of a unit test charge at point $\boldsymbol{r}$ that is exposed to the external potential $\phi^{\mathrm{ext}}(\boldsymbol{r}, \omega)$ can be expressed in the following form:

$$\phi(\boldsymbol{r}, \omega) = \phi^{\mathrm{ext}}(\boldsymbol{r}, \omega) + \delta\phi^{\mathrm{H}}(\boldsymbol{r}, \omega), \tag{6.1}$$

where $\delta\phi^{\mathrm{H}}(\boldsymbol{r}, \omega)$ represents the induced potential of equation (5.4). Using equations (5.1) and (5.4), the total potential $\phi(\boldsymbol{r}, \omega)$ of equation (6.1) is easily found to take the following form:

$$\phi(\boldsymbol{r}, \omega) = \int \mathrm{d}\boldsymbol{r}'\, \epsilon^{-1}(\boldsymbol{r}, \boldsymbol{r}'; \omega)\, \phi^{\mathrm{ext}}(\boldsymbol{r}', \omega), \tag{6.2}$$

where

$$\epsilon^{-1}(\boldsymbol{r}, \boldsymbol{r}'; \omega) = \delta(\boldsymbol{r} - \boldsymbol{r}') + \int \mathrm{d}\boldsymbol{r}''\, v(\boldsymbol{r} - \boldsymbol{r}'')\, \chi(\boldsymbol{r}'', \boldsymbol{r}'; \omega). \tag{6.3}$$

This is the so-called inverse *longitudinal* dielectric function of the many-electron system, whose poles dictate the occurrence of collective electronic excitations and which can be evaluated in the RPA or in the framework of TDDFT from the knowledge of the density-response function of equations (5.6) and (5.11), respectively.

Some quantities, such as the optical absorption and the electron energy loss of charged particles moving in arbitrary inhomogeneous media, can be described by the so-called effective inverse dielectric function $\epsilon^{-1}_{\mathrm{eff}}(\boldsymbol{Q}, \omega)$, which is defined as a 3D Fourier transform of the inverse dielectric function $\epsilon^{-1}(\boldsymbol{r}, \boldsymbol{r}'; \omega)$:

$$\epsilon^{-1}_{\mathrm{eff}}(\boldsymbol{Q}, \omega) = \frac{1}{\Omega}\int \mathrm{d}\boldsymbol{r} \int \mathrm{d}\boldsymbol{r}'\, \mathrm{e}^{-i\boldsymbol{Q}\cdot(\boldsymbol{r}-\boldsymbol{r}')}\, \epsilon^{-1}(\boldsymbol{r}, \boldsymbol{r}'; \omega) \tag{6.4}$$

and which at long wavelengths ($Q \to 0$) should take the form of equation (3.46)[13].

In particular, in the case of a homogeneous system and in the *classical* long-wavelength limit, where the total potential $\phi(\boldsymbol{r}, \omega)$ of a unit test charge at point $\boldsymbol{r}$ only depends on the external potential $\phi^{\rm ext}(\boldsymbol{r}, \omega)$ at that point, the inverse dielectric function takes the following form:

$$\epsilon^{-1}(\boldsymbol{r}, \boldsymbol{r}'; \omega) = \epsilon^{-1}(\omega)\, \delta(\boldsymbol{r} - \boldsymbol{r}'), \tag{6.5}$$

which in combination with equation (6.2) yields the classical formula

$$\phi(\boldsymbol{r}, \omega) = \phi^{\rm ext}(\boldsymbol{r}, \omega)/\epsilon(\omega), \tag{6.6}$$

$\epsilon(\omega)$ representing the so-called *local* dielectric function of the medium.

7. Screened interaction

Another key quantity in the description of electronic excitations in a many-electron system, which also dictates the occurrence of collective electronic excitations, is the frequency-dependent complex screened interaction $W(\boldsymbol{r}, \boldsymbol{r}'; \omega)$. This quantity yields the total potential $\phi(\boldsymbol{r}, \omega)$ of a unit test charge at point $\boldsymbol{r}$ in the presence of an external test charge of density $n^{\rm ext}(\boldsymbol{r}', \omega)$ at point $\boldsymbol{r}'$:

$$\phi(\boldsymbol{r}, \omega) = \int {\rm d}\boldsymbol{r}'\, W(\boldsymbol{r}, \boldsymbol{r}'; \omega)\, n^{\rm ext}(\boldsymbol{r}', \omega). \tag{7.1}$$

The potential $\phi^{\rm ext}(\boldsymbol{r}, \omega)$ due to the external test charge density $n^{\rm ext}(\boldsymbol{r}, \omega)$ is simply

$$\phi^{\rm ext}(\boldsymbol{r}, \omega) = \int {\rm d}\boldsymbol{r}'\, v(\boldsymbol{r}, \boldsymbol{r}')\, n^{\rm ext}(\boldsymbol{r}', \omega). \tag{7.2}$$

Hence, a comparison of equations (6.2) and (7.1) yields

$$W(\boldsymbol{r}, \boldsymbol{r}'; \omega) = \int {\rm d}\boldsymbol{r}''\, \epsilon^{-1}(\boldsymbol{r}, \boldsymbol{r}''; \omega)\, v(\boldsymbol{r}'', \boldsymbol{r}'), \tag{7.3}$$

and using equation (6.3):

$$W(\boldsymbol{r}, \boldsymbol{r}'; \omega) = v(\boldsymbol{r}, \boldsymbol{r}') + \int {\rm d}\boldsymbol{r}_1 \int {\rm d}\boldsymbol{r}_2 v(\boldsymbol{r}, \boldsymbol{r}_1)\, \chi(\boldsymbol{r}_1, \boldsymbol{r}_2; \omega)\, v(\boldsymbol{r}_2, \boldsymbol{r}'). \tag{7.4}$$

From equations (6.4) and (7.3) one easily finds the following representation of the effective inverse dielectric function:

$$\epsilon^{-1}_{\rm eff}(\boldsymbol{Q}, \omega) = \frac{1}{\Omega v_Q} \int {\rm d}\boldsymbol{r} \int {\rm d}\boldsymbol{r}'\, {\rm e}^{-{\rm i}\boldsymbol{Q}\cdot(\boldsymbol{r}-\boldsymbol{r}')}\, W(\boldsymbol{r}, \boldsymbol{r}'; \omega), \tag{7.5}$$

where $v_Q = 4\pi/Q^2$ denotes the 3D Fourier transform of the bare Coulomb interaction $v(\boldsymbol{r}, \boldsymbol{r}')$.

7.1. Classical model

In a classical model consisting of two homogeneous media characterized by local (frequency-dependent) dielectric functions ϵ_1 and ϵ_2 and separated by an interface of arbitrary geometry, the total potential at each medium is simply given by equation (6.6) and is, therefore, a solution of Poisson's equation

$$\nabla^2 \phi(\boldsymbol{r}, \omega) = -\frac{4\pi}{\epsilon_i(\omega)}\, n^{\rm ext}(\boldsymbol{r}, \omega), \tag{7.6}$$

[13] In the long-wavelength ($Q \to 0$) limit, longitudinal and transverse dielectric functions with the same polarization coincide.

$\epsilon_i(\omega)$ being ϵ_1 or ϵ_2 depending on whether the point $\boldsymbol{r}$ is located in medium 1 or in medium 2, respectively. Hence, the screened interaction $W(\boldsymbol{r}, \boldsymbol{r}'; \omega)$ entering equation (7.1) is a solution of the following equation:

$$\nabla^2 W(\boldsymbol{r}, \boldsymbol{r}'; \omega) = -\frac{4\pi}{\epsilon_i(\omega)}\,\delta(\boldsymbol{r} - \boldsymbol{r}'). \tag{7.7}$$

For simple geometries, such as the planar, spherical and cylindrical interfaces, equation (7.7) can be solved explicitly by imposing the ordinary boundary conditions of continuity of the potential and the normal component of the displacement vector at the interface.

7.1.1. Planar surface. In the case of two semi-infinite media with local (frequency-dependent) dielectric functions ϵ_1 (at $z < 0$) and ϵ_2 (at $z > 0$) separated by a planar interface at $z = 0$ (see figure 1), there is translational invariance in two directions, which we take to be normal to the z axis. Hence, one can define the Fourier transform $W(z, z'; q, \omega)$, q being the magnitude of a 2D wave vector in the plane of the interface, and imposing the ordinary boundary conditions of continuity of the potential and the normal component of the displacement vector at the interface, one finds:

$$W(z, z'; q, \omega) = \frac{2\pi}{q} \begin{cases} \left[\mathrm{e}^{-q|z-z'|} + g\,\mathrm{e}^{-q(|z|+|z'|)}\right]/\epsilon_1, & z < 0, z' < 0, \\ 2\,g\,\mathrm{e}^{-q|z-z'|}/(\epsilon_1 - \epsilon_2), & z^< < 0, z^> > 0, \\ \left[\mathrm{e}^{-q|z-z'|} - g\,\mathrm{e}^{-q(|z|+|z'|)}\right]/\epsilon_2, & z > 0, z' > 0, \end{cases} \tag{7.8}$$

where $z^<$ ($z^>$) is the smallest (largest) of z and z', and g is the classical surface-response function:

$$g(\omega) = \frac{\epsilon_1(\omega) - \epsilon_2(\omega)}{\epsilon_1(\omega) + \epsilon_2(\omega)}, \tag{7.9}$$

or, equivalently,

$$g(\omega) = -\frac{n}{u - n}, \tag{7.10}$$

where u is the spectral variable of equation (3.44) and $n = 1/2$.

An inspection of equations (7.8) and (7.9) shows that the screened interaction $W(z, z'; q, \omega)$ has poles at the *classical* bulk- and surface-plasmon conditions dictated by $\epsilon_i = 0$ and by equation (3.7), respectively.

7.1.2. Spheres. In the case of a sphere of radius a and local (frequency-dependent) dielectric function ϵ_1 embedded in a host medium of local (frequency-dependent) dielectric function ϵ_2, we first expand the screened interaction $W(\boldsymbol{r}, \boldsymbol{r}'; \omega)$ in spherical harmonics:

$$W(\boldsymbol{r}, \boldsymbol{r}'; \omega) = \sum_{l,m} \frac{4\pi}{2l+1}\, W_l(r, r'; \omega)\, Y^*_{l,m}(\Omega)\, Y_{l,m}(\Omega'), \tag{7.11}$$

and we then derive the coefficients of this expansion by imposing the boundary conditions. One finds [240][14]:

$$W_l(r,r';\omega) = \begin{cases} \left[\dfrac{(r^<)^l}{(r^>)^{l+1}} + (l+1)\, g_l\, \dfrac{(r\,r')^l}{a^{2l+1}}\right]/\epsilon_1, & r,r' < a, \\ (l+1)\, g_l \dfrac{(r^<)^l}{(r^>)^{l+1}}/(\epsilon_1-\epsilon_2), & r^< < a, r^> > a, \\ \left[\dfrac{(r^<)^l}{(r^>)^{l+1}} - l\, g_l\, \dfrac{a^{2l+1}}{(r\,r')^{l+1}}\right]/\epsilon_2, & r,r' > a, \end{cases} \tag{7.12}$$

where $r^<$ ($r^>$) is the smallest (largest) of r and r', and

$$g_l(\omega) = \frac{\epsilon_1(\omega)-\epsilon_2(\omega)}{l\,\epsilon_1(\omega)+(l+1)\,\epsilon_2(\omega)}, \tag{7.13}$$

or, equivalently,

$$g_l(\omega) = -\frac{n_l}{u-n_l}, \tag{7.14}$$

with u being the spectral variable of equation (3.44) and

$$n_l = \frac{l}{2l+1}. \tag{7.15}$$

As in the case of the planar surface, the screened interaction of equations (7.11)–(7.13) has poles at the *classical* bulk- and surface-plasmon conditions, which in the case of a single sphere in a host medium are dictated by $\epsilon_i = 0$ and by equation (3.33), respectively.

Introducing equations (7.11)–(7.13) into equation (7.5), one finds the following expression for the effective inverse dielectric function [182]:

$$\epsilon^{-1}_{\rm eff}(Q,\omega) = \epsilon_2^{-1} + f(\epsilon_1^{-1}-\epsilon_2^{-1})\left[1+\frac{3}{x}\sum_{l=0}^{\infty}(2l+1)\, g_l\, j_l(x)\, \Theta_l(x)\right], \tag{7.16}$$

where

$$\Theta_l(x) = \frac{l\, j_{l-1}(x)\,\epsilon_1 - (l+1)\, j_{l+1}(x)\,\epsilon_2}{\epsilon_1-\epsilon_2} \tag{7.17}$$

and $x = Qa$. Here, f represents the volume fraction filled by the sphere and $j_l(x)$ are spherical Bessel functions of the first kind [241]. This equation represents the dilute ($f \to 0$) limit of the effective inverse dielectric function derived by Barrera and Fuchs for a system composed of identical interacting spheres in a host medium [242].

In the limit as $Qa \ll 1$, an expansion of equation (7.16) yields

$$\epsilon^{-1}_{\rm eff}(Q,\omega) = \epsilon_2^{-1}\left[1-3f\,\frac{\epsilon_1-\epsilon_2}{\epsilon_1+2\epsilon_2}\right], \tag{7.18}$$

which is precisely the long-wavelength effective inverse dielectric function obtained in section 3.2.3 from equations (3.48) and (3.54) with $D = 3$ and which admits the spectral representation of equation (3.51) with $n = 1/3$. This result demonstrates the expected result

[14] The direct contribution to the screened interaction is missing in the first line of equation (5) of this reference, as pointed out in [182]. This contribution, together with part of the term represented in the second line of equation (5), would give the bulk contribution $\epsilon^{-1} - 1$ to equation (7) of the same reference. Hence, equation (5) of this reference must be replaced by equations (7.11)–(7.13) of the present manuscript with $\epsilon_2 = 1$.

that in the limit as $Qa \ll 1$ a broad beam of charged particles interacting with a single sphere of dielectric function ϵ_1 in a host medium of dielectric function ϵ_2 can only create collective excitations at the *dipole* resonance where $\epsilon_1 + 2\epsilon_2 = 0$ (equation (3.33) with $l = 1$), which for a Drude sphere in vacuum yields $\omega = \omega_p/\sqrt{3}$.

7.1.3. Cylinders. In the case of an infinitely long cylinder of radius a and local (frequency-dependent) dielectric function ϵ_1 embedded in a host medium of local (frequency-dependent) dielectric function ϵ_2, we expand the screened interaction $W(\boldsymbol{r}, \boldsymbol{r}'; \omega)$ in terms of the modified Bessel functions $I_m(x)$ and $K_m(x)$ [241], as follows:

$$W(\boldsymbol{r}, \boldsymbol{r}'; \omega) = \frac{2}{\pi} \int_0^\infty \mathrm{d}q_z \, \cos\left[q_z(z - z')\right] \times \sum_{m=0}^{\infty} \mu_m \, W_m(\rho, \rho'; \omega) \cos\left[m(\phi - \phi')\right], \tag{7.19}$$

where z and ρ represent the projections of the position vector along the axis of the cylinder and in a plane perpendicular to the cylinder, respectively, q_z denotes the magnitude of a wave vector along the axis of the cylinder and m_m are Neumann numbers

$$\mu_m = \begin{cases} 1, & m = 0, \\ 2, & m \geqslant 1. \end{cases} \tag{7.20}$$

The coefficients $W_m(\rho, \rho'; \omega)$ are then derived by imposing the boundary conditions, i.e. by requiring that the total scalar potential and the normal component of the displacement vectors be continuous at the interface. One finds:

$$W_m(\rho, \rho'; \omega) = \begin{cases} I_m(q_z\rho^<) \left[K_m(q_z\rho^>) - K'_m(x)\, g_m\, I_m(q_z\rho^>)/I'_m(x)\right]/\epsilon_1, & \rho, \rho' < a, \\ \left[x\, I'_m(x)\, K_m(x)\right]^{-1} g_m\, I_m(q_z\rho^<)\, K_m(q_z\rho^>)/(\epsilon_1 - \epsilon_2), & \rho^< < a, \rho^> > a, \\ \left[I_m(q_z\rho^<) - I_m(x)\, g_m\, K_m(q_z\rho^<)/K_m(x)\right] K_m(q_z\rho^>)/\epsilon_2, & \rho, \rho' > a, \end{cases} \tag{7.21}$$

where $x = q_z a$ and

$$g_m(x, \omega) = \frac{I'_m(x)\, K_m(x)\, [\epsilon_1(\omega) - \epsilon_2(\omega)]}{I'_m(x)\, K_m(x)\, \epsilon_1(\omega) - I_m(x)\, K'_m(x)\, \epsilon_2(\omega)}, \tag{7.22}$$

or, equivalently,

$$g_m(x, \omega) = -\frac{n_m}{u - n_m}, \tag{7.23}$$

with u being the spectral variable of equation (3.44) and

$$n_m = x\, I'_m(x)\, K_m(x). \tag{7.24}$$

In the limit as $x \to 0$ (p-polarization)[15], the depolarization factors of equation (7.24) are easily found to be $n_0 = 0$ (corresponding to the plasmon condition $\epsilon_2 = 0$)[16] and $n_m = 1/2$

[15] As we are considering longitudinal fields, where the electric field $\mathbf{E}$ and the wave vector $\mathbf{q}$ have the same direction, in the limit as $x = q_z a \to 0$ the electric field lies in the plane perpendicular to the axis of the cylinder.

[16] This mode, however, does not contribute to the effective inverse dielectric function and, therefore, to the energy loss of moving charged particles, since when $x = q_z a = 0$ (p-polarization) the strength of this mode is equal to zero for all values of the total wave vector Qa (see [183]).

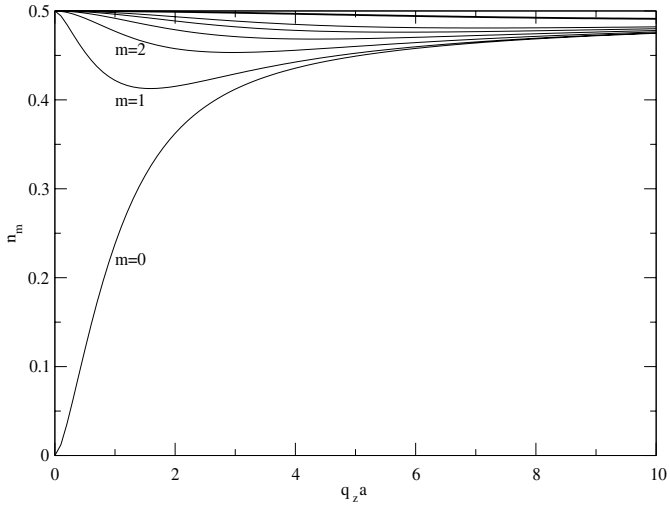

Figure 7. Depolarization factors $n_m = x\, I'_m(x)\, K_m(x)$, as a function of $x = q_z a$, for $m = 0, 1, 2, 3, 4, 5$ (thin solid lines), and $m = 10$ (thick solid line). As $m \to \infty$, the depolarization factor n_m equals the planar surface-plasmon value $n_m = 1/2$ for all values of $x = q_z a$.

(corresponding to the planar surface-plasmon condition $\epsilon_1 + \epsilon_2 = 0$) for all $m \neq 0$; in the limit as $x \to \infty$, equation (7.24) yields $n_m = 1/2$ for all m. For the behaviour of the depolarization factors n_m of equation (7.24) as a function of x see figure 7. This figure shows that the energies of all modes are rather close to the planar surface-plasmon energy (corresponding to $n_m = 1/2$), except for $m = 0$. The $m = 0$ mode, which corresponds to a homogeneous charge distribution around the cylindrical surface, shifts downwards from the planar surface-plasmon energy ($n_0 = 1/2$) as the adimensional quantity $x = q_z a$ decreases, as occurs with the symmetric low-energy mode in thin films (see equations (2.26) and (2.27)).

Introducing equations (7.19)–(7.22) into equation (7.5), one finds the following expression for the effective inverse dielectric function [182]:

$$\epsilon_{\rm eff}^{-1}(\boldsymbol{Q}, \omega) = \epsilon_2^{-1} + f\,(\epsilon_1^{-1} - \epsilon_2^{-1}) \left[1 + \frac{2}{x^2 + y^2} \sum_{m=0}^{\infty} \mu_m J_m(y) g_m \Theta_m(x, y) \right], \tag{7.25}$$

where

$$\Theta_m(x, y) = \frac{I'_m(x)\, f_m^{(1)}(x, y)\, \epsilon_1 + K'_m(x)\, f_m^{(2)}(x, y)\, \epsilon_2}{I'_m(x)\, K_m(x)\, [\epsilon_1 - \epsilon_2]}, \tag{7.26}$$

$$f_m^{(1)}(x, y) = x\, J_m(y)\, K_{m-1}(x) + y\, J_{m-1}(y)\, K_m(x), \tag{7.27}$$

$$f_m^{(2)}(x, y) = x\, J_m(y)\, I_{m-1}(x) - y\, J_{m-1}(y)\, I_m(x), \tag{7.28}$$

$x = q_z a$, and $y = qa$, q_z and q representing the components of the total wave vector $\boldsymbol{Q}$ along the axis of the cylinder and in a plane perpendicular to the cylinder, respectively. The volume fraction filled by the cylinder is denoted by f, and $J_m(x)$ are cylindrical Bessel functions of the first kind [241]. A spectral representation of the effective inverse dielectric function of equations (7.25)–(7.28) was reported in [183].

In the limit as $Qa \ll 1$, an expansion of equations (7.25)–(7.28) yields

$$\epsilon_{\text{eff}}^{-1}(\boldsymbol{Q},\omega) = \epsilon_2^{-1}\left\{1 - f\,\frac{\epsilon_1-\epsilon_2}{x^2+y^2}\left[\frac{x^2}{\epsilon_2} + 2\,\frac{y^2}{\epsilon_1+\epsilon_2}\right]\right\}, \tag{7.29}$$

which admits the spectral representation of equation (3.46) with two nonvanishing spectra strengths: $C_0 = x^2/(x^2+y^2)$ and $C_1 = y^2/(x^2+y^2)$, the corresponding depolarization factors being $n_0 = 0$ and $n_1 = 1/2$, respectively.

Equation (7.29) demonstrates that in the limit as $Qa \ll 1$ and for a wave vector normal to the cylinder ($x = 0$), moving charged particles can only create collective excitations at the dipole resonance where $n_1 = 1/2$, i.e. $\epsilon_1 + \epsilon_2 = 0$, which for a Drude cylinder in vacuum yields Ritchie's frequency $\omega_{\text{s}} = \omega_{\text{p}}/\sqrt{2}$. Conversely, still in the limit as $Qa \ll 1$ but for a wave vector along the axis of the cylinder ($y = 0$), moving charged particles can only excite the bulk mode of the host medium dictated by the condition $u = 0$ (corresponding to $n_0 = 0$), i.e. $\epsilon_2 = 0$, in agreement with the discussion of section 3.2.3 (Simple geometries).

7.2. Nonlocal models: planar surface

Nonlocal effects that are absent in the classical model described above can be incorporated in a variety of semiclassical and quantal approaches, which we here only describe for a *planar surface*.

7.2.1. Hydrodynamic model.

Semiclassical hydrodynamic approach. Within a semiclassical hydrodynamic approach, the screened interaction $W(\boldsymbol{r},\boldsymbol{r}';\omega)$ (as defined in equation (7.1)) can be obtained from the linearized hydrodynamic equations (3.22)–(3.24). For a semi-infinite metal in vacuum consisting of an abrupt step of the unperturbed electron density $n_0(z)$ (see equation (3.25)), we can assume translational invariance in the plane of the surface, and noting that the normal component of the hydrodynamical velocity should vanish at the interface equations (3.22)–(3.24) yield the following expression for the 2D Fourier transform $W(z,z';q,\omega)$:

$$W(z,z';q,\omega) = \frac{2\pi}{q}\begin{cases} \epsilon_{\text{s}}(z-z') + \epsilon_{\text{s}}(z+z') - 2\,g\,\dfrac{\epsilon_{\text{s}}(z)\,\epsilon_{\text{s}}(z')}{1-\epsilon_{\text{s}}^0}, & z<0,\ z'<0, \\ 2\,g\,\dfrac{\epsilon_{\text{s}}(z^<)}{1-\epsilon_{\text{s}}^0}\,\mathrm{e}^{-qz^>}, & z^<<0,\ z^>>0, \\ \mathrm{e}^{-q|z-z'|} - g\,\mathrm{e}^{-q(z+z')}, & z>0,\ z'>0, \end{cases} \tag{7.30}$$

where $z^<$ ($z^>$) is the smallest (largest) of z and z',

$$\epsilon_{\text{s}}(z;q,\omega) = \frac{\Lambda\,\omega\,(\omega+\mathrm{i}\eta)\,\mathrm{e}^{-q|z|} - q\,\omega_{\text{p}}^2\,\mathrm{e}^{-\Lambda|z|}}{\Lambda\left[\omega(\omega+\mathrm{i}\eta) - \omega_{\text{p}}^2\right]}, \tag{7.31}$$

$$g(q,\omega) = \frac{\omega_{\text{p}}^2}{2\beta^2\,\Lambda(\Lambda+q) - \omega_{\text{p}}^2}, \tag{7.32}$$

$$\Lambda = \frac{1}{\beta}\sqrt{\omega_{\text{p}}^2 + \beta^2 q^2 - \omega(\omega+\mathrm{i}\eta)}, \tag{7.33}$$

$\beta = \sqrt{1/3}(3\pi^2 n_0)^{1/3}$ (as in equations (3.29) and (3.30)) and

$$\epsilon_{\rm s}^0(q,\omega) = \epsilon_{\rm s}(z=0;q,\omega). \tag{7.34}$$

An inspection of equations (7.30)–(7.34) shows that the hydrodynamic surface-response function $g(q,\omega)$ and, therefore, the hydrodynamic screened interaction $W(z,z';q,\omega)$ become singular at the hydrodynamic surface-plasmon condition dictated by equation (3.30). We also note that the second moment of the imaginary part of the hydrodynamic surface-response function $g(q,\omega)$ is found to be

$$\int_{-\infty}^{\infty} {\rm d}\omega\, \omega\, {\rm Im}\, g(q,\omega) = 2\pi^2\, \bar{n}, \tag{7.35}$$

where $\bar{n}$ represents the electron density: $\bar{n} = \omega_{\rm p}^2/4\pi$.

Finally, we note that in the long-wavelength ($q \to 0$) limit the hydrodynamic screened interaction of equations (7.30)–(7.34) reduces to the *classical* screened interaction of equations (7.8) and (7.9) with the dielectric functions ϵ_1 and ϵ_2 being replaced by the Drude dielectric function (equation (2.15)) and unity, respectively. The same result is also obtained by simply assuming that the electron gas is nondispersive, i.e. by taking the hydrodynamic speed β equal to zero.

Quantum hydrodynamic approach. Within a quantized hydrodynamic model of a many-electron system, one first linearizes the hydrodynamic Hamiltonian with respect to the induced electron density and then quantizes this Hamiltonian on the basis of the normal modes of oscillation (bulk and surface plasmons) corresponding to equations (3.29) and (3.30). One finds

$$H = H_{\rm G} + H_0^{\rm B} + H_0^{\rm S}, \tag{7.36}$$

where $H_{\rm G}$ represents the Thomas–Fermi ground state of the static unperturbed electron system [176], and $H_0^{\rm B}$ and $H_0^{\rm S}$ are free bulk and surface plasmon Hamiltonians, respectively:

$$H_0^{\rm B} = \frac{1}{\Omega} \sum_{\boldsymbol{q},q_z} \left[1/2 + \omega_Q^{\rm B}\right] a_{\boldsymbol{Q}}^\dagger(t) a_{\boldsymbol{Q}}(t) \tag{7.37}$$

and

$$H_0^{\rm S} = \frac{1}{A} \sum_{\boldsymbol{q}} \left[1/2 + \omega_q^{\rm S}\right] b_{\boldsymbol{q}}^\dagger(t) b_{\boldsymbol{q}}(t). \tag{7.38}$$

Here, Ω and A represent the normalization volume and the normalization area of the surface, respectively, $a_{\boldsymbol{Q}}(t)$ and $b_{\boldsymbol{q}}(t)$ are Bose–Einstein operators that annihilate bulk and surface plasmons with wave vectors $\boldsymbol{Q} = (\boldsymbol{q}, q_z)$ and $\boldsymbol{q}$, respectively, and $\omega_Q^{\rm B}$ and $\omega_q^{\rm S}$ represent the dispersion of bulk and surface plasmons:

$$\left(\omega_Q^{\rm B}\right)^2 = \omega_{\rm p}^2 + \beta^2\, Q^2 \tag{7.39}$$

and

$$\left(\omega_q^{\rm S}\right)^2 = \frac{1}{2}\left[\omega_{\rm p}^2 + \beta^2\, q^2 + \beta\, q \sqrt{2\omega_{\rm p}^2 + \beta^2\, q^2}\right]. \tag{7.40}$$

Hence, within this approach one can distinguish the separate contributions to the imaginary part of the hydrodynamic surface-response function $g(q,\omega)$ of equation (7.32) coming from the excitation of either bulk or surface plasmons. One finds [243]

$${\rm Im}\, g(q,\omega) = {\rm Im}\, g^{\rm B}(q,\omega) + {\rm Im}\, g^{\rm S}(q,\omega), \tag{7.41}$$

where

$$\operatorname{Im} g^{\mathrm{B}}(q,\omega) = \frac{1}{2}\, q \int_0^\infty \mathrm{d}q_z\, \delta(\omega - \omega_Q^{\mathrm{B}}) \frac{(\omega_{\mathrm{p}}^2/\omega_Q^{\mathrm{B}})\, q_z^2}{q_z^4 + q_z^2(q^2 + \omega_{\mathrm{p}}^2/\beta^2) + \omega_{\mathrm{p}}^4/(4\beta^4)} \tag{7.42}$$

and

$$\operatorname{Im} g^{\mathrm{S}}(q,\omega) = \frac{\pi}{2}\, \frac{\gamma_q}{q + 2\gamma_q}\, \frac{\omega_{\mathrm{p}}^2}{\omega_q^{\mathrm{S}}}\, \delta(\omega - \omega_q^{\mathrm{S}}), \tag{7.43}$$

with $Q = \sqrt{q^2 + q_z^2}$ and

$$\gamma_q = \frac{1}{2\beta}\left(-\beta q + \sqrt{2\omega_{\mathrm{p}}^2 + \beta^2 q^2}\right). \tag{7.44}$$

For the second moments of $\operatorname{Im} g^{\mathrm{B}}(q,\omega)$ and $\operatorname{Im} g^{\mathrm{S}}(q,\omega)$, one finds

$$\int_0^\infty \mathrm{d}\omega\, \omega \operatorname{Im} g^{\mathrm{B}}(q,\omega) = \frac{\pi}{4}\, \frac{q}{q + 2\gamma_q}\, \omega_{\mathrm{p}}^2 \tag{7.45}$$

and

$$\int_0^\infty \mathrm{d}\omega\, \omega \operatorname{Im} g^{\mathrm{S}}(q,\omega) = \frac{\pi}{4}\, \frac{2\gamma_q}{q + 2\gamma_q}\, \omega_{\mathrm{p}}^2, \tag{7.46}$$

which add up to the second moment of equation (7.35).

In the limit as $q \to 0$ the bulk contribution to the so-called energy-loss function $\operatorname{Im} g(q,\omega)$ (see equations (7.41)–(7.44)) vanishes, and the imaginary part of both equations (7.32) and (7.43) yields the classical result:

$$\operatorname{Im} g(q,\omega) \to \frac{\pi}{2}\, \omega_{\mathrm{s}}\, \delta(\omega - \omega_{\mathrm{s}}), \tag{7.47}$$

which can also be obtained from equation (7.9) with ϵ_1 replaced by the Drude dielectric function of equation (2.15) and ϵ_2 set equal to unity. Equation (7.47) shows that in the classical (long-wavelength) limit the energy loss is dominated by the excitation of surface plasmons of energy $\omega_{\mathrm{s}} = \omega_{\mathrm{p}}/\sqrt{2}$, as predicted by Ritchie.

7.2.2. Specular-reflection model (SRM). An alternative scheme to incorporate *nonlocal* effects, which has the virtue of expressing the screened interaction $W(z, z'; q, \omega)$ in terms of the dielectric function $\epsilon(Q,\omega)$ of a homogeneous electron gas representing the bulk material, is the so-called specular-reflection model reported independently by Wagner [179] and by Ritchie and Marusak [180]. In this model, the medium is described by an electron gas in which all electrons are considered to be specularly reflected at the surface, thereby the electron density vanishing outside.

For a semi-infinite metal in vacuum, the unperturbed electron density $n_0(z)$ is taken to be of the form of equation (3.25), and the SRM yields a screened interaction of the form of equation (7.30) but with the quantities $\epsilon_{\mathrm{s}}(z; q, \omega)$ and $g(q,\omega)$ being replaced by the more general expressions:

$$\epsilon_{\mathrm{s}}(z; q, \omega) = \frac{q}{\pi} \int_{-\infty}^{+\infty} \frac{\mathrm{d}q_z}{Q^2}\, \mathrm{e}^{\mathrm{i}q_z z} \epsilon^{-1}(Q,\omega) \tag{7.48}$$

and

$$g(q,\omega) = \frac{1-\epsilon_{\rm s}^0(q,\omega)}{1+\epsilon_{\rm s}^0(q,\omega)}, \tag{7.49}$$

with $\epsilon_{\rm s}^0(q,\omega)$ defined as in equation (7.34), and $Q = \sqrt{q^2+q_z^2}$.

The inverse dielectric function $\epsilon^{-1}(Q,\omega)$ entering equation (7.48) represents the 3D Fourier transform of the inverse dielectric function $\epsilon^{-1}(\boldsymbol{r},\boldsymbol{r}';\omega)$ of a homogeneous electron gas. From equation (6.3), one finds

$$\epsilon^{-1}(Q,\omega) = 1 + v_Q\,\chi(Q,\omega), \tag{7.50}$$

where $\chi(Q,\omega)$ represents the 3D Fourier transform of the density-response function $\chi(\boldsymbol{r},\boldsymbol{r}';\omega)$.

In the framework of TDDFT, one uses equation (5.11) to find

$$\chi(Q,\omega) = \chi^0(Q,\omega) + \chi^0(Q,\omega) \times \left\{v_Q + f_{\rm xc}(\bar{n};\,Q,\omega)\right\}\,\chi(Q,\omega), \tag{7.51}$$

with $\chi^0(Q,\omega)$ and $f_{\rm xc}(\bar{n};\,Q,\omega)$ being the 3D Fourier transforms of the noninteracting density-response function and the XC kernel of equations (5.7) and (5.15), respectively. For a homogeneous electron gas, the eigenfunctions $\psi_{\rm i}(\boldsymbol{r})$ entering equation (5.7) are all plane waves; thus, the integrations can be carried out analytically to yield the well-known Lindhard function $\chi^0(Q,\omega)$ [244]. If one sets the XC kernel $f_{\rm xc}(\bar{n};\,Q,\omega)$ equal to zero, introduction of equation (7.51) into equation (7.50) yields the RPA dielectric function

$$\epsilon^{\rm RPA}(Q,\omega) = 1 - v_Q\,\chi^0(Q,\omega), \tag{7.52}$$

which is easy to evaluate.

The RPA dielectric function $\epsilon^{\rm RPA}(Q,\omega)$ of a homogeneous electron gas can be further approximated in the framework of the hydrodynamic scheme described in section 3.1.3. One finds

$$\epsilon^{\rm hydro}(Q,\omega) = 1 + \frac{\omega_{\rm p}^2}{\beta^2 Q^2 - \omega(\omega+{\rm i}\eta)}, \tag{7.53}$$

which in the classical (long-wavelength) limit yields the *local* Drude dielectric function of equation (2.15). Introduction of equation (7.53) into equation (7.48) yields the hydrodynamic screened interaction of equations (7.30)–(7.34).

We know from equation (7.1) that collective excitations are dictated by singularities in the screened interaction or, equivalently, maxima in the imaginary part of this quantity. For z and z' coordinates well inside the solid ($z,\,z' \to -\infty$), one finds

$$W^{\rm in}(z,z';q,\omega) = \int_{-\infty}^{\infty}\frac{{\rm d}q_z}{2\pi}\,{\rm e}^{{\rm i}q_z(z-z')}\,v_Q\,\epsilon^{-1}(Q,\omega), \tag{7.54}$$

which in the case of the Drude dielectric function $\epsilon(Q,\omega)$ of equation (2.15) and for positive frequencies ($\omega > 0$) yields

$${\rm Im}\,W^{\rm in}(z,z';q,\omega) \to -\frac{\pi^2}{q}\,\omega_{\rm p}\,\delta(\omega-\omega_{\rm p})\,{\rm e}^{-q|z-z'|}. \tag{7.55}$$

For z and z' coordinates both outside the solid ($z,\,z' > 0$), one finds

$$W^{\rm out}(z,z';q,\omega) = \frac{2\pi}{q}\left[{\rm e}^{-q|z-z'|} - g(q,\omega)\,{\rm e}^{-q(z+z')}\right], \tag{7.56}$$

which in the classical ($q \to 0$) limit and for positive frequencies ($\omega > 0$) yields

$${\rm Im}\,W^{\rm out}(z,z';q,\omega) \to -\frac{\pi^2}{q}\,\omega_{\rm s}\,\delta(\omega-\omega_{\rm s})\,{\rm e}^{-q(z+z')}. \tag{7.57}$$

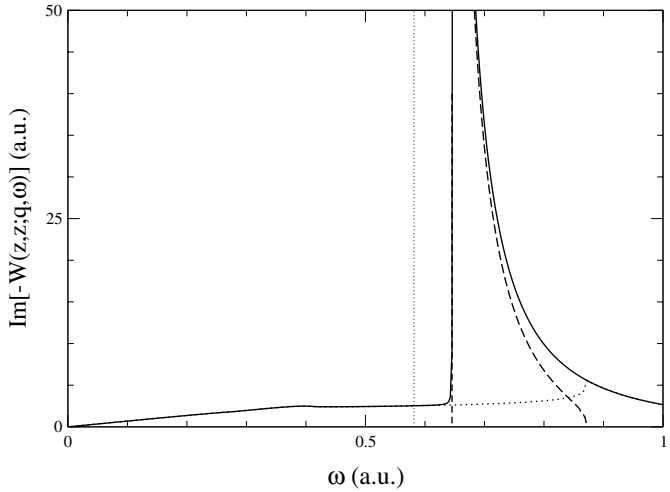

Figure 8. The solid line represents the energy-loss function, $\mathrm{Im}[-W(z, z'; q, \omega)]$, versus ω, as obtained at $z = z'$, $q = 0.4q_{\mathrm{F}}$, and $r_{\mathrm{s}} = 2.07$ from equation (7.54) by using the full RPA dielectric function $\epsilon^{\mathrm{RPA}}(Q, \omega)$. The thick dashed and dotted lines represent separate contributions from the excitation of *bulk* collective modes and e–h pairs occurring at energies $\omega^{\mathrm{B}}_{Q=q} < \omega < \omega^{\mathrm{B}}_{Q=Q_{\mathrm{c}}}$ and $\omega \leqslant qq_{\mathrm{F}} + q^2/2$, respectively. The vertical dotted line represents the energy $\omega_{\mathrm{p}} = 15.8\,\mathrm{eV}$ at which collective oscillations would occur in a Drude metal.

Figures 8 and 9 show the energy-loss function $\mathrm{Im}[-W(z, z'; q, \omega)]$ that we have obtained at $z = z'$, $q = 0.4q_{\mathrm{F}}$ and $r_{\mathrm{s}} = 2.07$ from equations (7.54) and (7.56), respectively, by using the full RPA dielectric function $\epsilon^{\mathrm{RPA}}(Q, \omega)$. For z coordinates well inside the solid (figure 8), instead of the single *classical* collective excitation at ω_{p} (dotted vertical line) predicted by equation (7.55) the RPA energy-loss spectrum (solid line) is composed of (i) a continuum of bulk collective excitations (dashed line) occurring at energies $\omega^{\mathrm{B}}_{Q=q} < \omega < \omega^{\mathrm{B}}_{Q=Q_{\mathrm{c}}}$[17] and (ii) the excitation of electron–hole (e–h) pairs represented by a thick dotted line.

For z coordinates that are outside the surface, it had been generally believed that only surface plasmons and e–h pairs can be excited. However, it was shown explicitly in [243,245] that the continuum of bulk-plasmon excitations dominating the energy-loss spectrum inside the solid (see figure 8) is still present for z coordinates outside, as shown in figure 9 for $z = z' = \lambda_{\mathrm{F}}$[18]. This continuum, which covers the excitation spectrum at energies $\omega \geqslant \omega^{\mathrm{B}}_{Q=q}$ and is well separated from the lower-energy spectrum arising from the excitation of surface plasmons and e–h pairs, is accurately described by using the quantal hydrodynamic surface energy-loss function of equation (7.42), which has been represented in figure 9 by a thick dotted line.

Nonetheless, the main contribution to the energy-loss spectrum outside the solid comes from the excitation of surface plasmons, which are damped by the presence of e–h pairs. These e–h pair excitations are not present in the classical and hydrodynamic schemes described above, which predict the existence of long-lived surface plasmons at the energies represented in figure 9 by thin dotted vertical lines: $\omega_{\mathrm{s}} = \omega_{\mathrm{p}}/\sqrt{2}$ (see equation (7.57)) and ω^{S}_q of equation (7.40) (see equations (7.43)–(7.44)), respectively.

[17] ω^{B}_Q denotes the energy of bulk plasmons with momentum Q, and Q_{c} denotes the critical momentum for which the bulk-plasmon dispersion ω^{B}_Q enters the electron–hole pair excitation spectrum. For $r_{\mathrm{s}} = 2.07$ and $Q = 0.4q_{\mathrm{F}}$, the RPA values of ω^{B}_Q and $\omega^{\mathrm{B}}_{Q_{\mathrm{c}}}$ are 17.6 eV and 23.6 eV, respectively.

[18] The Fermi wavelength λ_{F} is defined as follows: $\lambda_{\mathrm{F}} = 2\pi/q_{\mathrm{F}}$, q_{F} being the magnitude of the Fermi wave vector.

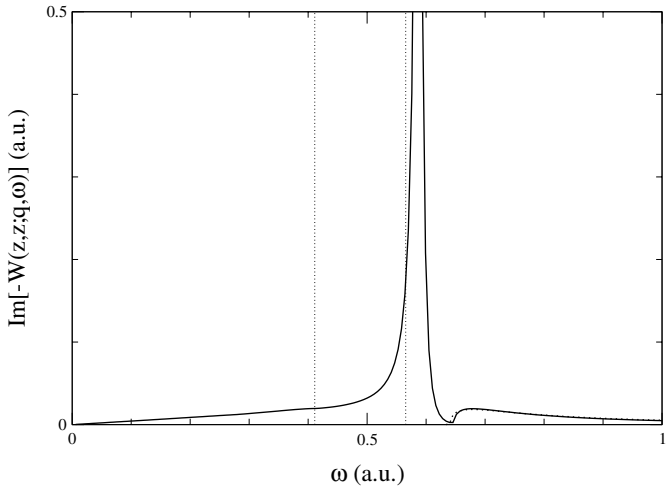

Figure 9. The solid line represents the energy-loss function, $\mathrm{Im}[-W(z,z';q,\omega)]$, versus ω, as obtained at $z = z' = \lambda_{\mathrm{F}}$, $q = 0.4q_{\mathrm{F}}$, and $r_{\mathrm{s}} = 2.07$ from equation (7.56) by using the full RPA dielectric function $\epsilon^{\mathrm{RPA}}(Q,\omega)$. The thick dotted line, which is nearly indistinguishable from the solid line covering the same part of the spectrum, represents the hydrodynamic prediction from equation (7.42). The thin dotted vertical lines represent the energies $\omega_{\mathrm{s}} = 11.2\,\mathrm{eV}$ and $\omega_Q^{\mathrm{S}} = 15.4\,\mathrm{eV}$ of equation (7.40) at which long-lived surface plasmons would occur in a semi-infinite metal described by a Drude and a hydrodynamic model, respectively. Introduction of the full RPA dielectric function $\epsilon^{\mathrm{RPA}}(Q,\omega)$ into equation (7.49) yields a maximum of the surface-loss function $\mathrm{Im}g(q,\omega)$ (and, therefore, $\mathrm{Im}[-W(z,z';q,\omega)]$) at the surface-plasmon energy $\omega_Q^{\mathrm{S}} = 16.0\,\mathrm{eV}$, which is slightly larger than its hydrodynamic counterpart.

7.2.3. Self-consistent scheme. For an accurate quantal description of the electronic excitations that can occur in a semi-infinite metal, we need to consider the true density-response function $\chi(\boldsymbol{r},\boldsymbol{r}';\omega)$ entering equation (7.4), which is known to fulfil the f-sum rule of equation (5.3).

Jellium surface. In the case of a free-electron gas bounded by a semi-infinite positive background of density

$$n_+(z) = \begin{cases} \bar{n}, & z \leqslant 0, \\ \\ 0, & z > 0, \end{cases} \tag{7.58}$$

translationally invariance in the plane of the surface allows one to define the 2D Fourier transform $W(z,z';q,\omega)$, which according to equation (7.4) can be obtained as follows:

$$W(z,z';q,\omega) = v(z,z';q) + \int \mathrm{d}z_1 \int \mathrm{d}z_2\, v(z,z_1;q)\chi(z_1,z_2;q,\omega)\, v(z_2,z';q), \tag{7.59}$$

where $v(z,z';q)$ is the 2D Fourier transform of the bare Coulomb interaction $v(\boldsymbol{r},\boldsymbol{r}')$:

$$v(z,z';q) = \frac{2\pi}{q}\,\mathrm{e}^{-q|z-z'|}, \tag{7.60}$$

and $\chi(z,z';q,\omega)$ denotes the 2D Fourier transform of the interacting density-response function $\chi(\boldsymbol{r},\boldsymbol{r}';\omega)$. In the framework of TDDFT, one uses equation (5.11) to find

$$\chi(z,z';q,\omega) = \chi^0(z,z';q,\omega) + \int \mathrm{d}z_1 \int \mathrm{d}z_2\, \chi^0(z,z_1;q,\omega) \times \{v(z_1,z_2;q) + f_{\mathrm{xc}}[n_0](z_1,z_2;q,\omega)\}\,\chi(z_2,z';q,\omega), \tag{7.61}$$

where $\chi^0(z,z';q,\omega)$ and $f_{\rm xc}[n_0](z,z';q,\omega)$ denote the 2D Fourier transforms of the noninteracting density-response function $\chi^0(\boldsymbol{r},\boldsymbol{r}';\omega)$ and the XC kernel $f_{\rm xc}[n_0](\boldsymbol{r},\boldsymbol{r}';\omega)$, respectively. Using equation (5.7), and noting that the single-particle orbitals $\psi_i(\boldsymbol{r})$ now take the form

$$\psi_{\boldsymbol{k},i}(\boldsymbol{r}) = \mathrm{e}^{\mathrm{i}\boldsymbol{k}\cdot\boldsymbol{r}_\parallel}\,\psi_i(z), \tag{7.62}$$

one finds

$$\chi^0(z,z';q,\omega) = \frac{2}{A}\sum_{i,j}\psi_i(z)\psi_j^*(z)\psi_j(z')\psi_i^*(z')\sum_{\boldsymbol{k}}\frac{f_{\boldsymbol{k},i}-f_{\boldsymbol{k}+\boldsymbol{q},j}}{E_{\boldsymbol{k},i}-E_{\boldsymbol{k}+\boldsymbol{q},j}+\omega+\mathrm{i}\eta}, \tag{7.63}$$

where

$$E_{\boldsymbol{k},i} = \varepsilon_i + \frac{k^2}{2}, \tag{7.64}$$

the single-particle orbitals $\psi_i(z)$ and energies ε_i now being the solutions of the one-dimensional Kohn–Sham equation

$$\left[-\frac{1}{2}\frac{\mathrm{d}^2}{\mathrm{d}z^2} + v_{\rm KS}[n_0](z)\right]\psi_i(z) = \varepsilon_i\,\psi_i(z), \tag{7.65}$$

with

$$v_{\rm KS}[n_0](z) = v_{\rm H}[n_0](z) + v_{\rm xc}[n_0](z), \tag{7.66}$$

$$v_{\rm H}(z) = -2\pi\int_{-\infty}^{\infty}\mathrm{d}z'\,|z-z'|\,\left[n_0(z')-n_+(z')\right], \tag{7.67}$$

$$v_{\rm xc}[n_0](z) = \left.\frac{\delta E_{\rm xc}[n]}{\delta n(z)}\right|_{n=n_0}, \tag{7.68}$$

and

$$n_0(z) = \frac{1}{\pi}\sum_i(\varepsilon_{\rm F}-\varepsilon_i)\,\psi_i^2(z)\,\theta(\varepsilon_{\rm F}-\varepsilon_i). \tag{7.69}$$

From equation (5.3), the imaginary part of the density-response function $\chi(z,z';q,\omega)$ is easily found to fulfil the following sum rule:

$$\int_{-\infty}^{\infty}\mathrm{d}\omega\,\omega\,\mathrm{Im}\,\chi(z,z';q,\omega) = -\pi\left[q^2+\frac{\mathrm{d}^2}{\mathrm{d}z\mathrm{d}z'}\right]n_0(z)\,\delta(z-z'). \tag{7.70}$$

Within this scheme, the simplest possible approximation is to neglect XC effects altogether and set the XC potential $v_{\rm xc}[n_0](z)$ and kernel $f_{\rm xc}[n_0](z,z';q,\omega)$ equal to zero. In this case, the one-dimensional single-particle wave functions $\psi_i(z)$ and energies ε_i are the self-consistent eigenfunctions and eigenvalues of a one-dimensional Hartree Hamiltonian. The calculation of the density-response function is further simplified if the Hartree potential $v_{\rm H}[n_0](z)$ of equation (7.67) is replaced by

$$v_{\rm IBM}(z) = \begin{cases} v_0, & z \leqslant z_0, \\ \\ \infty, & z > z_0, \end{cases} \tag{7.71}$$

where the value $z_0 = (3/16)\lambda_{\rm F}$ is chosen so as to ensure charge neutrality. This is the so-called inifinite-barrier model (IBM) [246], in which the single-particle orbitals $\psi_i(z)$ are simply sines. If one further neglects interference between incident and scattered electrons at the surface, this model yields the classical IBM (CIBM) [247] which can be shown to be equivalent to the SRM described in section 7.2.2.

Alternatively, and with the aim of incorporating band-structure effects (such as the presence of energy gaps and surface states) approximately, the self-consistent jellium-like Kohn–Sham potential of equation (7.66) can be replaced by a physically motivated model potential $v_{\rm MP}(z)$. Examples are the parametrized model potential reported by Chulkov *et al* [248], which was successful in the description of the lifetimes of image and Shockley states in a variety of metal surfaces [249–255], and the q-dependent model potential that has been reported recently to investigate the momentum-resolved lifetimes of Shockley states at the Cu(111) surface [256].

At this point, we note that for z and z' coordinates that are far from the surface into the vacuum, where the electron density vanishes, equation (7.59) takes the form of equation (7.56) (which within the SRM is true for all $z, z' > 0$), i.e.

$$W(z, z'; q, \omega) = v(z, z'; q) - \frac{2\pi}{q}\, \mathrm{e}^{-q(z+z')}\, g(q, \omega), \tag{7.72}$$

but with the surface-response function $g(q, \omega)$ now being given by the general expression [257]:

$$g(q, \omega) = -\frac{2\pi}{q} \int \mathrm{d}z_1 \int \mathrm{d}z_2\, \mathrm{e}^{q(z_1+z_2)}\, \chi(z_1, z_2; q, \omega), \tag{7.73}$$

which according to equation (5.1) can be expressed as follows

$$g(q, \omega) = \int \mathrm{d}z\, \mathrm{e}^{qz}\, \delta n(z; q, \omega), \tag{7.74}$$

with $\delta n(z; q, \omega)$ being the electron density induced by an external potential of the form

$$\phi^{\rm ext}(z; q, \omega) = -\frac{2\pi}{q}\, \mathrm{e}^{qz}. \tag{7.75}$$

In the framework of TDDFT, the induced electron density is obtained as in the RPA (see equation (5.5)), but with the XC kernel $f_{\rm xc}[n_0](\boldsymbol{r}, \boldsymbol{r}'; q, \omega)$ added to the bare Coulomb interaction $v(\boldsymbol{r}, \boldsymbol{r}')$. Hence, after Fourier transforming one writes

$$\delta n(z; q, \omega) = \int \mathrm{d}z'\, \chi^0(z, z'; q, \omega)\{\phi^{\rm ext}(z'; q, \omega) + \int \mathrm{d}z'' \times \left[v(z', z''; q) + f_{\rm xc}[n_0](z', z''; q, \omega)\right] \delta n(z''; q, \omega)\}. \tag{7.76}$$

Using equations (7.70) and (7.73), the surface loss function $\mathrm{Im}g(q, \omega)$ is easily found to fulfil the following sum rule:

$$\int_0^\infty \mathrm{d}\omega\, \omega\, \mathrm{Im}g(q, \omega) = 2\pi^2\, q \int \mathrm{d}z\, \mathrm{e}^{2qz}\, n_0(z), \tag{7.77}$$

which for a step-like electron density $n_0(z)$ of the form of equation (3.25) reduces to equation (7.35), as expected.

Periodic surface. For a periodic surface, single-particle wave functions are of the form

$$\psi_{\boldsymbol{k},n;i}(\boldsymbol{r}) = \psi_{\boldsymbol{k},n}(\boldsymbol{r}_\parallel)\, \psi_i(z), \tag{7.78}$$

where $\psi_{\boldsymbol{k},n}(\boldsymbol{r}_\parallel)$ are Bloch states:

$$\psi_{\boldsymbol{k},n}(\boldsymbol{r}_\parallel) = \frac{1}{\sqrt{A}}\, \mathrm{e}^{\boldsymbol{k}\cdot\boldsymbol{r}_\parallel}\, u_{\boldsymbol{k},n}(\boldsymbol{r}_\parallel), \tag{7.79}$$

with $\boldsymbol{r}_\parallel$ and $\boldsymbol{k}$ being 2D vectors in the plane of the surface. Hence, one may introduce the following Fourier expansion of the screened interaction:

$$W(\boldsymbol{r},\boldsymbol{r}';\omega)=\frac{1}{A}\sum_{\boldsymbol{q}}^{\mathrm{SBZ}}\sum_{\boldsymbol{g},\boldsymbol{g}'}\mathrm{e}^{\mathrm{i}(\boldsymbol{q}+\boldsymbol{g})\cdot\boldsymbol{r}_\parallel}\mathrm{e}^{-\mathrm{i}(\boldsymbol{q}+\boldsymbol{g}')\cdot\boldsymbol{r}'_\parallel}W_{\boldsymbol{g},\boldsymbol{g}'}(z,z';\boldsymbol{q},\omega), \tag{7.80}$$

where $\boldsymbol{q}$ is a 2D wave vector in the surface Brillouin zone (SBZ), and $\boldsymbol{g}$ and $\boldsymbol{g}'$ denote 2D reciprocal-lattice vectors. According to equation (7.4), the 2D Fourier coefficients $W_{\boldsymbol{g},\boldsymbol{g}'}(z,z';\boldsymbol{q},\omega)$ are given by the following expression:

$$\begin{aligned}W_{\boldsymbol{g},\boldsymbol{g}'}(z,z';\boldsymbol{q},\omega)&=v_{\boldsymbol{g}}(z,z';\boldsymbol{q})\,\delta_{\boldsymbol{g},\boldsymbol{g}'}+\int\mathrm{d}z_1\int\mathrm{d}z_2\\&\times v_{\boldsymbol{g}}(z,z_1;\boldsymbol{q})\,\chi_{\boldsymbol{g},\boldsymbol{g}'}(z_1,z_2;\boldsymbol{q},\omega)\,v_{\boldsymbol{g}'}(z_2,z';\boldsymbol{q}),\end{aligned} \tag{7.81}$$

where $v_{\boldsymbol{g}}(z,z';\boldsymbol{q})$ denote the 2D Fourier coefficients of the bare Coulomb interaction $v(\boldsymbol{r},\boldsymbol{r}')$:

$$v_{\boldsymbol{g}}(z,z';\boldsymbol{q})=\frac{2\pi}{|\boldsymbol{q}+\boldsymbol{g}|}\,\mathrm{e}^{-|\boldsymbol{q}+\boldsymbol{g}|\,|z-z'|}, \tag{7.82}$$

and $\chi_{\boldsymbol{g},\boldsymbol{g}'}(z,z';\boldsymbol{q},\omega)$ are the Fourier coefficients of the interacting density-response function $\chi(\boldsymbol{r},\boldsymbol{r}';\omega)$. In the framework of TDDFT, one uses equation (5.11) to find:

$$\begin{aligned}\chi_{\boldsymbol{g},\boldsymbol{g}'}(z,z';\boldsymbol{q},\omega)&=\chi^0_{\boldsymbol{g},\boldsymbol{g}'}(z,z';\boldsymbol{q},\omega)+\int\mathrm{d}z_1\int\mathrm{d}z_2\\&\times\chi^0_{\boldsymbol{g},\boldsymbol{g}'}(z,z_1;\boldsymbol{q},\omega)\left[v_{\boldsymbol{g}_1}(z_1,z_2;\boldsymbol{q})\,\delta_{\boldsymbol{g}_1,\boldsymbol{g}_2}+f^{\mathrm{xc}}_{\boldsymbol{g}_1,\boldsymbol{g}_2}[n_0](z_1,z_2;\boldsymbol{q},\omega)\right]\chi_{\boldsymbol{g}_2,\boldsymbol{g}'}(z_2,z';\boldsymbol{q},\omega),\end{aligned} \tag{7.83}$$

where $\chi^0_{\boldsymbol{g},\boldsymbol{g}'}(z,z';\boldsymbol{q},\omega)$ and $f^{\mathrm{xc}}_{\boldsymbol{g},\boldsymbol{g}'}[n_0](z,z';\boldsymbol{q},\omega)$ denote the Fourier coefficients of the noninteracting density-response function $\chi^0(\boldsymbol{r},\boldsymbol{r}';\omega)$ and the XC kernel $f_{\mathrm{xc}}[n_0](\boldsymbol{r},\boldsymbol{r}';\omega)$, respectively. Using equation (5.7), one finds:

$$\begin{aligned}\chi^0_{\boldsymbol{g},\boldsymbol{g}'}(z,z';\boldsymbol{q},\omega)&=\frac{2}{A}\sum_{i,j}\psi_i(z)\psi^*_j(z)\psi_j(z')\psi^*_i(z')\sum_{\boldsymbol{k}}^{\mathrm{SBZ}}\sum_{n,n'}\frac{f_{\boldsymbol{k},n;i}-f_{\boldsymbol{k}+\boldsymbol{q},n';j}}{\varepsilon_{\boldsymbol{k},n;i}-\varepsilon_{\boldsymbol{k}+\boldsymbol{q},n';j}+\hbar(\omega+\mathrm{i}\eta)}\\&\times\langle\psi_{\boldsymbol{k},n}|\mathrm{e}^{-\mathrm{i}(\boldsymbol{q}+\boldsymbol{g})\cdot\boldsymbol{r}_\parallel}|\psi_{\boldsymbol{k}+\boldsymbol{q},n'}\rangle\langle\psi_{\boldsymbol{k}+\boldsymbol{q},n'}|\mathrm{e}^{\mathrm{i}(\boldsymbol{q}+\boldsymbol{g}')\cdot\boldsymbol{r}_\parallel}|\psi_{\boldsymbol{k},n}\rangle,\end{aligned} \tag{7.84}$$

the single-particle orbitals $\psi_{\boldsymbol{k},n;i}(\boldsymbol{r})=\psi_{\boldsymbol{k},n}(\boldsymbol{r}_\parallel)\,\psi_i(z)$ and energies $\varepsilon_{\boldsymbol{k},n;i}$ being the eigenfunctions and eigenvalues of a 3D Kohn–Sham Hamiltonian with an effective potential that is periodic in the plane of the surface.

As in the case of the jellium surface, we can focus on the special situation where both z and z' coordinates are located far from the surface into the vacuum. Equation (7.4) shows that under such conditions the Fourier coefficients $W_{\boldsymbol{g},\boldsymbol{g}'}(z,z';\boldsymbol{q},\omega)$ take the following form:

$$W_{\boldsymbol{g},\boldsymbol{g}'}(z,z';\boldsymbol{q},\omega)=v_{\boldsymbol{g}}(z,z';\boldsymbol{q})\,\delta_{\boldsymbol{g},\boldsymbol{g}'}-\frac{2\pi q}{|\boldsymbol{q}+\boldsymbol{g}|\,|\boldsymbol{q}+\boldsymbol{g}'|}\,g_{\boldsymbol{g},\boldsymbol{g}'}(\boldsymbol{q},\omega)\,\mathrm{e}^{-|\boldsymbol{q}+\boldsymbol{g}|z}\,\mathrm{e}^{-|\boldsymbol{q}+\boldsymbol{g}'|z'}, \tag{7.85}$$

where

$$g_{\boldsymbol{g},\boldsymbol{g}'}(\boldsymbol{q},\omega)=-\frac{2\pi}{q}\int\mathrm{d}z_1\int\mathrm{d}z_2\,\mathrm{e}^{q(z_1+z_2)}\chi_{\boldsymbol{g},\boldsymbol{g}'}(z_1,z_2;\boldsymbol{q},\omega). \tag{7.86}$$

In particular,

$$g_{\boldsymbol{g}=0,\boldsymbol{g}=0}(\boldsymbol{q},\omega) = \int \mathrm{d}z\, \mathrm{e}^{qz}\, \delta n_{\boldsymbol{g}=0}(z;\boldsymbol{q},\omega), \tag{7.87}$$

with $\delta n_{\boldsymbol{g}}(z;\boldsymbol{q},\omega)$ being the Fourier coefficients of the electron density induced by an external potential of the form

$$\phi^{\mathrm{ext}}_{\boldsymbol{g}}(z;\boldsymbol{q},\omega) = -\frac{2\pi}{q}\, \mathrm{e}^{qz}\, \delta_{\boldsymbol{g},\boldsymbol{0}}. \tag{7.88}$$

Finally, one finds from equation (5.3) that the Fourier coefficients $\chi_{\boldsymbol{g},\boldsymbol{g}'}(z,z';\boldsymbol{q},\omega)$ fulfil the following sum rule:

$$\int_{-\infty}^{\infty} \mathrm{d}\omega\, \omega \mathrm{Im}\chi_{\boldsymbol{g},\boldsymbol{g}'}(z,z';\boldsymbol{q},\omega) = -\pi \left[q^2 + \frac{\mathrm{d}^2}{\mathrm{d}z\mathrm{d}z'}\right] n^0_{\boldsymbol{g}-\boldsymbol{g}'}(z;\boldsymbol{q})\, \delta(z-z'), \tag{7.89}$$

where the coefficients $n^0_{\boldsymbol{g}}(z;\boldsymbol{q})$ denote the 2D Fourier components of the ground-state electron density $n_0(\boldsymbol{r})$. Furthermore, combining equations (7.86) and (7.89), one writes

$$\int_0^{\infty} \mathrm{d}\omega\, \omega\, \mathrm{Im} g_{\boldsymbol{g},\boldsymbol{g}'}(q,\omega) = 2\,\pi^2\, q \int \mathrm{d}z\, \mathrm{e}^{2qz}\, n_{\boldsymbol{g}-\boldsymbol{g}'}(z;\boldsymbol{q}), \tag{7.90}$$

which is a generalization of the sum rule of equation (7.35) to the more general case of a real solid in which the crystal structure parallel to the surface is taken into account.

8. Surface-response function

The central quantity that is involved in a description of surface collective excitations is the surface-response function introduced in the preceding section: $g(q,\omega)$ for a jellium surface (see equation (7.73)) and $g_{\boldsymbol{g},\boldsymbol{g}'}(\boldsymbol{q},\omega)$ for a periodic surface (see equation (7.86)).

8.1. Generation-rate of electronic excitations

In the framework of TDDFT, an interacting many-electron system exposed to a frequency-dependent external potential $\phi^{\mathrm{ext}}(\boldsymbol{r},\omega)$ is replaced by a fictitious system of *noninteracting* electrons exposed to an effective self-consistent potential $\phi^{\mathrm{sc}}(\boldsymbol{r},\omega)$ of the form

$$\phi^{\mathrm{sc}}(\boldsymbol{r},\omega) = \phi^{\mathrm{ext}}(\boldsymbol{r},\omega) + \delta\phi(\boldsymbol{r},\omega), \tag{8.1}$$

where

$$\delta\phi(\boldsymbol{r},\omega) = \int \mathrm{d}\boldsymbol{r}' \left[v(\boldsymbol{r},\boldsymbol{r}') + f_{\mathrm{xc}}[n_0](\boldsymbol{r},\boldsymbol{r}';\omega)\right] \delta n(\boldsymbol{r}',\omega). \tag{8.2}$$

Hence, the rate at which a frequency-dependent external potential $\phi^{\mathrm{ext}}(\boldsymbol{r},\omega)$ generates electronic excitations in the many-electron system can be obtained, within lowest-order perturbation theory, as follows

$$w(\omega) = 2\pi \sum_{i,j} f_i(1-f_i) \left|\langle\psi_j(\boldsymbol{r})|\phi^{\mathrm{sc}}(\boldsymbol{r},\omega)\psi_i(\boldsymbol{r})\rangle\right|^2 \delta(\epsilon_i - \epsilon_f), \tag{8.3}$$

with $\psi_i(\boldsymbol{r})$ and ϵ_i being the eigenfunctions and eigenvalues of a 3D Kohn–Sham Hamiltonian. In terms of the induced electron density $\delta n(\boldsymbol{r},\omega)$ of equation (5.1), one finds [163]

$$w(\omega) = -2\,\mathrm{Im} \int \mathrm{d}\boldsymbol{r}\, \phi^*_{\mathrm{ext}}(\boldsymbol{r},\omega)\, \delta n(\boldsymbol{r},\omega), \tag{8.4}$$

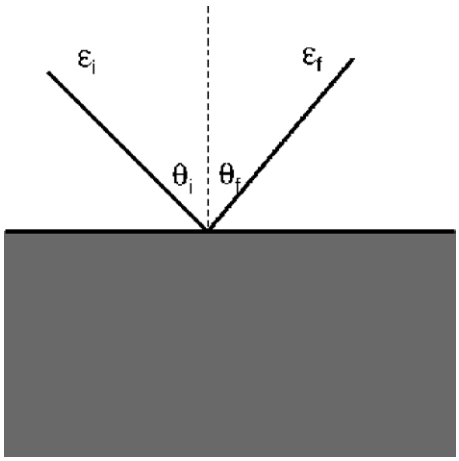

Figure 10. A schematic drawing of the scattering geometry in angle-resolved inelastic electron scattering experiments. On exciting a surface mode of frequency $\omega(q)$, the energy of detected electrons becomes $\varepsilon_f = \varepsilon_i - \omega(q)$, with the momentum q being determined by equation (8.9).

which in the case of a periodic surface takes the following form:

$$w(\omega) = \sum_{\boldsymbol{g}} \sum_{\boldsymbol{q}}^{\mathrm{SBZ}} w_{\boldsymbol{g}}(\boldsymbol{q}, \omega), \tag{8.5}$$

where $w_{\boldsymbol{g}}(\boldsymbol{q}, \omega)$ denotes the rate at which the external potential generates electronic excitations of frequency ω and parallel wave vector $\boldsymbol{q} + \boldsymbol{g}$:

$$w_{\boldsymbol{g}}(\boldsymbol{q}, \omega) = -\frac{2}{A} \operatorname{Im} \int \mathrm{d}z \, \phi_{\boldsymbol{g}}^{\mathrm{ext}}(z, \boldsymbol{q}) \, \delta n_{\boldsymbol{g}}(z, \boldsymbol{q}), \tag{8.6}$$

$\phi_{\boldsymbol{g}}^{\mathrm{ext}}(z, \boldsymbol{q})$ and $\delta n_{\boldsymbol{g}}(z, \boldsymbol{q})$ being the Fourier coefficients of the external potential and the induced electron density, respectively.

In particular, if the external potential is of the form of equation (7.88), the rate $w_{\boldsymbol{g}}(\boldsymbol{q}, \omega)$ can be expressed in terms of the surface-response function $g_{\boldsymbol{g},\boldsymbol{g}'}(\boldsymbol{q}, \omega)$ of equation (7.86), as follows

$$w_{\boldsymbol{g}}(\boldsymbol{q}, \omega) = \frac{4\pi}{qA} \operatorname{Im} g_{\boldsymbol{g},\boldsymbol{g}}(\boldsymbol{q}, \omega) \, \delta_{\boldsymbol{g},0}, \tag{8.7}$$

which for a jellium surface reduces to

$$w(q, \omega) = \frac{4\pi}{qA} \operatorname{Im} g(q, \omega), \tag{8.8}$$

with $g(q, \omega)$ being the surface-response function of equation (7.73). We note that although only the coefficient $\chi_{\boldsymbol{g}=0,\boldsymbol{g}'=0}(z, z'; \boldsymbol{q}, \omega)$ enters into the evaluation of the more realistic equation (8.7), the full $\chi^0_{\boldsymbol{g},\boldsymbol{g}'}(z, z'; \boldsymbol{q}, \omega)$ matrix is implicitly included through equation (7.83).

8.2. Inelastic electron scattering

The most commonly used experimental arrangement for the detection of surface collective excitations by the fields of moving charged particles is based on angle-resolved inelastic electron scattering [258]. Figure 10 shows a schematic drawing of the scattering geometry. A monochromatic beam of electrons of energy ε_i, incident on a flat surface at an angle θ_i, is

back scattered and detected by an angle-resolved energy analyzer positioned at an angle θ_f and energy ε_f. Inelastic events can occur, either before or after the elastic event, on exciting a surface mode of frequency $\omega(q) = \varepsilon_i - \varepsilon_f$. The energy and lifetime of this mode are determined by the corresponding energy-loss peak in the spectra, and the momentum q parallel to the surface is obtained from the measured angles θ_i and θ_f, as follows:

$$q = \sqrt{2}\left[\sqrt{\varepsilon_i}\,\sin\theta_i - \sqrt{\varepsilon_f}\,\sin\theta_f\right]. \tag{8.9}$$

The inelastic scattering cross section corresponding to a process in which an electronic excitation of energy ω and parallel wave vector $\boldsymbol{q}$ is created at a semi-infinite solid surface can be found to be proportional to the rate given by equation (8.7) [or equation (8.8) if the medium is represented by a jellium surface] and is, therefore, proportional to the imaginary part of the surface-response function, i.e. the so-called surface-loss function. Hence, apart from kinematic factors (which can indeed vary with energy and momentum [259, 260]), the inelastic scattering cross section is dictated by the rate $w_{\boldsymbol{g}}(\boldsymbol{q}, \omega)$ [or $w(q, \omega)$ if the medium is represented by a jellium surface] at which an external potential of the form of equation (7.88) generates electronic excitations of frequency ω and parallel wave vector $\boldsymbol{q}$.

In the following sections, we focus on the behaviour of the energy-loss function $\mathrm{Im}g_{\boldsymbol{g}=0,\boldsymbol{g}=0}(\boldsymbol{q}, \omega)$ [or $\mathrm{Im}g(q, \omega)$] and its maxima, which account for the presence and momentum-dispersion of surface collective excitations.

8.3. Surface plasmons: jellium surface

8.3.1. Simple models. In the simplest possible model of a jellium surface in vacuum, in which a semi-infinite medium with local dielectric function $\epsilon(\omega)$ at $z \leqslant 0$ is terminated at $z = 0$, the surface-response function $g(q, \omega)$ is obtained from equation (7.9) with $\epsilon_2 = 1$, or, equivalently, from equation (7.49) with $q = 0$, i.e.

$$g(q, \omega) = \frac{\epsilon(\omega) - 1}{\epsilon(\omega) + 1}, \tag{8.10}$$

which for a Drude dielectric function (see equation (2.15)) leads to the surface-loss function

$$\mathrm{Im}g(q, \omega) = \frac{\pi}{2}\,\omega_s\,\delta(\omega - \omega_s) \tag{8.11}$$

peaked at the surface-plasmon energy $\omega_s = \omega_p/\sqrt{2}$.

The *classical* energy-loss function of equation (8.10) represents indeed the true long-wavelength ($q \to 0$) limit of the actual self-consistent surface-loss function of a jellium surface. Nevertheless, the classical picture leading to equation (8.10) ignores both the nonlocality of the electronic response of the system and the microscopic spatial distribution of the electron density near the surface. Nonlocal effects can be incorporated within the hydrodynamic and specular-reflection models described in sections 7.2.1 and 7.2.2.

Within a one-step hydrodynamic approach, the surface-loss function is also dominated by a delta function (see equation (7.43)) but peaked at the momentum-dependent surface-plasmon energy of equation (7.40) (see also equation (3.30)):

$$\omega^2 = \frac{1}{2}\left[\omega_p^2 + \beta^2 q^2 + \beta q\sqrt{2\omega_p^2 + \beta^2 q^2}\right], \tag{8.12}$$

which at long wavelengths yields

$$\omega = \omega_p/\sqrt{2} + \beta q/2, \tag{8.13}$$

β representing the speed of propagation of hydrodynamic disturbances in the electron system[9].

In the SRM (with the bulk dielectric function being described within the RPA), surface plasmons, which occur at a momentum-dependent energy slightly different from its hydrodynamic counterpart, are damped by the presence of e–h pair excitations, as shown in figure 9[19].

The one-step hydrodynamic equations (8.12) and (8.13) and a numerical evaluation of the imaginary part of the SRM surface-response function of equation (7.49) (see figure 9) both yield a *positive* surface-plasmon energy dispersion at all wave vectors. Nonetheless, Bennett used a hydrodynamic model with a continuum decrease of the electron density at the metal surface, and found that a continuous electron-density variation yields a *monopole* surface plasmon with a *negative* dispersion at low wave vectors [84].

8.3.2. Self-consistent calculations: long wavelengths. Within a self-consistent long-wavelength description of the jellium-surface electronic response, Feibelman showed that up to first order in an expansion in powers of the magnitude q of the wave vector, the surface-response function of equation (7.73) can be written as [162]

$$g(q,\omega) = \frac{[\epsilon(\omega) - 1]\,[1 + q d_\perp(\omega)]}{\epsilon(\omega) + 1 - [\epsilon(\omega) - 1]\,q d_\perp(\omega)}, \tag{8.14}$$

where $\epsilon(\omega)$ represents the long-wavelength limit of the dielectric function of the bulk material [20] and $d_\perp(\omega)$ denotes the centroid of the induced electron density (see equation (3.13)) with respect to the jellium edge[21]. Equation (8.14) shows that at long wavelengths the poles of the surface-response function $g(q,\omega)$ are determined by the non-retarded surface-plasmon condition of equation (3.12) with $\epsilon_2 = 1$, which for a semi-infinite free-electron metal in vacuum yields the surface-plasmon dispersion relation of equation (3.15), i.e.

$$\omega = \omega_s\,(1 + \alpha\, q)\,, \tag{8.15}$$

with

$$\alpha = -\mathrm{Re}\,[d_\perp(\omega_s)]\,/2. \tag{8.16}$$

Equations (8.15)–(8.16) show that the long-wavelength surface-plasmon energy dispersion is dictated by the position of the centroid of the induced electron density with respect to the jellium edge. This can be understood by noting that the potential associated with the surface-plasmon charge attenuates on either side of $\mathrm{Re}[d_\perp(\omega_s)]$ with the attenuation constant q. If the fluctuating charge lies inside the jellium edge ($\mathrm{Re}[d_\perp(\omega_s)] < 0$), as q increases (thus the surface-plasmon potential attenuating faster) more of the field overlaps the metal giving rise to more interchange of energy between the electric field and the metal and resulting in a positive energy dispersion. However, if the fluctuating charge lies outside the jellium edge ($\mathrm{Re}[d_\perp(\omega_s)] > 0$), as q increases less of the metal is subject to the plasmon's electric field (i.e. there is a decreasing overlap of the fluctuating potential and the unperturbed electron density) which results in less interchange of energy between the electric field and the metal and a negative dispersion coefficient [261, 262].

Quantitative RPA calculations of the surface-plasmon linear-dispersion coefficient α entering equation (8.15) were carried out by several authors by using the specular-reflection and infinite-barrier models of the surface [82, 83, 88], a step potential [89, 90], and the more

[19] The quantity $\mathrm{Im}[-W(z,z;q,\omega)]$ represented in figure 9 (see equation (7.56)) coincides, apart from the factor $2\pi\,\exp(-2qz)/q$, with the energy-loss function $\mathrm{Im}\,g(q,\omega)$.

[20] For an ideal free-electron gas, $\epsilon(\omega)$ is given by the Drude dielectric function of equation (2.15).

[21] In general, the d-parameter $d_\perp(\omega)$ entering equation (8.14) should be replaced by $d_\perp(\omega) - d_\parallel(\omega)$. However, as for neutral jellium surfaces $d_\parallel(\omega)$ coincides with the jellium edge, $d_\perp(\omega) - d_\parallel(\omega)$ reduces to the centroid $d_\perp(\omega)$ of the induced electron density with respect to the jellium edge.

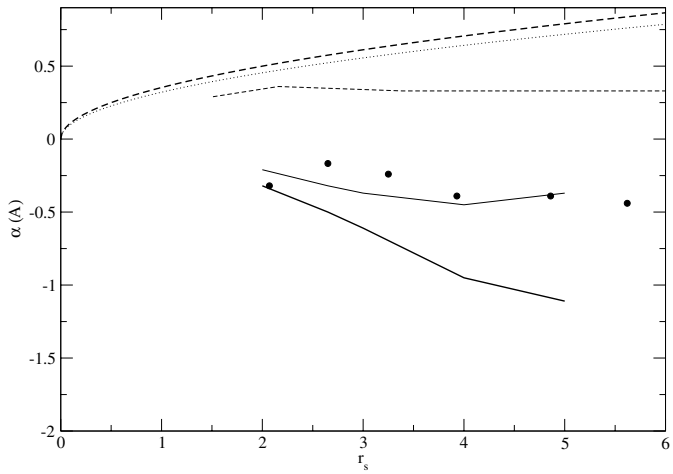

Figure 11. Long-wavelength surface-plasmon dispersion coefficient α entering equation (8.15), versus the electron-density parameter r_s, as obtained from equation (8.17) (dotted line) and from SRM (thick dashed line), IBM (thin dashed line), and self-consistent RPA and ALDA (thin and thick solid lines, respectively) calculations of the centroid of the induced electron density at $\omega = \omega_s$. The solid circles represent the angle-resolved low-energy inelastic electron scattering measurements reported in [98] for Na and K, in [100] for Cs, in [101] for Li and Mg, and in [264] for Al. The IBM and self-consistent (RPA and ALDA) calculations have been taken from [88] and [103], respectively.

realistic Lang–Kohn self-consistent surface potential [92, 103, 263]. Both Feibelman's RPA self-consistent calculations [92] and the ALDA calculations carried out later by Liebsch [103] and by Kempa and Schaich [263] demonstrated that in the range of typical bulk densities ($r_s = 2$–6) the centroid $d_\perp$ of the induced electron density at ω_s lies outside the jellium edge, which leads to a *negative* long-wavelength dispersion of the surface plasmon. These calculations, which corroborated Bennett's prediction [84], also demonstrated that the long-wavelength surface-plasmon dispersion is markedly sensitive to the shape of the barrier and to the presence of short-range XC effects.

Existing calculations of the long-wavelength dispersion coefficient α entering equation (3.15) are shown in figure 11 and summarized in table 1. At one extreme, the dotted line of figure 11 gives the single-step hydrodynamic coefficient $\alpha^{\rm HD}$ obtained from equation (3.31), i.e.

$$\alpha^{\rm HD} = \frac{\beta}{2\omega_s}, \tag{8.17}$$

with $\beta = \sqrt{3/5}(3\pi^2 n_0)^{1/3}$; within this model, the long-wavelength surface-plasmon dispersion is always positive. As in the single-step hydrodynamic approach, the SRM equilibrium density profile is of the form of equation (3.25), and in the IBM the electron density still varies too rapidly; as a result, the corresponding SRM and IBM α coefficients (represented by thick and thin dashed lines, respectively) are both positive. At the other extreme are the more realistic self-consistent RPA and ALDA calculations, represented by thin and thick solid lines, respectively, which yield a linear-dispersion coefficient α that is negative in the whole metallic density range.

Conclusive experimental confirmation that the original Bennett's prediction [84] was correct came with a series of measurements based on angle-resolved low-energy inelastic electron scattering [98–101, 264]. It has been demonstrated that the surface-plasmon energy of simple metals disperses downward in energy at small momentum q parallel to the surface, the

Table 1. Long-wavelength surface-plasmon dispersion coefficient α in Å for various simple metal surfaces, as obtained from equation (8.17) (HD) and from SRM, IBM, and self-consistent RPA and ALDA calculations of the centroid of the induced electron density at $\omega = \omega_s$ (see equation (8.16)), and from angle-resolved low-energy inelastic electron scattering measurements reported in [98] for Na and K, in [100] for Cs, in [101] for Li and Mg, and in [264] for Al. As in figure 11, the IBM and self-consistent (RPA and ALDA) calculations have been taken from [88] and [103], respectively. Also shown in this table are the measured values of the surface-plasmon energy ω_s at $q = 0$, which are all slightly below the jellium prediction: $\omega_p/\sqrt{2} = \sqrt{3/2r_s^3}e^2/a_0$, due to band-structure effects.

	r_s	ω_s	HD	SRM	IBM	RPA	ALDA	Exp.
Al	2.07	10.86	0.46	0.50	0.36	−0.21	−0.32	−0.32
Mg	2.66	7.38	0.52	0.57		−0.30	−0.50	−0.41
Li	3.25	4.28	0.58	0.63	0.33	−0.40	−0.70	−0.24
Na	3.93	3.99	0.64	0.70		−0.45	−0.85	−0.39
K	4.86	2.74	0.71	0.78		−0.35	−1.10	−0.39
Cs	5.62	1.99	0.76	0.84	0.33	−0.26	−1.14	−0.44

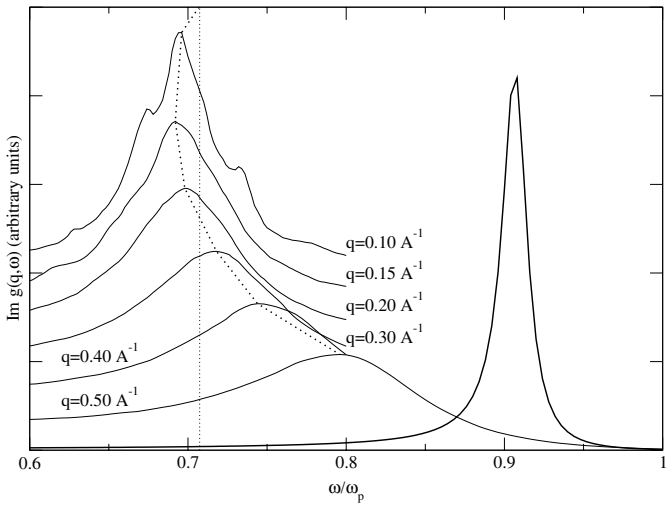

Figure 12. Self-consistent RPA calculations (thin solid lines) of the surface loss function $\mathrm{Im}g(q, \omega)$, as obtained from equation (7.73), versus the energy ω for a semi-infinite free-electron gas with the electron density equal to that of valence electrons in Al ($r_s = 2.07$) and for various magnitudes of the 2D wave vector $\boldsymbol{q}$. The thick solid line represents the SRM surface loss function for $r_s = 2.07$ and $q = 0.5\,\text{Å}^{-1}$.

dispersion coefficients (represented in figure 11 by solid circles) being in reasonable agreement with self-consistent jellium calculations, as shown in figure 11 and table 1.

8.3.3. Self-consistent calculations: arbitrary wavelengths. At arbitrary wavelengths, surface-plasmon energies can be derived from the maxima of the surface loss function $\mathrm{Im}g(q, \omega)$ and compared with the peak positions observed in experimental electron energy-loss spectra. Figure 12 shows the self-consistent calculations of $\mathrm{Im}g(q, \omega)$ that we have obtained in the RPA for a semi-infinite free-electron gas (jellium surface) with the electron density equal to that of valence electrons in Al ($r_s = 2.07$). For 2D wave vectors of magnitude in the range $q = 0 - 0.5\,\text{Å}^{-1}$, all spectra are clearly dominated by a surface-plasmon excitation, which is seen to first shift to lower frequencies as q increases [as dictated by equations (8.15)–(8.16)]

and then, from about $q = 0.15\,\text{Å}^{-1}$ on, towards higher frequencies.

For the numerical evaluation of the spectra shown in figure 12 we have first computed the interacting density-response function $\chi(z, z'; q, \omega)$ of a sufficiently thick jellium slab by following the method described in [265], and we have then derived the surface-loss function from equation (7.73). Alternatively, the self-consistent energy-loss spectra reported in [100] (see also [163]) were obtained by first computing the noninteracting density-response function $\chi^0(z, z'; q, \omega)$ of a semi-infinite electron system in terms of Green's functions, then performing a matrix inversion of equation (7.76) with the external potential $\phi^{\text{ext}}(z; q, \omega)$ of equation (7.75), and finally deriving the surface-loss function from equation (7.74). As expected, both approaches yield the same results.

Figure 13 shows the calculated and measured dispersion of surface plasmons in Al, Mg, Li, Na, K, and Cs. The jellium calculations presented here do not include effects due to band-structure effects; thus, all frequencies have been normalized to the measured value ω_s of the $q = 0$ surface-plasmon energy (see table 1). This figure shows that the single-step HD and SRM surface-plasmon dispersions (thin and thick dashed lines, respectively) are always upward and nearly linear. However, self-consistent RPA and ALDA calculations (thin and thick solid lines, respectively), which are based on a self-consistent treatment of the surface density profile, show that the surface-plasmon dispersion is initially downward (as also shown in figure 11 and table 1), then flattens out, and rises thereafter, in agreement with experiment (solid circles). A comparison between self-consistent RPA and ALDA calculations shows that although there is no qualitative difference between them XC effects tend to reduce the surface-plasmon energy, thereby improving the agreement with the measured plasmon frequencies. This lowering of the surface-plasmon energies shows that dynamic XC effects combine to lower the energy of the electron system, which is due to the weakening of the Coulomb e–e interaction by these effects.

Recently, XC effects on the surface-plasmon dispersion of Mg and Al were introduced still in the framework of TDDFT (but beyond the ALDA) by using the nonlocal (momentum-dependent) static XC local-field factor of equation (5.24) [118, 119]. At low wave vectors, this calculation (thick solid line with open circles) nearly coincides with the ALDA calculation (thick solid line), as expected. At larger wave vectors, however, the *nonlocal* calculation begins to deviate from the ALDA, bringing the surface-plasmon dispersion to nearly perfect agreement with the data for all values of the 2D wave vector. *Ab initio* calculations of the surface-plasmon dispersion of real Al and Mg were also reported in [118, 119]. For plasmon frequencies that are normalized to the measured value ω_s at $q = 0$ (as in figure 13), *ab initio* and jellium calculations are found to be nearly indistinguishable; however, only the *ab initio* calculations account for an overall lowering of the surface-plasmon dispersion that is due to core polarization.

In the case of the alkali metals Li, Na, K and Cs, there is a mismatch in the linear (low q) region of the surface-plasmon dispersion curve between jellium ALDA calculations and the experiment. The theoretical challenges for the future are therefore to understand the impact of band-structure and many-body effects on the energy of surface plasmons in these materials, which will require to pursue complete first-principles calculations of the surface electronic response at the level of those reported in [118, 119] for Mg and Al, respectively.

Thin films of jellium have been considered recently, in order to investigate the influence of the slab thickness on the excitation spectra and the surface-plasmon energy dispersion [266]. Oscillatory structures were found, corresponding to electronic interband transitions, and it was concluded that in the case of a slab thickness larger than $\sim$100 a.u. surface plasmons behave like the surface plasmon of a semi-infinite system.

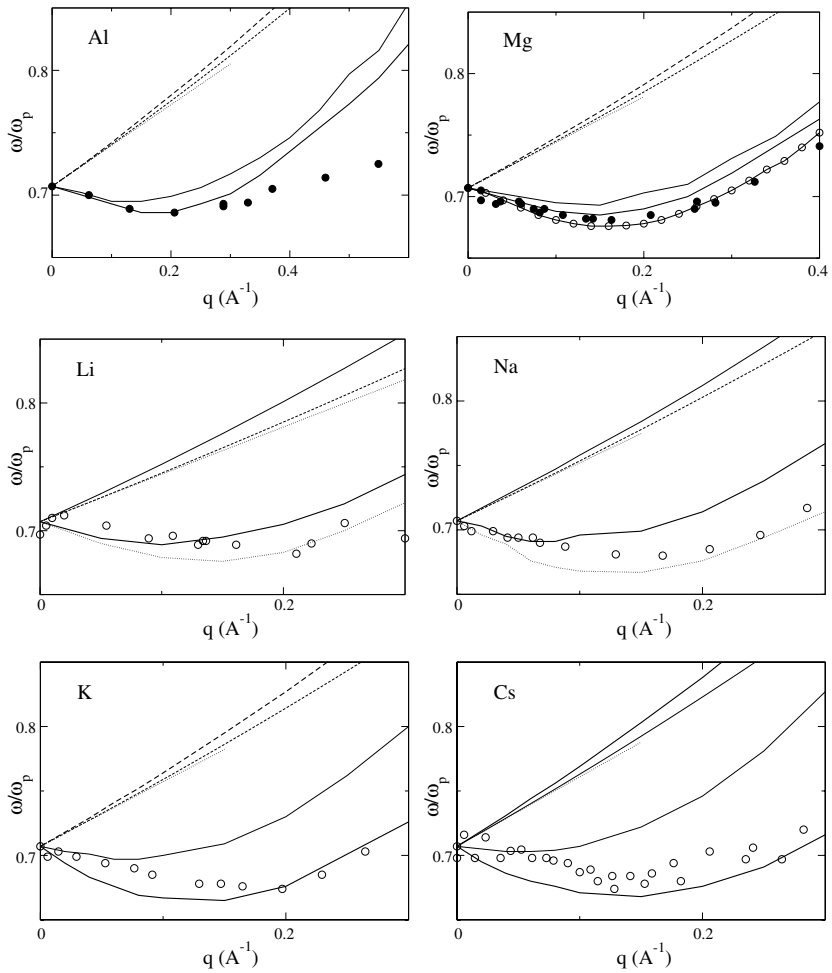

Figure 13. Surface-plasmon energy dispersion for the simple metals Al, Mg, Li, Na, K, and Cs, as obtained from equation (8.12) (thin dashed lines) and from SRM (thick dashed lines) and self-consistent RPA (thin solid lines) and ALDA (thick solid lines) calculations of the surface loss function $\mathrm{Im}g(q,\omega)$, and from the peak positions observed in experimental electron energy-loss spectra (solid circles). The dotted lines represent the initial slope of the HD surface-plasmon energy dispersion, as obtained from equation (3.31). In the case of Mg, the thick solid line with open circles represents the jellium TDDFT calculations reported in [118] and obtained with the use of the nonlocal (momentum-dependent) static XC local-field factor of equation (5.24). All frequencies have been normalized to the measured value ω_s of the $q = 0$ surface-plasmon energy.

8.3.4. Surface-plasmon linewidth. At jellium surfaces, the actual self-consistent surface response function $\mathrm{Im}g(q,\omega)$ reduces in the long-wavelength ($q \to 0$) limit to equation (8.11), so that long-wavelength surface plasmons are expected to be infinitely long-lived excitations. At finite wave vectors, however, surface plasmons are damped (even at a jellium surface) by the presence of e–h pair excitations [267].

Figure 14 shows the results that we have obtained from SRM (dashed lines) and self-consistent (solid lines) RPA calculations of the full width at half maximum (FWHM), $\Delta\omega$, of the surface loss function $\mathrm{Im}g(q,\omega)$. Also shown in this figure are the corresponding linewidths that have been reported in [98, 100, 101, 264] from experimental electron energy-loss spectra

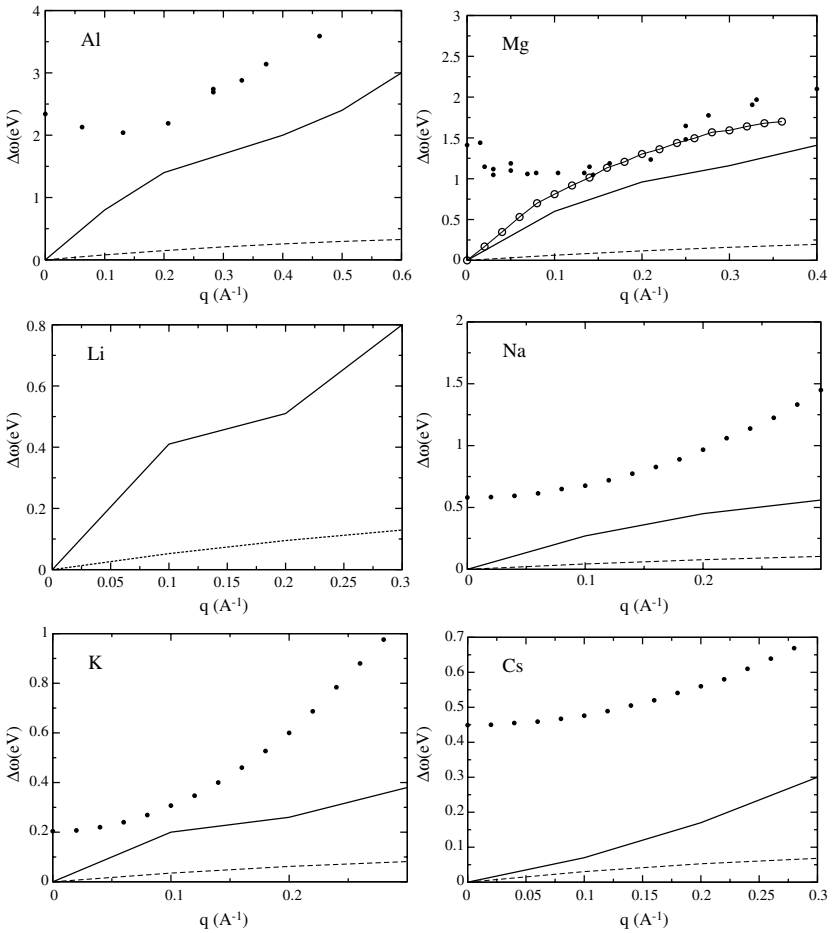

Figure 14. Surface-plasmon full width at half maximum (FWHM), $\Delta\omega$, for the simple metals Al, Mg, Li, Na, K, and Cs, as obtained from SRM (thick dashed lines) and self-consistent RPA (thin solid lines) calculations of the surface loss function $\mathrm{Im}g(q,\omega)$, and from the experimental electron energy-loss spectra at different scattering angles (solid circles) reported in [98] for Na and K, in [100] for Cs, in [101] for Li and Mg, and in [264] for Al. In the case of Mg, the thick solid line with open circles represents the jellium TDDFT calculations reported in [118] and obtained with the use of the nonlocal (momentum-dependent) static XC local-field factor of equation (5.24).

at different scattering angles. This figure clearly shows that at real surfaces the surface-plasmon peak is considerably wider than predicted by self-consistent RPA jellium calculations, especially at low wave vectors. This additional broadening should be expected to be mainly caused by the presence of short-range many-body XC effects and interband transitions, but also by scattering from defects and phonons.

Many-body XC effects on the surface-plasmon linewidth of Mg and Al were incorporated in [118,119] in the framework of TDDFT with the use of the nonlocal (momentum-dependent) static XC local-field factor of equation (5.24). These TDDFT calculations have been plotted in figure 14 by solid lines with circles; a comparison of these results with the corresponding RPA calculations (solid lines without circles) shows that short-range XC effects tend to increase the finite-q surface-plasmon linewidth, bringing the jellium calculations into nice agreement

Table 2. Relative widths $\Delta\omega/\omega_s$ of surface plasmons, as derived from the imaginary part of the surface-response function of equation (8.10) with measured values of the bulk dielectric function $\epsilon(\omega)$ (theory) [163] and from the surface-loss measurements at $q = 0$ reported in [98,100,101,264] (experiment).

	Al	Mg	Li	Na	K	Cs	Ag	Hg
Theory	0.035	0.16	0.33		0.035		0.027	0.18
Experiment	0.22	0.19	0.35		0.07		0.027	0.16

with experiment at the largest values of q. Nevertheless, jellium calculations cannot possibly account for the measured surface-plasmon linewidth at small q, which deviates from zero even at $q = 0$.

In the long-wavelength ($q \to 0$) limit, surface plasmons are known to be dictated by bulk properties through a long-wavelength bulk dielectric function $\epsilon(\omega)$, as in equation (8.10). Hence, the experimental surface-plasmon widths $\Delta\omega$ at $q = 0$ should be approximately described by using in equation (8.10) the measured bulk dielectric function $\epsilon(\omega)$. Table 2 exhibits the relative widths $\Delta\omega/\omega_s$ derived in this way [163], together with available surface-loss measurements at $q = 0$. Since silver (Ag) and mercury (Hg) have partially occupied d-bands, a jellium model, like the one leading to equation (8.10), is not, in principle, appropriate to describe these surfaces. However, table 2 shows that the surface-plasmon width of these solid surfaces is very well described by introducing the measured bulk dielectric function (which includes band-structure effects due to the presence of d-electrons) into equation (8.10). Nevertheless, the surface-plasmon widths of simple metals like K and Al, with no d-electrons, are considerably larger than predicted in this simple way[22]. This shows that an understanding of surface-plasmon broadening mechanisms requires a careful analysis of the actual band structure of the solid.

Approximate treatments of the impact of the band structure on the surface-plasmon energy dispersion have been developed by several authors, but a first-principles description of the surface-plasmon energy dispersion and linewidth has been reported only in the case of the simple-metal prototype surfaces Mg(0001) [118] and Al(111) [119]; these calculations will be discussed in section 8.4.3.

8.3.5. Multipole surface plasmons. In his attempt to incorporate the smoothly decreasing electron density profile at the surface, Bennett [84] solved the equations of a simple hydrodynamic model with a density profile which decreases linearly through the surface region and found that in addition to Ritchie's surface plasmon at $\omega \sim \omega_s$, with a negative energy dispersion at low $\boldsymbol{q}$ wave vectors, there is an upper surface plasmon at higher energies. This is the so-called multipole surface plasmon, which shows a positive wave vector dispersion even at small $\boldsymbol{q}$.

The possible existence and properties of multipole surface plasmons was later investigated in the framework of hydrodynamical models for various choices of the electron-density profile at the surface [269–271]. According to these calculations, higher multipole excitations could indeed exist, for a sufficiently diffuse surface, in addition to the usual surface plasmon at $\omega \sim \omega_s$. However, approximate quantum-mechanical RPA calculations gave no evidence for the existence of multipole surface plasmons [9,89], thereby leading to the speculation that multipole surface plasmons might be an artifact of the hydrodynamic approximation [271,272].

[22] Beck and Dasgupta [268] reported a two-band model calculation of the surface-plasmon linewidth of Al, but they found $\Delta\omega/\omega_s \approx 0.07$ which is also too small.

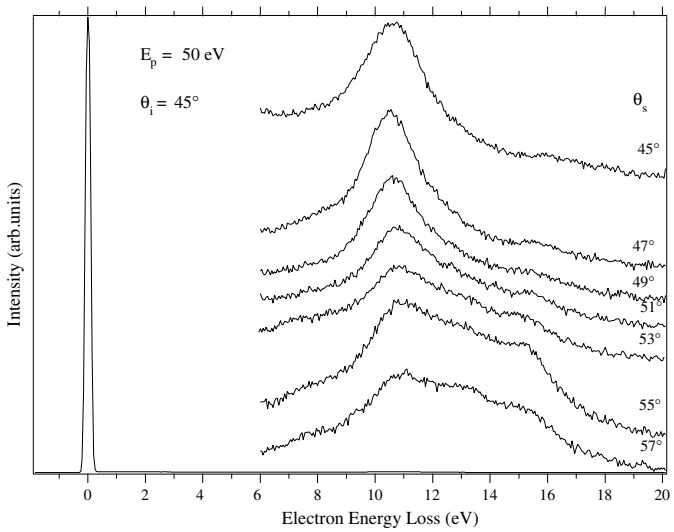

Figure 15. Angle-resolved high-resolution electron energy-loss spectra of the Al(111) surface at various scattering angles θ_s. The primary beam energy is 50 eV and the incident angle is $\theta_i = 45^\circ$ (from [264], used with permission).

The first experimental sign for the existence of multipole surface modes was established by Schwartz and Schaich [273] in their theoretical analysis of the photoemission yield spectra that had been reported by Levinson *et al* [122]. Later on, Dobson and Harris [274] used a DFT scheme to describe realistically the electron-density response at a jellium surface, to conclude that multipole surface plasmons should be expected to exist even for a high-density metal such as Al (which presents a considerably abrupt electron density profile at the surface). Two years later, direct experimental evidence of the existence of multipole surface plasmons was presented in inelastic reflection electron scattering experiments on smooth films of the low-density metals Na, K and Cs [99], the intensity of these multipole surface plasmons being in agreement with the DFT calculations reported later by Nazarov and Nishigaki [275]. The Al multipole surface plasmon has been detected only recently by means of angle-resolved high-resolution electron-energy-loss spectroscopy (HREELS) [264].

Figure 15 shows the loss spectra of the Al(111) surface, as obtained by Chiarello *et al* [264] with an incident electron energy of 50 eV and an incident angle of 45° with respect to the surface normal. The loss spectrum obtained in the specular geometry ($\theta_s = 45^\circ$) is characterized mainly by a single peak at the conventional surface-plasmon energy $\omega_s = 10.55$ eV. For off-specular scattering angles ($\theta_s \neq 45^\circ$), the conventional surface plasmon exhibits a clear energy dispersion and two other features arise in the loss spectra: the multipole surface plasmon and the bulk plasmon. The loss spectrum obtained at $\theta_s = 53^\circ$, which corresponds to $q = 0$ (see equation (8.9)) is represented again in figure 16, but now together with the background substraction and Gaussian-fitting procedure reported in [264]. The peak at $\omega_p = 15.34$ corresponds to the excitation of the Al bulk plasmon, and the multipole surface plasmon is located at 13.20 eV.

The calculated and measured energies and linewidths of long-wavelength ($q \to 0$) multipole surface plasmons in simple metals are given in table 3. On the whole, the ratio ω_m/ω_p agrees with ALDA calculations. Good agreement between ALDA calculations and experiment is also obtained for the entire dispersion of multipole surface plasmons, which is

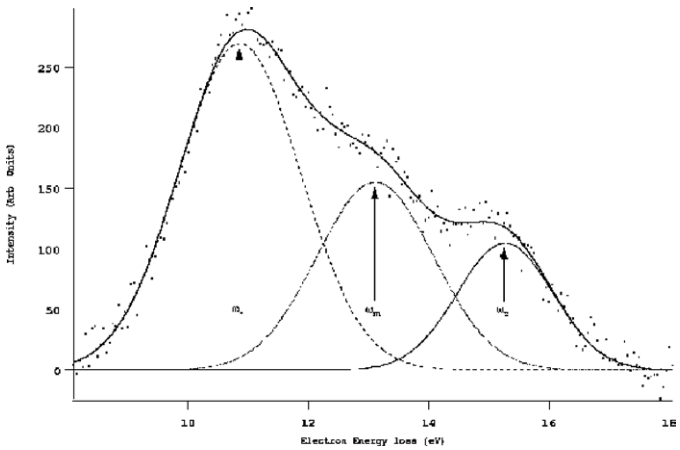

Figure 16. Angle-resolved high-resolution electron energy-loss spectra of the Al(111) surface at $\theta_s = 53^\circ$, for $\theta_i = 45^\circ$ and $\varepsilon_i = 50$ eV (as in figure 15) but now together with the deconvolution into contributions corresponding to the excitation of the conventional surface plasmon at $\omega_s = 10.55$ eV, multipole surface plasmon at 13.20 eV, and bulk plasmon at $\omega_p = 15.34$ eV (from [264], used with permission).

Table 3. Angle-resolved low-energy inelastic electron scattering measurements of the energy ω_m and width $\Delta\omega$ of multipole surface plasmons at $q = 0$, as reported in [99] for Na and K, in [100] for Cs, in [101] for Li and Mg, and in [264] for Al. Also shown is the ratio ω_m/ω_p calculated in the RPA and ALDA and reported in [100].

	r_s	ω_m (eV)	ω_m/ω_p	RPA	ALDA	$\Delta\omega$ (eV)	$\Delta\omega/\omega_p$
Al	2.07	13.20	0.86	0.821	0.782	2.1	0.14
Mg	2.66			0.825	0.784		
Li	3.25			0.833	0.789		
Na	3.93	4.67	0.81	0.849	0.798	1.23	0.21
K	4.86	3.20	0.84	0.883	0.814	0.68	0.18
Cs	5.62	2.40	0.83	0.914	0.837	0.64	0.22

found to be approximately linear and positive. This positive dispersion is originated in the fact that the centroid of the induced electron density, which at $\omega \sim \omega_s$ is located outside the jellium edge, is shifted into the metal at the multipole resonance frequency ω_m. We also note that multipole surface plasmons have only been observed at wave vectors well below the cutoff value for Landau damping, which has been argued to be due to an interplay between Coulomb and kinetic energies [276].

In a semi-infinite metal consisting of an abrupt step of the unperturbed electron density at the surface (as in the hydrodynamic and specular-reflection models described above), surface plasmons would be localized at the surface and would propagate like plane waves, as shown in figure 3, with positive and negative surface charge regions alternating periodically. In the real situation in which the electron density decays smoothly at the surface, surface plasmons also propagate along the surface as illustrated in figure 3, but the finite width of the electron-density profile yields fluctuating densities with finite widths, as illustrated in figure 17 for a model surface electron density profile with linear decay over a finite region.

Figure 17 qualitatively represents the real situation in which apart from small Friedel oscillations the distribution of the conventional surface plasmon at ω_s consists in the direction normal to the surface of a single peak (i.e. it has a *monopole* character), while the charge

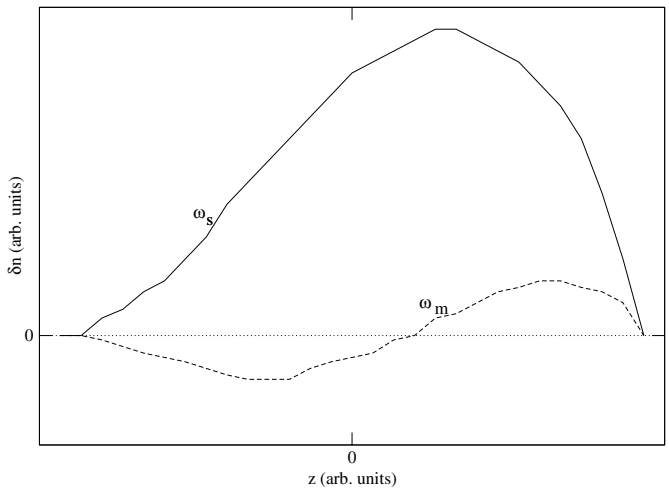

Figure 17. Real part of the electron density induced at $\omega = \omega_s$ (solid line) and $\omega = \omega_m$ (dashed line), as reported in [163] for a model unperturbed electron density profile with linear decay over a finite region.

distribution of the upper mode at ω_m has decreasing oscillating amplitude towards the interior of the metal, i.e. it has a *multipole* character. Along the direction normal to the surface, the electronic density associated with this multipole surface plasmon integrates to zero.

In the retarded region, where $q < \omega_s/c$, the surface-plasmon dispersion curve deviates from the non-retarded limit (where $q \gg \omega_s/c$) and approaches the light line $\omega = cq$, as shown by the lower solid line of figure 2, thus going to zero at $q = 0$; hence, in a light experiment the external radiation dispersion line will never intersect the surface-plasmon line, i.e. in an ideal flat surface the conventional *monopole* surface plasmon cannot be excited in a photoyield experiment. However, the multipole surface plasmon dispersion curve crosses the light line at $q \sim \omega_m/c$ and goes to ω_m at $q = 0$. Consequently, angle- and energy-resolved photoyield experiments are suitable to identify the multipole surface plasmon. A large increase in the surface photoyield was observed from K and Rb at $\omega_m = 3.15\,\text{eV}$ and 2.84 eV, respectively [277], from Al(100) at $\omega_m = 12.5\,\text{eV}$ [122], and from Al(111) at $\omega_m = 13\,\text{eV}$ [123], in nice agreement with the multipole-plasmon energy observed with the HREELS technique by Chiarello *et al* [264]. HREELS measurements yield, however, a FWHM of 2.1 eV for the $q = 0$ multipole surface plasmon in Al(111) [264], which is considerably smaller than the FWHM of 3 eV measured by photoyield experiments [123].

8.4. Surface plasmons: real surfaces

8.4.1. Stabilized jellium model. A simple way of including approximately the lattice potential that is absent in the jellium model is the so-called stabilized jellium or structureless pseudopotential model [278, 279], which yields energy stability against changes in the background density.

In this model, a solid surface is assumed to be translationally invariant in the plane of the surface, as in the jellium model. Hence, single-particle wave functions can be separated as in equation (7.62) into a plane wave along the surface and a component $\psi_i(z)$ describing motion normal to the surface. In the framework of DFT and TDDFT, this component is obtained by solving self-consistently a Kohn–Sham equation of the form of equation (7.65) but with the

Table 4. Measured values of the surface-plasmon energy ω_s at $q = 0$ and the long-wavelength surface-plasmon dispersion coefficient α of equation (8.16) for the noble metal Ag and the transition metals Hg and Pd. Also shown in this table is the coefficient α obtained from RPA and ALDA calculations of the centroid of the electron density induced at $\omega = \omega_s$ (see equation (8.16)) in a homogeneous electron gas with the electron density equal to that of valence sp electrons in Ag and Hg. Note that the measured values of the surface-plasmon energy ω_s at $q = 0$ are considerably below the jellium prediction: $\omega_p/\sqrt{2} = \sqrt{3/2r_s^3}e^2/a_0$, mainly due to the presence of d electrons. ω_s and α are given in eV and Å, respectively.

	r_s	ω_s	Direction	α^{exp}	α^{RPA}	α^{ALDA}
Ag(100)	3.02	3.7		0.377	−0.370	−0.609
Ag(111)	3.02	3.7		0.162	−0.370	−0.609
Ag(110)	3.02	3.7	⟨100⟩	0.305	−0.370	−0.609
			⟨1$\bar{1}$0⟩	0.114	−0.370	−0.609
Hg	2.65	6.9		−0.167	−0.32	−0.50
Pd		7.4		−1.02		

effective Kohn–Sham potential of equation (7.66) being replaced by

$$v_{KS}[n_0](z) = v_H[n_0](z) + v_{xc}[n_0](z) + \langle \delta v \rangle_{WS}, \tag{8.18}$$

$\langle \delta v \rangle_{WS}$ representing the difference between a local pseudopotential and the jellium potential:

$$\langle \delta v \rangle_{WS} = \frac{3r_c^2}{2r_s^3} - \frac{3Z^{2/3}}{10r_s}, \tag{8.19}$$

where Z is the chemical valence of the solid and r_c is a core radius that is chosen to stabilize the metal for given values of the parameters r_s and Z.

The stabilized jellium model was used by Ishida and Liebsch [280] to carry out RPA and ALDA calculations of the dispersion of the energy and linewidth of surface plasmons in Mg and Li. It is well known that the stabilized jellium model gives considerably better work functions and surface energies than the standard jellium model; however, the impact of a structureless pseudopotential on the properties of surface plasmons is found to be very small. In particular, this simple pseudopotential cannot explain the presence of core polarization lowering the surface-plasmon frequency for all wave vectors and does not account for the fact that the measured q dependence of the Li surface-plasmon energy is very much flatter than calculated within the jellium model (see figure 13). This discrepancy (not present in the case of Al and Mg) is attributed to the presence of an interband transition in Li at 3.2 eV, which is only slightly below the measured surface-plasmon energy at $q = 0$ ($\omega_s = 4.28$ eV) and allows, therefore, for interference between bulk single-particle and surface collective modes, as discussed in [280].

8.4.2. Occupied d-bands: simple models. Significant deviations from the dispersion of surface plasmons at jellium surfaces occur on the noble metal Ag [104–107], and the transition metals Hg [108] and Pd [281] (see table 4). These deviations are mainly due to the presence in these metals of filled 4d and 5d bands, which in the case of Ag yields an anomalous positive and strongly crystal-face dependent dispersion.

Ag. In order to describe the observed features of Ag surface plasmons, Liebsch [111] considered a self-consistent jellium model for valence 5s electrons and accounted for the presence of occupied 4d bands via a polarizable background of d electrons characterized by a local dielectric function $\epsilon_d(\omega)$ that can be taken from bulk optical data (see figure 18) [282].

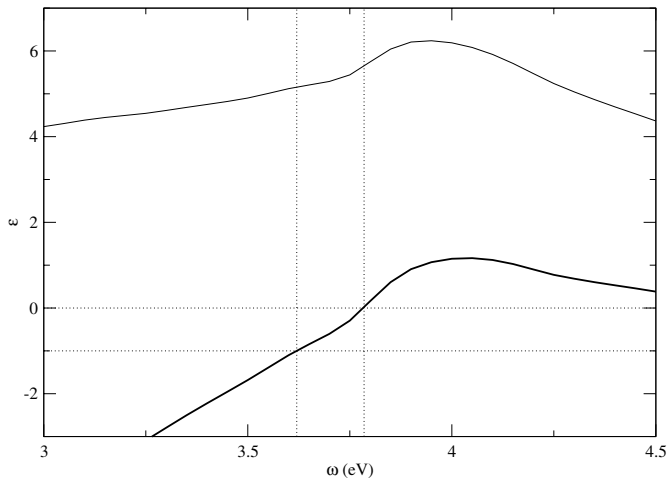

Figure 18. The thin solid line represents the real part of the d band contribution $\epsilon_{\rm d}(\omega)$ to the measured optical dielectric function of Ag [282]. The thick solid line represents $\epsilon(q,\omega)+\epsilon_{\rm d}(\omega)-1$ at $q=0$, i.e. $\epsilon_{\rm d}(\omega)-\omega_{\rm p}^2/\omega^2$. The vertical dotted lines represent the energies at which the plasmon conditions of equations (8.22) and (8.29) are fulfilled: $\omega_{\rm p}'=3.78\,{\rm eV}$ and $\omega_{\rm s}'=3.62\,{\rm eV}$, respectively. At these frequencies: $\epsilon_{\rm d}(\omega_{\rm p}')=5.65$ and $\epsilon_{\rm d}(\omega_{\rm p})=5.15$.

For a homogeneous electron gas, one simply replaces in this model the bare Coulomb interaction $v(\boldsymbol{r},\boldsymbol{r}')$ by

$$v'(\boldsymbol{r},\boldsymbol{r}';\omega)=v(\boldsymbol{r},\boldsymbol{r}')\,\epsilon_{\rm d}^{-1}(\omega), \tag{8.20}$$

which due to translational invariance yields the following expression for the Fourier transform $W'(q,\omega)$ of the screened interaction $W'(\boldsymbol{r},\boldsymbol{r}';\omega)$ of the form of equation (7.3):

$$W'(q,\omega)=\frac{v(q)}{\epsilon(q,\omega)+\epsilon_{\rm d}(\omega)-1}, \tag{8.21}$$

with $\epsilon(q,\omega)$ being the dielectric function of a homogeneous system of sp valence electrons (5s electrons in the case of Ag). Hence, the screened interaction $W'(q,\omega)$ has poles at the bulk-plasmon condition

$$\epsilon(q,\omega)+\epsilon_{\rm d}(\omega)-1=0, \tag{8.22}$$

which in the case of Ag ($r_{\rm s}=2.02$) and in the absence of d electrons ($\epsilon_{\rm d}=1$) yields the long-wavelength ($q\to 0$) bulk plasmon energy $\omega_{\rm p}=8.98\,{\rm eV}$. Instead, if d electrons are characterized by the frequency-dependent dielectric function $\epsilon_{\rm d}(\omega)$ represented by a thin solid line in figure 18, equation (8.22) yields the observed long-wavelength bulk plasmon at

$$\omega_{\rm p}'=\frac{\omega_{\rm p}}{\sqrt{\epsilon_{\rm d}(\omega_{\rm p}')}}=3.78\,{\rm eV}. \tag{8.23}$$

In the case of a solid surface, one still uses a modified (d-screened) Coulomb interaction $v'(\boldsymbol{r},\boldsymbol{r}';\omega)$ of the form of equation (8.20), but with $\epsilon_{\rm d}(\omega)$ being replaced by

$$\epsilon_{\rm d}(z,\omega)=\begin{cases}\epsilon_{\rm d}(\omega), & z\leqslant z_{\rm d}\\ \\ 1, & z>z_{\rm d},\end{cases} \tag{8.24}$$

which represents a polarizable background of d electrons that extends up to a certain plane at $z = z_d$. Using equation (8.24), the 2D Fourier transform of $v'(\boldsymbol{r}, \boldsymbol{r}'; \omega)$ yields [283]:

$$v'(z, z'; \boldsymbol{q}_\parallel, \omega) = \frac{2\pi}{q_\parallel \epsilon_d(z', \omega)} [e^{-q_\parallel |z-z'|} + \mathrm{sgn}(z_d - z')\sigma_d(\omega)\, e^{-q_\parallel |z-z_d|} e^{-q_\parallel |z_d - z'|}], \tag{8.25}$$

where

$$\sigma_d = [\epsilon_d(\omega) - 1]/[\epsilon_d(\omega) + 1]. \tag{8.26}$$

Introduction of equations (8.25) and (8.26) into an equation of the form of equation (7.59) yields the following expression for the modified RPA surface-response function:

$$g'(q, \omega) = \int dz\, e^{qz} \frac{\delta n(z; q, \omega)}{\epsilon_d(z, \omega)} + a(q, \omega), \tag{8.27}$$

where $\delta n(z; q, \omega)$ represents the RPA induced density of sp valence electrons which is given by equation (7.76) with $f_{xc}[n_0](z, z'; q, \omega) = 0$, and

$$a(q, \omega) = \sigma_d(\omega)\left[e^{q z_d} + \int dz e^{-q|z_d - z|} \mathrm{sgn}(z_d - z) \frac{\delta n(z; q, \omega)}{\epsilon_d(z, \omega)}\right]. \tag{8.28}$$

In the long-wavelength ($q \to 0$) limit, equation (8.27) takes the form of equation (8.10) but with $\epsilon(\omega)$ replaced by $\epsilon(\omega) + \epsilon_d(\omega) - 1$, which leads to the surface-plasmon condition:

$$\epsilon(\omega) + \epsilon_d(\omega) = 0. \tag{8.29}$$

For a Drude dielectric function $\epsilon(\omega)$ with $\omega_p = 8.98\,\mathrm{eV}$ ($r_s = 3.02$) and in the absence of d electrons ($\epsilon_d = 1$), the surface-plasmon condition of equation (8.29) yields the surface-plasmon energy $\omega_s = 6.35\,\mathrm{eV}$. However, in the presence of d electrons characterized by the frequency-dependent dielectric function $\epsilon_d(\omega)$, equation (8.29) leads to a modified (d-screened) surface plasmon at

$$\omega_s' = \frac{\omega_p}{\sqrt{1 + \epsilon_d(\omega_s')}} = 3.62\,\mathrm{eV}, \tag{8.30}$$

which for $\omega_p = 8.98\,\mathrm{eV}$ and the dielectric function $\epsilon_d(\omega)$ represented by a thin solid line in figure 18 yields $\omega_s' = 3.62\,\mathrm{eV}$, only slightly below the energy 3.7 eV of the measured Ag surface plasmon [106].

At finite wavelengths, the surface-plasmon dispersion was derived by Liebsch from the peak positions of the imaginary part of the surface-response function of equation (8.27), as obtained with a self-consistent RPA calculation of the induced density $\delta n(z; q, \omega)$ of $5s^1$ valence electrons. The surface-plasmon dispersion was found to be positive for $z_d \leqslant 0$ and to best reproduce the observed linear dispersion of Ag surface plasmons for $z_d = -0.8\,\text{Å}$. Hence, one finds that (i) the s–d screened interaction is responsible for the lowering of the surface-plasmon energy at $q = 0$ from the free-electron value of 6.35 eV to 3.62 eV, and (ii) the observed blueshift of the surface-plasmon frequency at increasing q can be interpreted as a reduction of the s–d screened interaction in the 'selvedge' region that is due to a decreasing penetration depth of the induced electric field.

With the aim of describing the strongly crystal-face dependence of the surface-plasmon energy dispersion in Ag, Feibelman [110] thought of the Ag surface plasmon as a collective mode that is split off the bottom of the 4d-to-5s electron–hole excitation band, and considered the relation between the surface-plasmon dispersion and the 4d-to-5s excitations induced by the surface-plasmon's field. He calculated the s–d matrix elements using a one-dimensional surface perturbation of the jellium Lang–Kohn potential, and he argued that for Ag(100) the

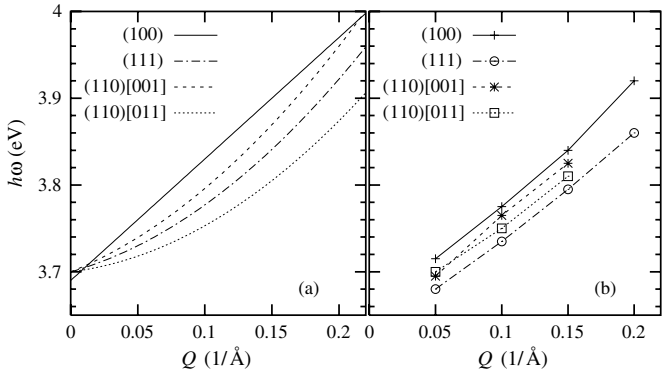

Figure 19. Surface-plasmon energy dispersion for the low-index faces (100), (111), and (110) of Ag. In the case of Ag (110), the exhibited surface-plasmon energy dispersions correspond to wave vectors along the [001] and [110] directions. (*a*) Experimental data from [106]. (*b*) The results obtained within the jellium–dipolium model (from [114], used with permission).

dispersion coefficient is increased relative to Ag(111) because in the case of Ag(100) the 4d electrons lie closer to the centroid of the oscillating free-electron charge, and the probability of 4d-to-5s excitation is, therefore, enhanced.

Most recently, a self-consistent jellium model for valence 5s electrons in Ag was combined with a so-called dipolium model in which the occupied 4d bands are represented in terms of polarizable spheres located at the sites of a semi-infinite fcc lattice [114] to calculate electron energy-loss spectra for all three low-index faces of Ag. The surface-plasmon energy dispersions obtained from these spectra are exhibited in figure 19 together with the experimental measurements [106]. This figure shows that the trend obtained for the different crystal orientations is in qualitative agreement with the data. On the one hand, the surface-plasmon dispersion of Ag(100) lies above that of the (111) surface; on the other hand, the slope for Ag(110) is larger for wave vectors along the [001] direction than when the wave vector is taken to have the [110] direction, illustrating the effect of the interplanar geometry on the effective local fields. The observed overall variation of the measured positive slope with crystal orientation is, however, considerably larger than predicted by the jellium–dipolium model. This must be a signature of genuine band structure effects not captured in the present model, which calls for a first-principles *ab initio* description of the electronic response of real Ag surfaces.

The impact of the band structure on the surface-plasmon energy dispersion in Ag was addressed by Moresco *et al* [284] and by Savio *et al* [285]. These authors performed test experiments with the K/Ag(110) and O/Ag(001) systems and concluded that (i) the surface-plasmon dispersion can be modified at will by manipulating the surface electronic structure near ω_s and (ii) surface interband transitions between Shockley states should be responsible for the anomalous linear behaviour of the surface-plasmon dispersion in Ag(100). Furthermore, HREELS experiments on sputtered and nanostructured Ag(100) have shown that the anomaly exhibited by surface plasmons on Ag(100) can indeed be eliminated by modifying the surface structure [286].

Hg. The s–d polarization model devised and used by Liebsch to describe the positive energy dispersion of surface plasmons in Ag [111] was also employed for a description of surface plasmons in Hg [108].

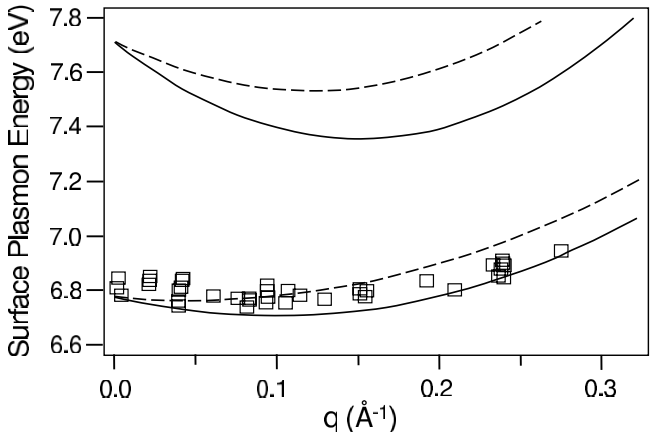

Figure 20. Hg surface-plasmon energy dispersion, as obtained from standard jellium calculations of the RPA and ALDA surface loss function $g(q, \omega)$ of equation (7.74) (upper dashed and solid curves, respectively), from stabilized jellium calculations of the RPA and ALDA surface loss function $g'(q, \omega)$ of equation (8.27) (upper dashed and solid curves, respectively), and from the peak positions observed in experimental electron energy-loss spectra (from [108], used with permission).

At $q = 0$, the measured surface-plasmon energy of this transition metal ($\sim 6.9\,\mathrm{eV}$) lies about 1 eV below the value expected for a bounded electron gas with the density equal to the average density of $6s^2$ valence electrons in Hg ($r_s = 2.65$). This can be explained along the lines described above for Ag (see equation (8.30)), with the use of a polarizable background with $\epsilon_d(\omega_s') = 1.6$.

At finite wave vectors, the s–d screening in Hg is found to considerably distort the surface-plasmon dispersion, as in the case of Ag, but now the linear coefficient of the low-q dispersion being still negative though much smaller than in the absence of d electrons. This is illustrated in figure 20, where the calculated (RPA and ALDA) and measured energy dispersions of the Hg surface plasmon are compared with the corresponding dispersions obtained within a standard jellium model (with $r_s = 2.65$) in the absence of a polarizable medium. This figure clearly shows that in addition to the overall lowering of the surface-plasma frequencies by about 12% relative to the jellium calculations (with no d electrons) the s–d screening leads to a significant flattening of the energy dispersion, thereby bringing the jellium calculations into nice agreement with experiment.

Simple calculations have also allowed to describe correctly the measured broadening of the Hg surface plasmon. As shown in table 2, the Hg surface-plasmon width at $q = 0$ is very well described by simply introducing the measured bulk dielectric function into equation (8.10). For a description of the surface-plasmon broadening at finite q, Kim *at* [108] introduced into equation (8.10) a Drude dielectric function of the form of equation (2.15), but with a q-dependent finite η defined as

$$\eta(q) = \eta(0)\,\mathrm{e}^{-qa}, \tag{8.31}$$

with $a = 3$ Å and $\eta(0) = \Delta\omega_s/\omega_s$ being the measured relative width at $q = 0$. This procedure gives a surface-plasmon linewidth of about 1 eV for all values of q, in reasonable agreement with experiment.

Pd. Collective excitations on transition metals with both sp and d-bands crossing the Fermi level are typically strongly damped by the presence of interband transitions. Pd, however, is known to support collective excitations that are relatively well defined.

Surface plasmons in Pd(110) were investigated with angle-resolved electron-energy-loss spectroscopy by Rocca *et al* [281]. These authors observed a prominent loss feature with a strongly negative linear initial dispersion, which they attributed to a surface-plasmon excitation. At $q = 0$, they found $\omega_s = 7.37\,\text{eV}$ and $\Delta\omega_s \sim 2\,\text{eV}$, in agreement with optical data [287]. At low wave vectors from $q = 0$ up to $q = 0.2\,\text{Å}^{-1}$, they found a linear surface-plasmon dispersion of the form of equation (8.15) with $\alpha = 1\,\text{Å}$. This linear dispersion is considerably stronger than in the case of simple metals (see table 1), and calls for a first-principles description of this material where both occupied and unoccupied sp and d states be treated on an equal footing.

Multipole surface plasmons. Among the noble and transition metals with occupied d bands, multipole surface plasmons have only been observed recently in the case of Ag. In an improvement over previous HREELS experiments, Moresco *et al* [120] performed ELS-LEED experiments with both high-momentum and high-energy resolution, and by substracting the data for two different impact energies they found a peak at 3.72 eV, which was interpreted to be the Ag multipole plasmon. However, Liebsch argued that the frequency of the Ag multipole surface plasmon should be in the 6–8 eV range *above* rather than *below* the bulk plasma frequency, and suggested that the observed peak at 3.72 eV might not be associated with a multipole surface plasmon [121].

Recently, the surface electronic structure and optical response of Ag have been studied on the basis of angle- and energy-resolved photoyield experiments [124]. In these experiments, the Ag multipole surface plasmon is observed at 3.7 eV, but no signature of the multipole surface plasmon is observed above the plasma frequency ($\omega_p = 3.8\,\text{eV}$) in disagreement with the existing theoretical prediction [121].

8.4.3. First-principles calculations. First-principles calculations of the surface-plasmon energy and linewidth dispersion of real solids have been carried out only in the case of the simple-metal prototype surfaces Mg(0001) [118] and Al(111) [119]. These calculations were performed by employing a supercell geometry with slabs containing 16(27) atomic layers of Mg(Al) separated by vacuum intervals. The matrix $\chi^0_{\boldsymbol{g},\boldsymbol{g}'}(z, z'; \boldsymbol{q}, \omega)$ was calculated from equation (7.84), with the sum over n and n' running over bands up to energies of 30 eV above the Fermi level, the sum over $\boldsymbol{k}$ including 7812 points, and the single-particle orbitals $\psi_{\boldsymbol{k},n;i}(\boldsymbol{r}) = \psi_{\boldsymbol{k},n}(\boldsymbol{r}_\parallel)\psi_i(z)$ being expanded in a plane-wave basis set with a kinetic-energy cutoff of 12 Ry. The surface-response function $g_{\boldsymbol{g}=0,\boldsymbol{g}'=0}(\boldsymbol{q}, \omega)$ was then calculated from equation (7.86) including $\sim$ 300 3D reciprocal-lattice vectors in the evaluation of the RPA or TDDFT Fourier coefficients $\chi_{\boldsymbol{g},\boldsymbol{g}'}(z, z'; \boldsymbol{q}, \omega)$ of equation (7.83). Finally, the dispersion of the energy and linewidth of surface plasmons was calculated from the maxima of the imaginary part of $g_{\boldsymbol{g}=0,\boldsymbol{g}'=0}(\boldsymbol{q}, \omega)$ for various values of the magnitude and the direction of the 2D wave vector $\boldsymbol{q}$.

The *ab initio* calculations reported in [118, 119] for the surface-plasmon energy dispersion of Mg(0001) and Al(111) with the 2D wave vector along various symmetry directions show that (i) there is almost perfect isotropy of the surface-plasmon energy dispersion, (ii) there is excellent agreement with experiment (thereby accurately accounting for core polarization not presented in jellium models), as long as the nonlocal (momentum-dependent) static XC local-field factor of equation (5.24) is employed in the evaluation of the interacting density-response function, and (iii) if the corresponding jellium calculations are normalized to the measured value ω_s at $q = 0$ (as shown in figure 13 by the thick solid line with open circles) *ab initio* and jellium calculations are found to be nearly indistinguishable.

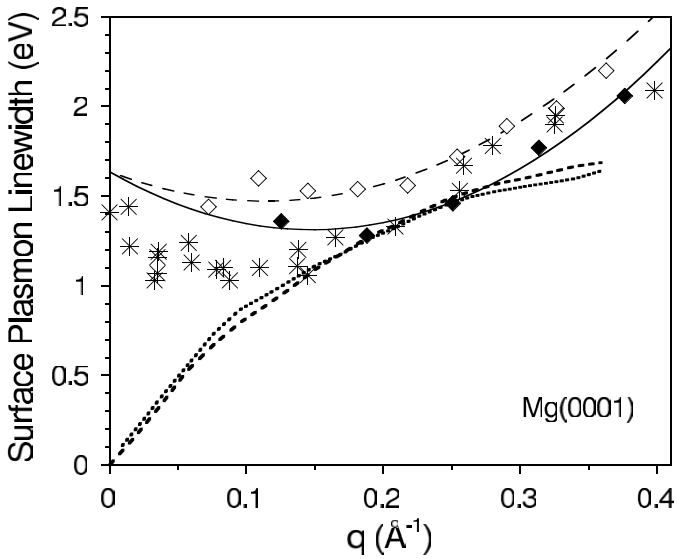

Figure 21. Linewidth of surface plasmons in Mg(0001), as a function of the magnitude of the 2D wave vector $\boldsymbol{q}$. The filled (open) diamonds represent *ab initio* calculations [118], as obtained with $\boldsymbol{q}$ along the $\bar{\Gamma}\bar{M}$ ($\bar{\Gamma}\bar{K}$) direction by employing the static XC local-field factor of equation (5.24) in the evaluation of the Fourier coefficients of the interacting density-response function. The solid and long dashed lines represent the best fit of the *ab initio* calculations. The short dashed and dotted lines correspond to jellium and 1D model-potential calculations, also obtained by employing the static XC local-field factor of equation (5.24). Stars represent the experimental data reported in [101].

Ab initio calculations also show that the band structure is of paramount importance for a correct description of the surface-plasmon linewidth. First-principles TDDFT calculations of the Mg(0001) and Al(111) surface-plasmon linewidth dispersions along various symmetry directions are shown in figures 21 and 22, respectively. Also shown in this figures are the experimental measurements reported in [95, 101] (stars) and the corresponding jellium calculations (dashed lines). For small 2D wave vectors, the agreement between theory and experiment is not as good as in the case of the surface-plasmon energy dispersion (which can be attributed to finite-size effects of the supercell geometry). Nevertheless, *ab initio* calculations for Mg(0001) (see figure 21) yield a negative slope for the linewidth dispersion at small $\boldsymbol{q}$, in agreement with experiment, and properly account for the experimental linewidth dispersion at intermediate and large wave vectors. Figure 21 also shows that the Mg(0001) surface-plasmon linewidth dispersion depends considerably on the direction of the 2D wave vector, and that the use of the parametrized one-dimensional model potential reported in [248] (dotted line) does not improve the jellium calculations. As for Al(111), we note that band-structure effects bring the jellium calculations closer to experiment; however, *ab initio* calculations are still in considerable disagreement with the measurements reported in [95, 264], especially at the lowest wave vectors. At the moment it is not clear the origin of such a large discrepancy between theory and experiment. On the other hand, considerable disagreement is also found between the measured surface-plasmon linewidth at $q \sim 0$ reported in [95] ($\Delta\omega_s \sim 1.9\,\text{eV}$) and [264] ($\Delta\omega_s \sim 2.3\,\text{eV}$) and the value derived (see table 2) from the imaginary part of the surface-response function of equation (8.10) with measured values of the bulk dielectric function ($\Delta\omega_s = 0.38\,\text{eV}$).

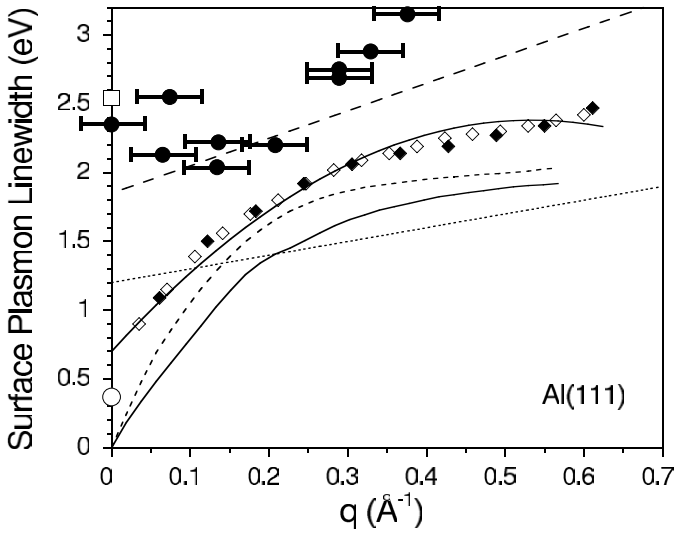

Figure 22. Linewidth of surface plasmons in Al(111), as a function of the magnitude of the 2D wave vectors $\boldsymbol{q}$. The filled (open) diamonds represent *ab initio* ALDA calculations, as obtained with $\boldsymbol{q}$ along the $\bar{\Gamma}\bar{M}$ ($\bar{\Gamma}\bar{K}$) [119]. The thin solid line represents the best fit of the *ab initio* calculations. The dashed (solid) line represents the jellium model (1D model potential) dispersion. Long dashed and dotted lines are the experimental data of [95] for Al(111) and (100) respectively. The open circle at $q = 0$ is the linewidth derived from optical measurements of the Al bulk dielectric function [163]. The open square at $q = 0$ shows the linewidth obtained from surface-loss measurements [163]. The measured values from [264] are represented by dots with error bars.

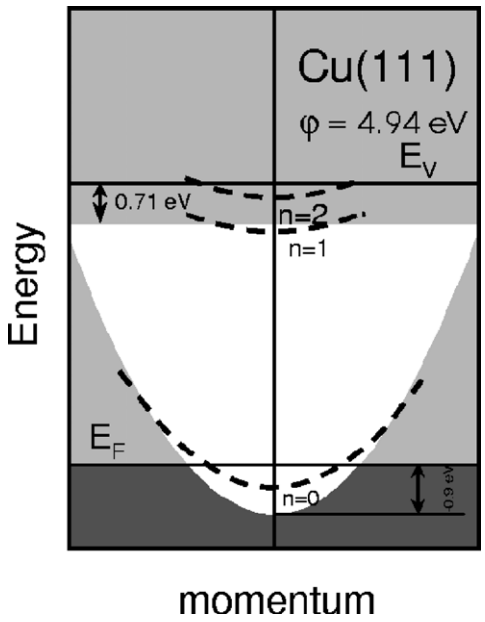

Figure 23. Schematic representation of the surface band structure on Cu(111) near the $\bar{\Gamma}$ point. The shaded region represents the projection of the bulk bands.

Table 5. 2D Fermi energy (ε_F^{2D}) of surface states at the $\bar{\Gamma}$ point of Be(0001) and the (111) surfaces of the noble metals Cu, Ag, and Au. v_F^{2D} and m^{2D} represent the corresponding 2D Fermi velocity and effective mass, respectively. v_F^{2D} is expressed in units of the Bohr velocity $v_0 = e^2/\hbar$.

	ε_F^{2D}(eV)	v_F^{2D}/v_0	m^{2D}
Be(0001)	2.75	0.41	1.18
Cu(111)	0.44	0.28	0.42
Ag(111)	0.065	0.11	0.44
Au(111)	0.48	0.35	0.28

8.5. Acoustic surface plasmons

A variety of metal surfaces, such as Be(0001) and the (111) surfaces of the noble metals Cu, Ag, and Au, are known to support a partially occupied band of Shockley surface states within a wide energy gap around the Fermi level (see figure 23) [288, 289]. Since these states are strongly localized near the surface and disperse with momentum parallel to the surface, they can be considered to form a quasi 2D surface-state band with a 2D Fermi energy ε_F^{2D} equal to the surface-state binding energy at the $\bar{\Gamma}$ point (see table 5).

In the absence of the 3D substrate, a Shockley surface state would support a 2D collective oscillation, the energy of the corresponding plasmon being given by [173]

$$\omega_{2D} = (2\pi n^{2D} q)^{1/2}, \tag{8.32}$$

with n^{2D} being the 2D density of occupied surface states, i.e,

$$n^{2D} = \varepsilon_F^{2D}/\pi. \tag{8.33}$$

Equation (8.32) shows that at very long wavelengths plasmons in a 2D electron gas have low energies; however, they do not affect e–ph interaction and phonon dynamics near the Fermi level, due to their square-root dependence on the wave vector. Much more effective than ordinary 2D plasmons in mediating, e.g. superconductivity would be the so-called acoustic plasmons with sound-like long-wavelength dispersion.

Recently, it has been shown that in the presence of the 3D substrate the dynamical screening at the surface provides a mechanism for the existence of a *new* acoustic collective mode, the so-called acoustic surface plasmon, whose energy exhibits a linear dependence on the 2D wave number [125–127]. This *novel* surface-plasmon mode has been observed at the (0001) surface of Be, showing a linear energy dispersion that is in very good agreement with first-principles calculations [128].

8.5.1. A simple model. First of all, we consider a simplified model in which surface-state electrons comprise a 2D electron gas at $z = z_d$ (see figure 24), while all other states of the semi-infinite metal comprise a 3D substrate at $z \leqslant 0$ represented by the Drude dielectric function of equation (2.15). Within this model, one finds that both e–h and collective excitations occurring within the 2D gas can be described with the use of an effective 2D dielectric function, which in the RPA takes the form [127]

$$\epsilon_{\text{eff}}^{2D}(q,\omega) = 1 - W(z_d, z_d; q, \omega)\, \chi_{2D}^0(q,\omega), \tag{8.34}$$

$W(z, z'; q, \omega)$ being the screened interaction of equation (7.59), and $\chi_{2D}^0(q,\omega)$ being the noninteracting density-response function of a homogeneous 2D electron gas [173].

In the absence of the 3D substrate, $W(z, z'; q, \omega)$ reduces to the bare Coulomb interaction $v(z, z'; q)$, and $\epsilon_{\text{eff}}^{2D}(q,\omega)$ coincides, therefore, with the RPA dielectric function of a 2D electron

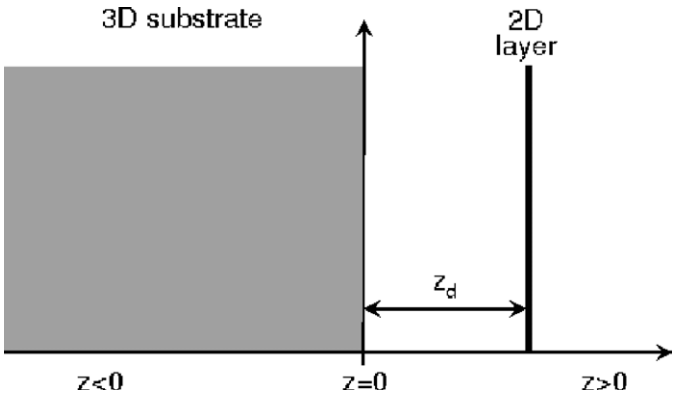

Figure 24. Surface-state electrons comprise a 2D sheet of interacting free electrons at $z = z_d$. All other states of the semi-infinite metal comprise a plane-bounded 3D electron gas at $z \leqslant 0$. The metal surface is located at $z = 0$.

gas, which in the long-wavelength ($q \to 0$) limit has one single zero corresponding to collective excitations at $\omega = \omega_{2D}$.

In the presence of a 3D substrate, the long-wavelength limit of $\epsilon^{2D}_{\rm eff}(q, \omega)$ is found to have two zeros. One zero corresponds to a high-frequency ($\omega \gg v_F q$) oscillation of energy

$$\omega^2 = \omega_s^2 + \omega_{2D}^2, \tag{8.35}$$

in which 2D and 3D electrons oscillate in phase with one another. The other zero corresponds to a low-frequency *acoustic* oscillation in which both 2D and 3D electrons oscillate out of phase; for this zero to be present, the long-wavelength ($q \to 0$) limit of the low-frequency ($\omega \to 0$) screened interaction $W(z_d, z_d; q, \omega)$,

$$I(z_d) = \lim_{q \to 0} W(z_d, z_d; q, \omega \to 0), \tag{8.36}$$

must be different from zero. The energy of this low-frequency mode is then found to be of the form [127]

$$\omega = \alpha\, v_F^{2D}\, q, \tag{8.37}$$

where

$$\alpha = \sqrt{1 + \frac{[I(z_d)]^2}{\pi\,[\pi + 2\, I(z_d)]}}. \tag{8.38}$$

Local 3D response. If one characterizes the 3D substrate by a Drude dielectric function of the form of equation (2.15), the 3D screened interaction $W(z_d, z_d; q, \alpha v_F q)$ is easily found to be

$$W(z_d, z_d; q, \alpha v_F q) = \begin{cases} 0 & z_d \leqslant 0 \\ & \\ 4\pi\, z_d & z_d > 0 \end{cases}. \tag{8.39}$$

Hence, in the presence of a 3D substrate that is *spatially separated* from the 2D sheet ($z_d > 0$), introduction of $I(z_d) = 4\pi\, z_d$ into equation (8.38) yields at $z_d \gg 1$:

$$\alpha = \sqrt{2 z_d}, \tag{8.40}$$

which is the result first obtained by Chaplik in his study of charge-carrier crystallization in low-density inversion layers [290].

If the 2D sheet is located inside the 3D substrate ($z_d \leqslant 0$), $I(z_d) = 0$, which means that the effective dielectric function of equation (8.34) has no zero at low energies ($\omega < \omega_s$). Hence, in a local picture of the 3D response the characteristic collective oscillations of the 2D electron gas would be completely screened by the surrounding 3D substrate, and no low-energy acoustic mode would exist. This result had suggested over the years that acoustic plasmons should only exist in the case of *spatially separated* plasmas, as pointed out by Das Sarma and Madhukar [291].

Nevertheless, Silkin *et al* [125] have demonstrated that metal surfaces where a partially occupied quasi-2D surface-state band *coexists* in the same region of space with the underlying 3D continuum can indeed support a well-defined acoustic surface plasmon. This acoustic collective oscillation has been found to appear as the result of a combination of the nonlocality of the 3D dynamical screening and the spill out of the 3D electron density into the vacuum [127].

Self-consistent 3D response. Figures 25(a) and 25(b) exhibit self-consistent RPA calculations of the effective dielectric function of equation (8.34) corresponding to the (0001) surface of Be, with $q = 0.01\, a_0^{-1}$ (figure 25a) and $q = 0.1\, a_0^{-1}$ (figure 25b). The real and imaginary parts of the effective dielectric function (thick and thin solid lines, respectively) have been displayed for $z_d = 0$, as approximately occurs with the quasi-2D surface-state band in Be(0001). Also shown in these figures (dotted lines) is the energy-loss function $\mathrm{Im}\left[-1/\epsilon_{\mathrm{eff}}^{2D}(q\omega)\right]$ for the 2D sheet located inside the metal at $z_d = -\lambda_F$, at the jellium edge ($z_d = 0$), and outside the metal at $z_d = \lambda_F/2$ and $z_d = \lambda_F$.

Collective excitations are related to a zero of $\mathrm{Re}\,\epsilon_{\mathrm{eff}}^{2D}(q,\omega)$ in a region where $\mathrm{Im}\,\epsilon_{\mathrm{eff}}^{2D}(q,\omega)$ is small, which yields a maximum in the energy-loss function $\mathrm{Im}\left[-1/\epsilon_{\mathrm{eff}}^{2D}(q,\omega)\right]$. For the 2D electron density under study ($r_s^{2D} = 3.12$), in the absence of the 3D substrate a 2D plasmon would occur at $\omega_{2D} = 1.22$ eV for $q = 0.01 a_0^{-1}$ and $\omega_{2D} = 3.99$ eV for $q = 0.1 a_0^{-1}$. However, in the presence of the 3D substrate (see figure 25) a well-defined low-energy *acoustic* plasmon occurs at energies (above the upper edge $\omega_u = v_F q + q^2/2$ of the 2D e–h pair continuum) dictated by equation (8.37) with the sound velocity αv_F being just over the 2D Fermi velocity v_F ($\alpha > 1$). When the 2D sheet is located far inside the metal surface, the sound velocity is found to approach the Fermi velocity ($\alpha \to 1$). When the 2D sheet is located far outside the metal surface, the coefficient α approaches the classical limit ($\alpha \to \sqrt{2z_d}$) of equation (8.40).

Finally, we note that apart from the limiting case $z_d = \lambda_F$ and $q = 0.01\, a_0^{-1}$ (which yields a plasmon linewidth negligibly small) the small width of the plasmon peak exhibited in figure 25 is entirely due to plasmon decay into e–h pairs of the 3D substrate.

8.5.2. 1D model calculations. For a more realistic (but still simplified) description of electronic excitations at the (0001) surface of Be and the (111) surface of the noble metals Cu, Ag, and Au, the 1D model potential $v_{MP}(z)$ of [248] was employed in [125, 126]. The use of this model potential allows to assume translational invariance in the plane of the surface and to trace, therefore, the presence of collective excitations to the peaks of the imaginary part of the jellium-like surface response function of equation (7.73). The important difference between the screened interaction $W(z, z'; q, \omega)$ used here to evaluate $g(q, \omega)$ and the screened interaction used in equation (8.34) in the framework of the simple model described above lies in the fact that the single-particle orbitals $\psi_i(z)$ and energies ϵ_i are now obtained by solving equation (7.65) with the jellium Kohn–Sham potential $v_{KS}[n_0](z)$ replaced by the

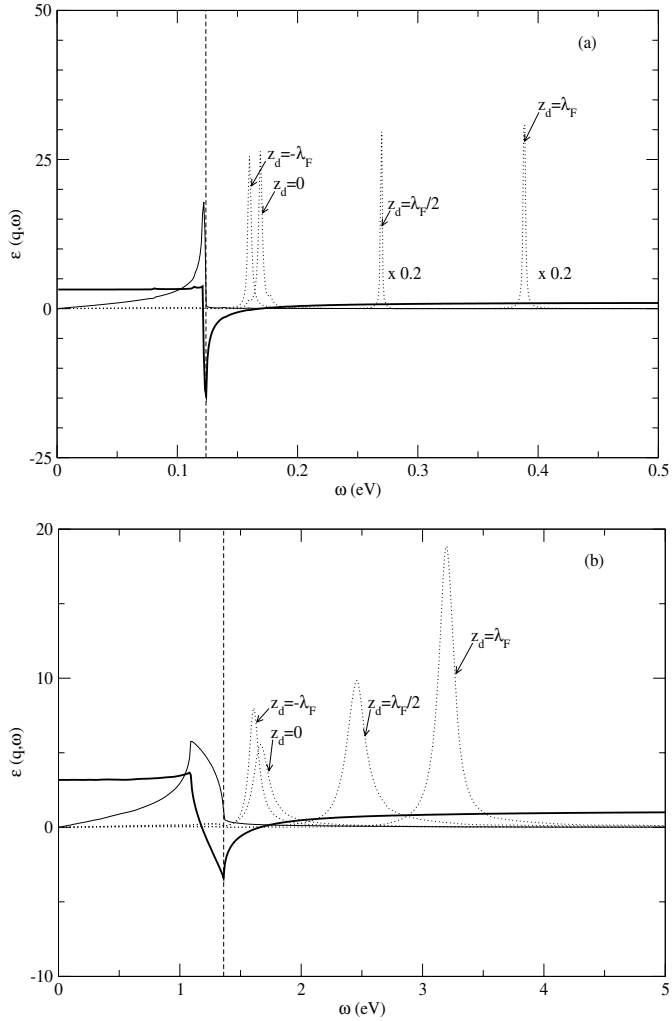

Figure 25. Effective dielectric function of a 2D sheet that is located at the jellium edge ($z_d = 0$), as obtained from equation (8.34) and self-consistent RPA calculations of the 3D screened interaction $W(z_d, z_d; q, \omega)$ and the 2D density-response function $\chi^{2D}(q, \omega)$ with (a) $q = 0.01$ and (b) $q = 0.1$ [127]. The real and imaginary parts of $\epsilon_{\rm eff}(q, \omega)$ are represented by thick and thin solid lines, respectively. The dotted lines represent the effective 2D energy-loss function $\mathrm{Im}[-\epsilon_{\rm eff}^{-1}(q, \omega)]$ for $z_d = -\lambda_F$, $z_d = \lambda_F/2$ and $z_d = \lambda_F$. The vertical dashed line represents the upper edge $\omega_u = v_F q + q^2/2m$ of the 2D e–h pair continuum, where 2D e–h pairs can be excited. The calculations presented here for $z_d = \lambda_F$ and $q = 0.01\, a_0^{-1}$ have been carried out by replacing the energy ω by a complex quantity $\omega + i\eta$ with $\eta = 0.05$ eV. All remaining calculations have been carried out for real frequencies, i.e. with $\eta = 0$. The 2D and 3D electron-density parameters have been taken to be $r_s^{2D} = 3.14$ and $r_s = 1.87$, corresponding to Be(0001).

model potential $v_{\rm MP}(z)$. Since this model potential has been shown to reproduce the key features of the surface band structure and, in particular, the presence of a Shockley surface state within an energy gap around the Fermi level of the materials under study, it provides a realistic description of surface-state electrons moving in the presence of the 3D substrate.

Figure 26 shows the imaginary part of the surface-response function of equation (7.73), as obtained for Be(0001) and for increasing values of q by using the 1D model potential $v_{\rm MP}(z)$

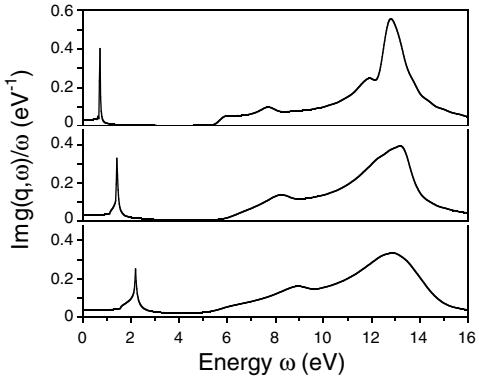

Figure 26. Energy loss function $\mathrm{Im}[g(q,\omega)]/\omega$ of Be(0001) versus the excitation energy ω, obtained from equation (7.73) with the use of the 1D model potential of [248], as reported in [125]. The magnitude of the wave vector $\boldsymbol{q}$ has been taken to be 0.05 (top panel), 0.1 (middle panel), and 0.15 (bottom panel), in units of the inverse Bohr radius a_0^{-1}. In the long-wavelength limit ($q \to 0$), $g(q,\omega)$ is simply the total electron density induced by the potential of equation (7.75).

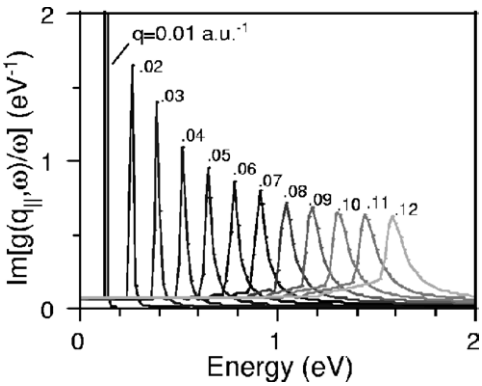

Figure 27. Energy loss function $\mathrm{Im}[g(q,\omega)]/\omega$ of Be(0001) versus the excitation energy ω obtained from equation (7.73) with the use of the 1D model potential of [248] and for various values of q [293].

of [248]. As follows from the figure, the excitation spectra is clearly dominated by two distinct features: (i) the conventional surface plasmon at $\hbar\omega_s \sim 13\,\mathrm{eV}$, which can be traced to the characteristic pole that the surface-response function $g(q,\omega)$ of a bounded 3D free electron gas with $r_s^{3D} = 1.87$ exhibits at this energy[23], and (ii) a well-defined low-energy peak with *linear* dispersion.

That the low-frequency mode that is visible in figure 26 has linear dispersion is clearly shown in figure 27, where the imaginary part of the surface-response function $g(q,\omega)$ of Be(0001) is displayed at low energies for increasing values of the magnitude of the wave vector in the range $q = 0.01 - 0.12\,a_0^{-1}$. The excitation spectra is indeed dominated at low energies by a well-defined *acoustic* peak at energies of the form of equation (8.37) with an α coefficient that is close to unity, i.e. the sound velocity being at long wavelengths very close to the 2D Fermi velocity v_F^{2D} (see table 5).

The energy-loss function $\mathrm{Im}\, g(q,\omega)$ of the (111) surfaces of the noble metals Cu, Ag,

[23] This surface plasmon would also be present in the absence of surface states, i.e. if the 1D model potential v_{MP} of [248] were replaced by the jellium Kohn–Sham potential of equation (5.13).

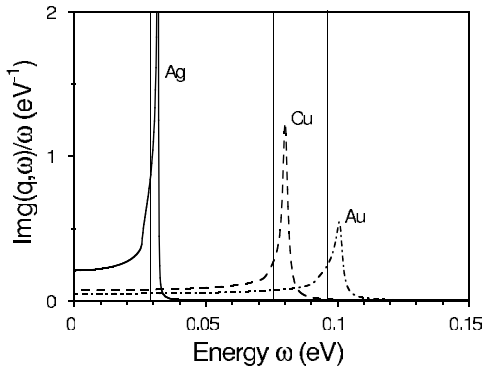

Figure 28. Energy-loss function Im$[g(q,\omega)]/\omega$ of the (111) surfaces of the noble metals Cu, Ag and Au [126], shown by solid, dashed, and dashed-dotted lines, respectively, versus the excitation energy ω, as obtained from equation (7.73) with the use of the 1D model potential of [248] and for $q = 0.01\, a_0^{-1}$ and $\eta = 1$ meV. The vertical solid lines are located at the energies $\omega = v_{\rm F}^{\rm 2D}\, q$, which would correspond to equation (8.37) with $\alpha = 1$.

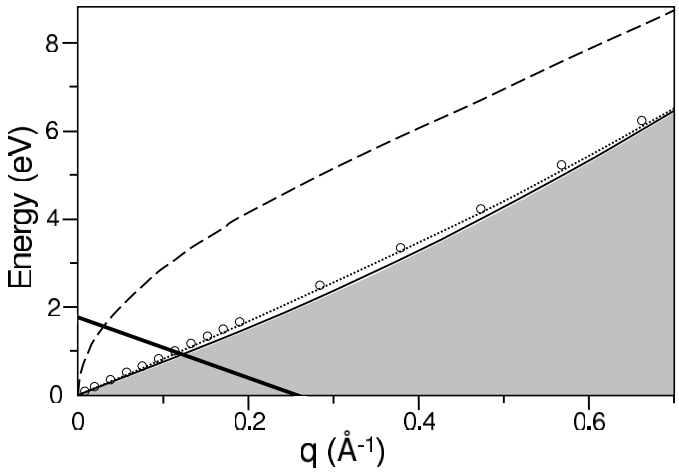

Figure 29. The solid line shows the energy of the acoustic surface plasmon of Be(0001) [125], as obtained from the maxima of the calculated surface-loss function Im $g(q,\omega)$ shown in figure 27. The thick dotted line and the open circles represent the maxima of the energy-loss function Im$[-1/\epsilon_{\rm eff}(q,\omega)]$ obtained from equation (8.34) with $z_{\rm d}$ far inside the solid (thick dotted line) and with $z_{\rm d} = 0$ (open circles). The dashed line is the plasmon dispersion of a 2D electron gas in the absence of the 3D system. The grey area indicates the region of the (q,ω) plane (with the upper limit at $\omega_{\rm 2D}^{\rm up} = v_{\rm F}^{\rm 2D} q + q^2/2m_{\rm 2D}$) where e–h pairs can be created within the 2D Shockley band of Be(0001). The area below the thick solid line corresponds to the region of momentum space where transitions between 3D and 2D states cannot occur. The quantities $\omega_{\rm inter}^{\rm min}$ and $q^{\rm min}$ are determined from the surface band structure of Be(0001). 2D and 3D electron densities have been taken to be those corresponding to the Wigner radii $r_{\rm s}^{\rm 2D} = 3.14$ and $r_{\rm s}^{\rm 3D} = 1.87$, respectively.

and Au is displayed in figure 28 for $q = 0.01\, a_0^{-1}$. This figure shows again the presence of a well-defined low-energy collective excitation whose energy is of the form of equation (8.37) with $\alpha \sim 1$.

Figure 29 shows the energy of the acoustic surface plasmon of Be(0001) versus q (solid line), as derived from the maxima of the calculated Im $g(q,\omega)$ of figure 27 (solid line) and

Figure 30. A periodic grating of constant L. The grating periodic structure can provide an impinging free electromagnetic radiation with additional momentum $2\pi/L$.

from the maxima of the effective energy-loss function $\mathrm{Im}[-1/\epsilon_{\mathrm{eff}}(q,\omega)]$ (see figure 25) obtained from equation (8.34) for $z_{\mathrm{d}} = 0$ (dashed line). Little discrepancies between these two calculations should be originated in (i) the absence in the simplified model leading to equation (8.34) of transitions between 2D and 3D states, and (ii) the nature of the decay and penetration of the surface-state orbitals, which in the framework of the model leading to equation (8.34) are assumed to be fully localized in a 2D sheet at $z = z_{\mathrm{d}}$.

8.5.3. First-principles calculations. First-principles calculations of the imaginary part of the surface-response function $g_{\boldsymbol{g}=0,\boldsymbol{g}=0}(\boldsymbol{q},\omega)$ of Be(0001) have been carried out recently [128], and it has been found that this metal surface is indeed expected to support an acoustic surface plasmon whose energy dispersion agrees with the solid line represented in figure 29 (if the dispersion of figure 29 calculated for surface state effective mass $m = 1$ is scaled according to the *ab initio* value $m = 1.2$ [292]). Furthermore, these calculations have been found to agree closely with recent high-resolution EELS measurements on the (0001) surface of Be [128] (under grazing incidence), which represent the first evidence of the existence of acoustic surface plasmons.

8.5.4. Excitation of acoustic surface plasmons. As in the case of the conventional surface plasmon at the Ritchie's frequency ω_{s}, acoustic surface plasmons should be expected to be excited not only by moving electrons (as occurs in the EELS experiments reported recently [128]) but also by light. Now we focus on a possible mechanism that would lead to the excitation of acoustic surface plasmons by light in, e.g. vicinal surfaces with high indices [293].

At long wavelengths ($q \to 0$), the acoustic surface-plasmon dispersion curve is of the form of equation (8.37) with $\alpha \sim 1$. As the 2D Fermi velocity $v_{\mathrm{F}}^{\mathrm{2D}}$ is typically about three orders of magnitude smaller than the velocity of light, there is, in principle, no way that incident light can provide an ideal surface with the correct amount of momentum and energy for the excitation of an acoustic surface plasmon to occur. As in the case of conventional surface plasmons, however, a periodic corrugation or grating in the metal surface should be able to provide the missing momentum.

Let us consider a periodic grating of constant L (see figure 30). If light hits such a surface, the grating periodic structure can provide the impinging free electromagnetic waves with additional momentum arising from the grating periodic structure. If free electromagnetic radiation hits the grating at an angle θ, its wave vector along the grating surface has magnitude

$$q = \frac{\omega}{c}\,\sin\theta \pm \frac{2\pi}{L}\,n, \tag{8.41}$$

where L represents the grating constant, and $n = 1, 2, \ldots$. Hence, the linear (nearly vertical) dispersion relation of free light changes into a set of parallel straight lines, which can match the acoustic–plasmon dispersion relation as shown in figure 31.

For a well-defined acoustic surface plasmon in Be(0001) to be observed, the wave number q needs to be smaller than $q \sim 0.06\,a_0^{-1}$ (see figure 29)[24]. For $q = 0.05\,a_0^{-1}$, equation (8.41) with

[24] Acoustic surface plasmons in Be(0001) have been observed for energies up to 2 eV [128].

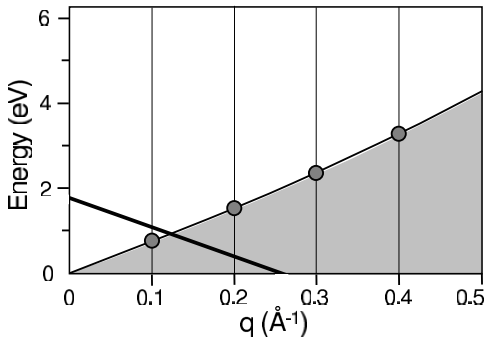

Figure 31. A schematic representation of the dispersion relation of acoustic surface plasmons (solid line) and free light impinging on a periodic grating of constant L (essentially vertical dotted lines).

$n = 1$ yields a grating constant $L = 66\,\text{Å}$. Acoustic surface plasmons of energy $\omega \sim 0.6\,\text{eV}$ could be excited in this way. Although a grating period of a few nanometres sounds unrealistic with present technology, the possible control of vicinal surfaces with high indices could provide appropriate grating periods in the near future.

9. Applications

Surface plasmons have been employed over the years in a wide spectrum of studies ranging from condensed matter and surface physics [9–24] to electrochemistry [25], wetting [26], biosensing [27, 28, 29], scanning tunnelling microscopy [30], the ejection of ions from surfaces [31], nanoparticle growth [32, 33], surface-plasmon microscopy [34, 35] and surface-plasmon resonance technology [36–42]. Renewed interest in surface plasmons has come from recent advances in the investigation of the optical properties of nanostructured materials [43, 44], one of the most attractive aspects of these collective excitations now being their use to concentrate light in subwavelength structures and to enhance transmission through periodic arrays of subwavelength holes in optically thick metallic films [45, 46], as well as the possible fabrication of nanoscale photonic circuits operating at optical frequencies [48] and their use as mediators in the transfer of energy from donor to acceptor molecules on opposite sides of metal films [67].

Here we focus on two distinct applications of collective electronic excitations at metal surfaces: the role that surface plasmons play in particle–surface interactions and the new emerging field called plasmonics.

9.1. Particle–surface interactions: energy loss

Let us consider a recoilless fast point particle of charge Z_1 moving in an arbitrary inhomogeneous many-electron system at a given impact vector $\boldsymbol{b}$ with nonrelativistic velocity $\boldsymbol{v}$, for which retardation effects and radiation losses can be neglected[25]. Using Fermi's golden rule of time-dependent perturbation theory, the lowest-order probability for the probe particle

[25] This approximation is valid for heavy charged particles, e.g. ions and also for swift electrons moving with nonrelativistic velocities that are large compared to the velocity of target electrons. In the case of electrons, $Z_1 = -1$.

to transfer momentum $\boldsymbol{q}$ to the medium is given by the following expression [294]:

$$P_{\boldsymbol{q}} = -\frac{4\pi}{LA} Z_1^2 \int_0^\infty \mathrm{d}\omega \int \frac{\mathrm{d}\boldsymbol{q}'}{(2\pi)^3} \mathrm{e}^{\mathrm{i}\boldsymbol{b}\cdot(\boldsymbol{q}+\boldsymbol{q}')} \times \mathrm{Im} W(\boldsymbol{q}, \boldsymbol{q}'; \omega)\, \delta(\omega - \boldsymbol{q}\cdot\boldsymbol{v})\, \delta(\omega + \boldsymbol{q}'\cdot\boldsymbol{v}), \tag{9.1}$$

where L and A represent the normalization length and area, respectively, and $W(\boldsymbol{q}, \boldsymbol{q}'; \omega)$ is the double Fourier transform of the screened interaction $W(\boldsymbol{r}, \boldsymbol{r}'; \omega)$ of equation (7.4):

$$W(\boldsymbol{q}, \boldsymbol{q}'; \omega) = \int \mathrm{d}\boldsymbol{r} \int \mathrm{d}\boldsymbol{r}'\, \mathrm{e}^{-\mathrm{i}(\boldsymbol{q}\cdot\boldsymbol{r}+\boldsymbol{q}'\cdot\boldsymbol{r}')}\, W(\boldsymbol{r}, \boldsymbol{r}'; \omega). \tag{9.2}$$

Alternatively, the total decay rate τ^{-1} of the probe particle can be obtained from the knowledge of the imaginary part of the self-energy. In the GW approximation of many-body theory [295], and replacing the probe-particle Green function by that of a non-interacting recoilless particle, one finds [250]:

$$\tau^{-1} = -2\, Z_1^2 \sum_f \int \mathrm{d}\boldsymbol{r} \int \mathrm{d}\boldsymbol{r}'\, \phi_{\mathrm{i}}^*(\boldsymbol{r})\, \phi_{\mathrm{f}}^*(\boldsymbol{r}') \mathrm{Im} W(\boldsymbol{r}, \boldsymbol{r}'; \varepsilon_{\mathrm{i}} - \varepsilon_{\mathrm{f}})\, \phi_{\mathrm{i}}(\boldsymbol{r}')\, \phi_{\mathrm{f}}(\boldsymbol{r}), \tag{9.3}$$

where $\phi_{\mathrm{i}}(\boldsymbol{r})$ represents the probe-particle initial state of energy ε_{i}, and the sum is extended over a complete set of final states $\phi_{\mathrm{f}}(\boldsymbol{r})$ of energy ε_{f}. Describing the probe-particle initial and final states by plane waves in the direction of motion and a Dirac δ function in the transverse direction, i.e.

$$\phi(\boldsymbol{r}) = \frac{1}{\sqrt{A}} \mathrm{e}^{\mathrm{i}\boldsymbol{v}\cdot\boldsymbol{r}} \sqrt{\delta(\boldsymbol{r}_\perp - \boldsymbol{b})}, \tag{9.4}$$

where $\boldsymbol{r}_\perp$ represents the position vector perpendicular to the projectile velocity, one finds that the decay rate of equation (9.3) reduces indeed to a sum over the probability $P_{\boldsymbol{q}}$ of equation (9.1), i.e.

$$\tau^{-1} = \frac{1}{T} \sum_{\boldsymbol{q}} P_{\boldsymbol{q}}, \tag{9.5}$$

T being a normalization time.

For a description of the total energy ΔE that the moving probe particle loses due to electronic excitations in the medium, one can first define the time-dependent probe-particle charge density

$$\rho^{\mathrm{ext}}(\boldsymbol{r}, t) = Z_1\, \delta(\boldsymbol{r} - \boldsymbol{b} - \boldsymbol{v}\, t), \tag{9.6}$$

and one then obtains the energy that this classical particle loses per unit time as follows [87]

$$-\frac{\mathrm{d}E}{\mathrm{d}t} = -\int \mathrm{d}\boldsymbol{r}\, \rho^{\mathrm{ext}}(\boldsymbol{r}, t)\, \frac{\partial V^{\mathrm{ind}}(\boldsymbol{r}, t)}{\partial t}, \tag{9.7}$$

where $V^{\mathrm{ind}}(\boldsymbol{r}, t)$ is the potential induced by the probe particle at position $\boldsymbol{r}$ and time t, which to first order in the external perturbation yields (see equation (7.1)):

$$V^{\mathrm{ind}}(\boldsymbol{r}, t) = \int \mathrm{d}\boldsymbol{r}' \int_{-\infty}^{+\infty} \mathrm{d}t' \int_{-\infty}^{+\infty} \frac{\mathrm{d}\omega}{2\pi} \mathrm{e}^{-\mathrm{i}\omega(t-t')}\, \tilde{W}^{\mathrm{ind}}(\boldsymbol{r}, \boldsymbol{r}'; \omega)\, \rho^{\mathrm{ext}}(\boldsymbol{r}', t') \tag{9.8}$$

with

$$\tilde{W}(\boldsymbol{r}, \boldsymbol{r}'; \omega) = W(\boldsymbol{r}, \boldsymbol{r}'; \omega) - v(\boldsymbol{r}, \boldsymbol{r}'), \tag{9.9}$$

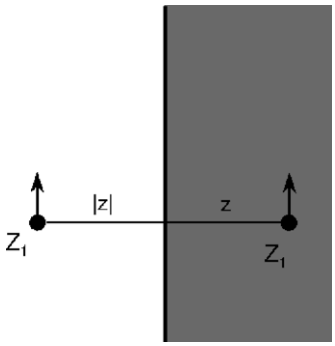

Figure 32. Particle of charge Z_1 moving with constant velocity at a fixed distance z from the surface of a plane-bounded electron gas. Inside the solid, the presence of the surface causes (i) a decrease of loss at the bulk-plasmon frequency ω_p varying with z as $\sim K_0(2\omega_p z/v)$ and (ii) an additional loss at the surface-plasmon frequency ω_s varying with z as $\sim K_0(2\omega_s z/v)$. Outside the solid, energy losses are dominated by a surface-plasmon excitation at ω_s.

Finally, one writes:

$$-\Delta E = \int_{-\infty}^{+\infty} \mathrm{d}t \left(-\frac{\mathrm{d}E}{\mathrm{d}t}\right). \tag{9.10}$$

Introducing equations (9.6) and (9.8) into equation (9.7), and equation (9.7) into equation (9.10), one finds that the total energy loss ΔE can indeed be written as a sum over the probability $P_{\boldsymbol{q}}$ of equation (9.1), i.e.

$$-\Delta E = \sum_{\boldsymbol{q}} (\boldsymbol{q}\cdot\boldsymbol{v})\, P_{\boldsymbol{q}}, \tag{9.11}$$

where $\boldsymbol{q}\cdot\boldsymbol{v}$ is simply the energy transferred by our recoilless probe particle to the medium.

9.1.1. Planar surface. In the case of a plane-bounded electron gas that is translationally invariant in two directions, which we take to be normal to the z axis, equations (9.6)–(9.8) yield the following expression for the energy that the probe particle loses per unit time:

$$-\frac{\mathrm{d}E}{\mathrm{d}t} = \mathrm{i}\,\frac{Z_1^2}{\pi}\int \frac{\mathrm{d}^2\boldsymbol{q}}{(2\pi)^2}\int_{-\infty}^{+\infty}\mathrm{d}t'\int_0^{\infty}\mathrm{d}\omega\,\omega \mathrm{e}^{-\mathrm{i}(\omega-\boldsymbol{q}\cdot\boldsymbol{v}_\parallel)(t-t')}\,\tilde{W}[z(t),z(t');q,\omega], \tag{9.12}$$

where $\boldsymbol{q}$ is a 2D wave vector in the plane of the surface, $\boldsymbol{v}_\parallel$ represents the component of the velocity that is parallel to the surface, $z(t)$ represents the position of the projectile relative to the surface, and $\tilde{W}(z,z';q,\omega)$ is the 2D Fourier transform of $\tilde{W}(\boldsymbol{r},\boldsymbol{r}';\omega)$.

In the simplest possible model of a bounded semi-infinite electron gas in vacuum, in which the screened interaction $W(z,z';q,\omega)$ is given by the classical expression equation (7.8) with ϵ_1 being the Drude dielectric function of equation (2.15) and $\epsilon_2 = 1$, explicit expressions can be found for the energy lost per unit path length by probe particles that move along a trajectory that is either parallel or normal to the surface.

Parallel trajectory. In the case of a probe particle moving with constant velocity at a fixed distance z from the surface (see figure 32), introduction of equation (7.8) into equation (9.12)

yields [293]

$$-\frac{\mathrm{d}E}{\mathrm{d}x}=\frac{Z_1^2}{v^2}\begin{cases}\omega_\mathrm{p}^2\left[\ln(k_\mathrm{c}v/\omega_\mathrm{p})-K_0(2\omega_\mathrm{p}z/v)\right]+\omega_\mathrm{s}^2\,K_0(2\omega_\mathrm{s}z/v), & z<0,\\ \omega_\mathrm{s}^2\,K_0(2\omega_\mathrm{s}|z|/v), & z>0,\end{cases}\tag{9.13}$$

where $K_0(\alpha)$ is the zero-order modified Bessel function [241], and k_c denotes the magnitude of a wave vector above which long-lived bulk plasmons are not sustainable.

For particle trajectories outside the solid ($z>0$), equation (9.13) reproduces the classical expression of Echenique and Pendry [22], which was found to describe correctly EELS experiments [131] and which was extended to include relativistic corrections [296]. For particle trajectories inside the solid ($z>0$), equation (9.13) reproduces the result first obtained by Nuñez *et al* [297]. Outside the solid, the energy loss is dominated by the excitation of surface plasmons at ω_s. When the particle moves inside the solid, the effect of the boundary is to cause (i) a decrease in loss at the bulk plasma frequency ω_p, which in an infinite electron gas would be $-\mathrm{d}E/\mathrm{d}x=Z_1^2\omega_\mathrm{p}^2\ln(k_\mathrm{c}v/\omega_\mathrm{p})/v^2$ and (ii) an additional loss at the surface-plasma frequency ω_s.

Nonlocal effects that are absent in the classical equation (9.13) were incorporated approximately by several authors in the framework of the hydrodynamic approach and the specular-reflection model described in sections 7.2.1 and 7.2.2 [298–303]. More recently, extensive RPA and ALDA calculations of the energy-loss spectra of charged particles moving near a jellium surface were carried out [245] within the self-consistent scheme described in section 7.2.3. At high velocities (of a few Bohr units) and for charged particles moving far from the surface into the vacuum, the actual energy loss was found to converge with the classical limit dictated by the first line of equation (9.13). However, at low and intermediate velocities substantial changes in the energy loss were observed as a realistic description of the surface response was considered.

Corrections to the energy loss of charged particles (moving far from the surface into the vacuum) due to the finite width of the surface-plasmon resonance that is not present, in principle, in jellium self-consistent calculations, have been discussed recently [304]. These corrections have been included to investigate the energy loss of highly charged ions undergoing distant collisions at grazing incidence angles with the internal surface of microcapillary materials, and it has been suggested that the correlation between the angular distribution and the energy loss of transmitted ions can be used to probe the dielectric properties of the capillary material.

For a more realistic description of the energy loss of charged particles moving near a Cu(111) surface, the Kohn–Sham potential $v_\mathrm{KS}(z)$ used in the self-consistent jellium calculations of [245] was replaced in [305] by the 1D model potential v_MP of [248]. It was shown, however, that although the Cu(111) surface exhibits a wide band gap around the Fermi level and a well-defined Shockley surface state the energy loss expected from this model does not differ significantly from its jellium counterpart. This is due to the fact that the presence of the surface state compensates the reduction of the energy loss due to the band gap.

Existing first-principles calculations of the interaction of charged particles with solids invoke periodicity of the solid in all directions and neglect, therefore, surface effects and, in particular, the excitation of surfaces plasmons [306, 307]. An exception is a recent first-principles calculation of the energy loss of ions moving parallel with a Mg(0001) surface [308], which accounts naturally for the finite width of the surface-plasmon resonance that is present neither in the self-consistent jellium calculations of [245] nor in the 1D model calculations of [305].

A typical situation in which charged particles can be approximately assumed to move along a trajectory that is parallel to a solid surface occurs in the glancing-incidence geometry, where

ions penetrate into the solid, they skim the outermost layer of the solid, and are then specularly repelled by a repulsive, screened Coulomb potential, as discussed by Gemell [309]. By first calculating the ion trajectory under the combined influence of the repulsive planar potential and the attractive image potential, the total energy loss can be obtained approximately as follows

$$\Delta E = 2v \int_{z_{\rm tp}}^{\infty} \frac{{\rm d}E}{{\rm d}x}(z) \left[v_z(z)\right]^{-1} {\rm d}z, \tag{9.14}$$

$z_{\rm tp}$ and $v_z(z)$ denoting the turning point and the value of the component of the velocity normal to the surface, respectively, which both depend on the angle of incidence.

Accurate measurements of the energy loss of ions being reflected from a variety of solid surfaces at grazing incidence have been reported by several authors [310–314]. In particular, Winter *et al* [312] carried out measurements of the energy loss of protons being reflected from Al(111). From the analysis of their data at 120 keV, these authors deduced the energy loss ${\rm d}E/{\rm d}x(z)$ and found that at large distances from the surface the energy loss follows closely the energy loss expected from the excitation of surface plasmons. Later on, RPA jellium calculations of the energy loss from the excitation of valence electrons were combined with a first-Born calculation of the energy loss due to the excitation of the inner shells and reasonably good agreement with the experimental data was obtained for all angles of incidence [315].

Normal trajectory. Let us now consider a situation in which the probe particle moves along a normal trajectory from the vacuum side of the surface ($z > 0$) and enters the solid at $z = t = 0$. The position of the projectile relative to the surface is then $z(t) = -vt$. Assuming that the electron gas at $z \leqslant 0$ can be described by the Drude dielectric function of equation (2.15) and introducing equation (7.8) into equation (3.8) yields [293]:

$$-\frac{{\rm d}E}{{\rm d}z} = \frac{Z_1^2}{v^2} \begin{cases} \omega_{\rm p}^2 \left[\ln(k_{\rm c} v/\omega_{\rm p}) - h(\omega_{\rm p} z/v)\right] + \omega_{\rm s}^2\, h(\omega_{\rm s} z/v), & z < 0 \\ \omega_{\rm s}^2\, f(2\omega_{\rm s}|z|/v), & z > 0, \end{cases} \tag{9.15}$$

where

$$h(\alpha) = 2\cos(\alpha)\, f(\alpha) - f(2\alpha), \tag{9.16}$$

with $f(\alpha)$ being given by the following expression:

$$f(\alpha) = \int_0^{\infty} \frac{x\, {\rm e}^{-\alpha x}}{1+x^2}\, {\rm d}x. \tag{9.17}$$

Equation (9.15) shows that (i) when the probe particle is moving outside the solid the effect of the boundary is to cause energy loss at the surface-plasmon energy $\omega_{\rm s}$, and (ii) when the probe particle is moving inside the solid the effect of the boundary is to cause both a decrease in loss at the bulk-plasmon energy $\omega_{\rm p}$ and an additional loss at the surface-plasmon energy $\omega_{\rm s}$, as predicted by Ritchie [1].

Now we consider the real situation in which a fast charged particle passes through a *finite* foil of thickness a (see figure 33). Assuming that the foil is thick enough for the effect of each boundary to be the same as in the case of a semi-infinite medium, and integrating along the whole trajectory from minus to plus infinity, one finds the total energy that the probe particle loses to collective excitations:

$$-\Delta E = \frac{Z_1^2}{v^2}\left[a\,\omega_{\rm p}^2 \ln\frac{k_{\rm c} v}{\omega_{\rm p}} - \frac{\pi}{2}\omega_{\rm p} + \pi\,\omega_{\rm s}\right]. \tag{9.18}$$

This is the result first derived by Ritchie in a different way [1], which brought him to the realization that surface collective excitations exist at the lowered frequency $\omega_{\rm s}$. The first

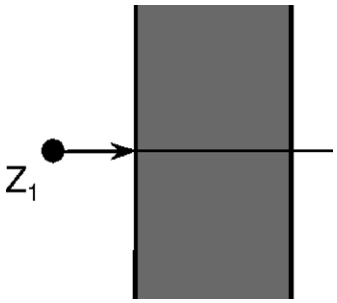

Figure 33. Particle of charge Z_1 passing perpendicularly through a finite foil of thickness a. The presence of the boundaries leads to a decrease in the energy loss at the bulk-plasmon frequency ω_p and an additional loss at the surface-plasmon frequency ω_s, the net boundary effect being an increase in the total energy loss in comparison to the case of a particle moving in an infinite medium with no boundaries.

term of equation (9.18), which is proportional to the thickness of the film represents the bulk contribution, which would also be present in the absence of the boundaries. The second and third terms, which are both due to the presence of the boundaries and become more important as the foil thickness decreases, represent the decrease in the energy loss at the plasma frequency ω_p and the energy loss at the lowered frequency ω_s, respectively. Equation (9.18) also shows that the net boundary effect is an increase in the total energy loss above the value which would exist in its absence, as noted by Ritchie [1]. A more accurate jellium self-consistent description of the energy loss of charged particles passing through thin foils has been performed recently in the RPA and ALDA [316].

9.2. STEM: valence EELS

The excitation of both surface plasmons on solid surfaces and localized Mie plasmons on small particles has attracted great interest over the years in the fields of scanning transmission electron microscopy [130–135] and near-field optical spectroscopy [136].

EELS of fast electrons in STEM shows two types of losses, depending on the nature of the excitations that are produced in the sample: atomically defined core-electron excitations at energies $\omega > 100\,\mathrm{eV}$ and valence-electron (mainly collective) excitations at energies up to $\sim 50\,\mathrm{eV}$. Core-electron excitations occur when the probe moves across the target, and provide chemical information about atomic-size regions of the target [317]. Conversely, valence-electron excitations provide information about the surface structure with a resolution of the order of several nanometres. One advantage of valence EELS is that it provides a strong signal, even for non-penetrating trajectories (the so-called *aloof beam energy loss spectroscopy* [318, 319]), and generates less specimen damage [131].

The central quantity in the interpretation of valence EELS experiments is the total probability $P(\omega)$ for the STEM beam to exchange energy ω with the sample. In terms of the screened interaction $W(\boldsymbol{r}, \boldsymbol{r}'; \omega)$ and for a probe electron in the state $\phi_0(\boldsymbol{r})$ with energy ε_0, first-order perturbation theory yields:

$$P(\omega) = -2 \sum_f \int \mathrm{d}\boldsymbol{r} \int \mathrm{d}\boldsymbol{r}'\, \phi_f^*(\boldsymbol{r}')\, \phi_0(\boldsymbol{r}')\, \phi_f(\boldsymbol{r})\, \phi_0^*(\boldsymbol{r}) \mathrm{Im} W(\boldsymbol{r}, \boldsymbol{r}'; \omega)\, \delta[\omega - \varepsilon_0 - \varepsilon_F], \qquad (9.19)$$

where the sum is extended over a complete set of final states $\phi_f(\boldsymbol{r})$ of energy ε_f. For probe electrons moving on a definite trajectory (and having, therefore, a charge density of the form

of equation (9.6) with no beam recoil), the total energy loss ΔE of equations (9.10) and (9.11) can be expressed in the expected form

$$\Delta E = \int_0^\infty \mathrm{d}\omega\, \omega\, P(\omega). \tag{9.20}$$

Ritchie and Howie [320] showed that, in EELS experiments where all the inelastic scattering is collected, treating the fast electrons as a classical charge of the form of equation (9.6) is indeed adequate. Nonetheless, quantal effects due to the spatial extension of the beam have been addressed by several authors [133, 321, 322].

9.2.1. Planar surface. In the case of a classical beam of electrons moving with constant velocity at a fixed distance z from a planar surface (see figure 32), the initial and final states can be described by taking a δ function in the transverse direction and plane waves in the direction of motion. Neglecting recoil, the probability $P(\omega)$ of equation (9.19) then takes the following form:

$$P(\omega) = -\frac{1}{\pi^2 v} \int_0^\infty \mathrm{d}q_x\, \mathrm{Im}\, W(z, z; q, \omega), \tag{9.21}$$

with $q = \sqrt{q_x^2 + (\omega/v)^2}$.

In a classical model in which the screened interaction $W(z, z'; q, \omega)$ is given by the classical expression equation (7.8), the probability $P(\omega)$ is easy to calculate. In particular, if the beam of electrons is moving outside the sample, one finds:

$$W(z, z; q, \omega) = \frac{2\pi}{q} \left[1 - g\, \mathrm{e}^{-2qz}/\epsilon_2\right], \tag{9.22}$$

with the surface-response function g given by equation (7.9). Introduction of equation (9.22) into equation (9.21) yields the classical probability

$$P(\omega) = \frac{2L}{\pi v^2} K_0(2\omega z/v)\, \mathrm{Im} g(\omega), \tag{9.23}$$

which in the case of a Drude metal in vacuum yields

$$P(\omega) = L\, \frac{\omega_\mathrm{s}}{v^2}\, \delta(\omega - \omega_\mathrm{s}), \tag{9.24}$$

and, therefore (see equation (9.20)), the energy loss per unit path length given by equation (9.13) with $Z_1 = -1$ and $z > 0$.

The classical equation (9.22) can be easily extended to the case in which the sample is formed by a semi-infinite medium characterized by ϵ_1 and covered by a layer of dielectric function ϵ_3 and thickness a. One finds:

$$W(z, z; q, \omega) = \frac{2\pi}{q} \left[1 - \mathrm{e}^{-2qz} \frac{\xi_{32} + \xi_{13}\, \mathrm{e}^{2qa}}{\xi_{32}\xi_{13} + \mathrm{e}^{2qa}}\right], \tag{9.25}$$

where

$$\xi_{32} = \frac{\epsilon_3 - \epsilon_2}{\epsilon_3 + \epsilon_2} \tag{9.26}$$

and

$$\xi_{13} = \frac{\epsilon_1 - \epsilon_3}{\epsilon_1 + \epsilon_3}. \tag{9.27}$$

Equations (9.25)–(9.27) show that while for a clean surface ($a = 0$) the energy-loss function $P(\omega)$ is dominated by the excitation of surface plasmons at $\omega = \omega_\mathrm{s}$ (see equation (9.24)), EELS should be sensitive to the presence of sub-surface structures. This effect was observed by Batson [130] in the energy-loss spectra corresponding to an Al surface coated with an Al_2O_3 layer of increasing thickness.

9.2.2. Spheres.

Definite trajectories. In the case of a classical beam of electrons moving with constant velocity at a fixed distance b from the centre of a single sphere of radius a and dielectric function $\epsilon_1(\omega)$ that is immersed in a host medium of dielectric function $\epsilon_2(\omega)$, the initial and final states can be described (as in the case of the planar surface) by taking a δ function in the transverse direction and plane waves in the direction of motion. If recoil is neglected and the classical screened interaction of equations (7.11)–(7.13) is used, then equation (9.19) yields the following expression for the energy-loss probability [132]:

$$P(\omega) = \frac{4a}{\pi v^2} \sum_{l=1}^{\infty} \sum_{m=0}^{l} \frac{\mu_m}{(l-m)(l+m)} \left[\frac{\omega a}{v}\right]^{2l} \times K_m^2(\omega_b/v)\, \mathrm{Im} g_l(\omega), \tag{9.28}$$

for outside trajectories ($a \leqslant b$), and [323]

$$P(\omega) = \frac{4a}{\pi v^2} \sum_{l=1}^{\infty} \sum_{m=0}^{l} \mu_m \frac{(l-m)}{(l+m)} \left\{ \left[A^0_{\mathrm{lm}} + A^i_{\mathrm{lm}}\right]^2 \mathrm{Im} g_l(\omega) + A^i_{\mathrm{lm}} \left[A^0_{\mathrm{lm}} + A^i_{\mathrm{lm}}\right] \mathrm{Im}\left[\epsilon^{-1}(\omega)\right] \right\}, \tag{9.29}$$

for inside trajectories ($a \geqslant b$), with

$$A^0_{\mathrm{lm}}(\omega) = \frac{1}{a} \int_{\mathrm{c}}^{\infty} \mathrm{d}x \left[\frac{\sqrt{b^2+x^2}}{a}\right]^{l+1} P_l^m \left[\frac{x}{\sqrt{b^2+x^2}}\right] c_{\mathrm{lm}}(\omega x/v) \tag{9.30}$$

and

$$A^i_{\mathrm{lm}}(\omega) = \frac{1}{a} \int_{0}^{c} \mathrm{d}x \left[\frac{\sqrt{b^2+x^2}}{a}\right]^{l} P_l^m \left[\frac{x}{\sqrt{b^2+x^2}}\right] c_{\mathrm{lm}}(\omega x/v). \tag{9.31}$$

Here, $c = \sqrt{a^2-b^2}$, $P_l^m(x)$ denote Legendre functions, $c_{\mathrm{lm}}(x) = \cos(x)$, if $(l+m)$ is even, os $\sin(x)$, if $(l+m)$ is odd, and $g_l(\omega)$ denotes the classical function of equation (7.13), which has poles at the classical surface-plasmon condition of equation (3.33).

Equations (9.28) and (9.29) show that an infinite number of multipolar modes can be excited, in general, which contribute to the energy loss of moving electrons. It is known, however, that for small spheres with $a \ll v/\omega_{\mathrm{s}}$ the dipolar mode ($l = 1$) dominates, which in the case of a Drude sphere in vacuum occurs at $\omega_1 = \omega_{\mathrm{p}}/\sqrt{3}$. For spheres with $a \sim v/\omega_{\mathrm{s}}$, many multipoles contribute with similar weight. For very large spheres ($a \gg v/\omega_{\mathrm{s}}$) and $a < b$, the main contribution arises from high multipolar modes occurring approximately at the planar surface plasmon energy ω_{s}, since in the limit of large l $g_l(\omega)$ of equation (7.13) reduces to the energy-loss function of equation (7.9). Indeed, this is an expected result, due to the fact that for very large spheres the probe electron effectively interacts with an almost planar surface.

Broad beam. We now consider a broad beam geometry, and we therefore describe the probe electron states by plane waves of the form:

$$\phi_0(\boldsymbol{r}) = \frac{1}{\sqrt{\Omega}} \mathrm{e}^{\mathrm{i}\boldsymbol{k}_0 \cdot \boldsymbol{r}} \tag{9.32}$$

and

$$\phi_{\mathrm{f}}(\boldsymbol{r}) = \frac{1}{\sqrt{\Omega}} \mathrm{e}^{\mathrm{i}\boldsymbol{k}_{\mathrm{f}} \cdot \boldsymbol{r}}, \tag{9.33}$$

where Ω represents the normalization volume. Then, introducing equations (9.32), (9.33) and (7.11)–(7.13) into equation (9.19), and neglecting recoil, one finds

$$P(\omega) = \frac{1}{\pi^2} \int \frac{\mathrm{d}\boldsymbol{Q}}{Q^2} \,\mathrm{Im}\left[-\epsilon_{\mathrm{eff}}^{-1}(Q,\omega)\right] \delta(\omega - \boldsymbol{Q}\cdot\boldsymbol{v}). \tag{9.34}$$

This is precisely the energy-loss probability corresponding to a probe electron moving in a 3D homogeneous electron gas but with the inverse dielectric function $\epsilon^{-1}(Q,\omega)$ replaced by the effective inverse dielectric function $\epsilon_{\mathrm{eff}}^{-1}(Q,\omega)$ of equation (7.16).

9.2.3. Cylinders.

Definite trajectory. In the case of a classical beam of electrons moving with constant velocity at a fixed distance b from the axis of a single cylinder of radius a and dielectric function $\epsilon_1(\omega)$ that is immersed in a host medium of dielectric function $\epsilon_2(\omega)$, the initial and final states can be described (as in the case of the planar surface) by taking a δ function in the transverse direction and plane waves in the direction of motion. If recoil is neglected and the classical screened interaction of equations (7.19)–(7.22) is used, then equation (9.19) yields the following expression for the energy-loss probability [135]:

$$P(\omega) = -\frac{2}{\pi v}\mathrm{Im}\left\{(\epsilon_1^{-1} - \epsilon_2^{-1}) \times \sum_{m=0}^{\infty} \mu_m \left[I_m\left(\frac{\omega b}{v}\right) K_m\left(\frac{\omega b}{v}\right) + \frac{\epsilon_2 K_m(\frac{\omega a}{v}) K_m'(\frac{\omega a}{v}) I_m^2\left(\frac{\omega b}{v}\right)}{\epsilon_1 I_m'(\frac{\omega a}{v}) K_m(\frac{\omega a}{v}) - \epsilon_2 I_m(\frac{\omega a}{v}) K_m'(\frac{\omega a}{v})} \right] \right\}, \tag{9.35}$$

for inside trajectories ($a \leqslant b$), and

$$P(\omega) = -\frac{2}{\pi v}\mathrm{Im}\left\{(\epsilon_1^{-1} - \epsilon_2^{-1}) \sum_{m=0}^{\infty} \mu_m \frac{\epsilon_1 I_m(\frac{\omega a}{v}) I_m'(\frac{\omega a}{v}) K_m^2\left(\frac{\omega b}{v}\right)}{\epsilon_1 I_m'(\frac{\omega a}{v}) K_m(\frac{\omega a}{v}) - \epsilon_2 I_m(\frac{\omega a}{v}) K_m'(\frac{\omega a}{v})} \right\}, \tag{9.36}$$

for outside trajectories ($a \geqslant b$). In particular, for axial trajectories ($b = 0$), the energy-loss probability $P(\omega)$ is due exclusively to the $m = 0$ mode.

Broad beam. For a broad beam geometry the probe electron states can be described by plane waves of the form of equations (9.32) and (9.33), which after introduction into equation (9.19), neglecting recoil, and using the classical screened interaction of equations (7.19)–(7.22) yield an energy-loss probability of the form of equation (9.34) but now with the inverse dielectric function $\epsilon^{-1}(Q,\omega)$ replaced by the effective inverse dielectric function $\epsilon_{\mathrm{eff}}^{-1}(Q,\omega)$ of equation (7.25).

9.3. Plasmonics

Renewed interest in surface plasmons has come from recent advances in the investigation of the electromagnetic properties of nanostructured materials [43,44], one of the most attractive aspects of these collective excitations now being their use to concentrate light in subwavelength structures and to enhance transmission through periodic arrays of subwavelength holes in optically thick metallic films [45,46]. Surface-plasmon polaritons are tightly bound to metal–dielectric interfaces penetrating around 10 nm into the metal (the so-called skin-depth) and typically more than 100 nm into the dielectric (depending on the wavelength), as shown in figure 4. Indeed, surface plasmons of an optical wavelength concentrate light in a region that is considerably smaller than their wavelength, a feature that suggests the possibility of

using surface-plasmon polaritons for the fabrication of nanoscale photonic circuits operating at optical frequencies [47, 48].

Here we discuss only a few aspects of the most recent research that has been carried out in the so-called field of plasmonics. This constitutes an important area of research, since surface-plasmon based circuits are known to merge the fields of photonics and electronics at the nanoscale, thereby enabling to overcome the existing difficulties related to the large size mismatch between the micrometre-scale bulky components of photonics and the nanometre-scale electronic chips. Indeed, the surface-plasmon polariton described in section 2 can serve as a base for constructing nano-circuits that will be able to carry optical signals and electric currents. These optoelectronic circuits would consist of various components such as couples, waveguides, switches, and modulators.

In order to transmit optical signals to nanophotonic devices and to efficiently increase the optical far-field to near-field conversion, a nanodot coupler (fabricated from a linear array of closely spaced metallic nanoparticles) has been combined recently with a surface-plasmon polariton condenser (working as a phase array) fabricated from hemispherical metallic nanoparticles [49]. By focusing surface-plasmon polaritons with a spot size as small as 400 nm at $\lambda = 785$ nm, their transmission length through the nanodot coupler was confirmed to be three times longer than that of a metallic-core waveguide, owing to the efficient near-field coupling between the localized surface plasmon of neighboring nanoparticles.

Achieving control of the light–solid interactions involved in nanophotonic devices requires structures that guide electromagnetic energy with a lateral mode confinement below the diffraction limit of light. It was suggested that this so-called subwavelength-sized wave guiding can occur along chains of closely spaced metal nanoparticles that convert the optical mode into surface (Mie) plasmons [50]. The existence of guided long-range surface-plasmon waves was observed experimentally by using thin metal films [51–53], nanowires [54, 55], closely spaced silver rods [56] and metal nanoparticles [57].

The propagation of guided surface plasmons is subject to significant ohmic losses that limit the maximum propagation length. In order to avoid these losses, various geometries have been devised using arrays of features of nanosize dimensions [58, 59]. The longest propagation length (13.6 mm) has been achieved with a structure consisting of a thin lossy metal film lying on a dielectric substrate and covered by a different dielectric superstrate [60]. The main issue in this context is to strongly confine the surface-plasmon field in the cross section perpendicular to the surface-plasmon propagation direction, while keeping relatively low propagation losses. Recently, it has been pointed out that strongly localized channel plasmon polaritons (radiation waves guided by a channel cut into a planar surface of a solid characterized by a negative dielectric function [61]) exhibit relatively low propagation losses [62]. The first realization and characterization of the propagation of channel plasmon polaritons along straight subwavelength metal grooves was reported by Bozhevilnyi *et al* [63]. More recently, the design, fabrication, and characterization of channel plasmon polariton based subwavelength waveguide components have been reported; these are Y-splitters, Mach-Zehnder interferometers and waveguide-ring resonators operating at telecom wavelengths [64].

In the framework of plasmonics, modulators and switches have also been investigated. Switches should serve as an active element to control surface-plasmon polariton waves [65, 66]. This approach takes advantage of the strong dependence of the propagation of surface-plasmon polaritons on the dielectric properties of the metal in a thin surface layer that may be manipulated using light. This idea was realized introducing a few-micron long gallium switching section to a gold-on-silica waveguide [66]. An example of an active plasmonic device has been demonstrated by using a thin silver film covered from both sides by thin

polymer films with molecular chromophores [67]. In this case, coupled surface-plasmon polaritons provide an effective transfer of excitation energy from donor molecules to acceptor molecules on the opposite sides of a metal film up to 120 nm thick.

Another emerging area of active research in the field of plasmonics is based on the generation and manipulation of electromagnetic radiation of various wavelengths from microwave to optical frequencies. For instance, the coating of semiconductor quantum wells by nanometre metal films results in an increased spontaneous emission rate in the semiconductor that leads to the enhancement of light emission. This enhancement is due to an efficient energy transfer from electron–hole pair recombination in the quantum well to surface-plasmon polaritons at the surface of semiconductor heterostructures coated by metal. Recently, a 32-fold increase in the spontaneous emission rate at 440 nm in an InGaN/GaN quantum well has been probed by time-resolved photoluminescence spectroscopy [324]. Also probed has been the enhancement of photoluminescence up to an order of magnitude through a thin metal film from organic light emitting diodes, by removing the surface-plasmon polariton quenching with the use of a periodic nanostructure [325].

Recent theoretical and experimental work also suggest that surface-plasmon polaritons play a key role both in the transmission of electromagnetic waves through a single aperture and the enhanced transmission of light through subwavelength hole arrays [45,326–328]. This enhanced transmission has also been observed at millimetre-waves and micro-waves [329,330] and at THz-waves [331].

Finally, we note that surface-plasmon polaritons have been used in the field of nanolithography. This surface-plasmon based nanolithography can produce subwavelength structures at surfaces, such as sub100 nm lines with visible light [332–335]. On the other hand, the enhancement of evanescent waves through the excitation of surface plasmons led Pendry [336] to the concept of the so-called superlens [337].

Acknowledgments

Partial support by the University of the Basque Country, the Basque Unibertsitate eta Ikerketa Saila, the Spanish Ministerio de Educación y Ciencia and the EC 6th framework Network of Excellence NANOQUANTA (Grant No NMP4-CT-2004-500198) is acknowledged. One of us (JMP) would like to acknowledge fruitful discussions with A Howie and the hospitality of Churchill College and the Cavendish Laboratory of the University of Cambridge, where part of this review was written.

References

[1] Ritchie R H 1957 *Phys. Rev.* **106** 874
[2] Pines D and Bohm D 1952 *Phys. Rev.* **85** 338
[3] Pines D 1956 *Rev. Mod. Phys.* **28** 184
[4] Tonks L and Langmuir I 1929 *Phys. Rev.* **33** 195
[5] Ruthemann G 1942 *Naturwiss* **30** 145
Ruthemann G 1948 *Ann. Phys.* **2** 113
[6] Lang W 1948 *Optik* **3** 233
[7] Powell C J and Swan J B 1959 *Phys. Rev.* **115** 869
Powell C J and Swan J B 1959 *Phys. Rev.* **116** 81
[8] Stern E A and Ferrell R A 1960 *Phys. Rev.* **120** 130
[9] Inglesfield J E and Wikborg E 1975 *J. Phys. F: Metal Phys.* **5** 1475
[10] Zaremba E and Kohn W 1976 *Phys. Rev.* B **13** 2270
[11] Sernelius B E 2005 *Phys. Rev.* B **71** 235114
[12] Feibelman P J 1971 *Surf. Sci.* **27** 438

[13] Ritchie R H 1972 *Phys. Lett.* A **38** 189
[14] Ray R and Mahan G D 1972 *Phys. Lett.* A **42** 301
[15] Šunjić M, Toulouse G and Lucas A A 1972 *Solid State Commun.* **11** 1629
[16] Gadzuk J W and Metiu H 1980 *Phys. Rev.* B **22** 2603
[17] Schmit J and Lucas A 1972 *Solid State Commun.* **11** 415
Schmit J and Lucas A 1972 *Solid State Commun.* **11** 419
[18] Wikborg E and Inglesfield J E 1977 *Phys. Scr.* **15** 37
Lang N D and Sham L J 1975 *Solid State Commun.* **17** 581
[19] Langreth D C and Perdew J P 1977 *Phys. Rev.* B **15** 2884
[20] Chabal Y J and Sievers A J 1980 *Phys. Rev. Lett.* **44** 944
[21] Persson B and Ryberg R 1985 *Phys. Rev. Lett.* **54** 2119
[22] Echenique P M and Pendry J B 1975 *J. Phys. C: Solid State Phys.* **8** 2936
[23] Echenique P M, Ritchie R H, Barberán N and Inkson J 1981 *Phys. Rev.* B **23** 6486
[24] Ueba H 1992 *Phys. Rev.* B **45** 3755
[25] Knoll W 1998 *Annu. Rev. Phys. Chem.* **49** 569
[26] Herminghaus S, Vorberg J, Gau H, Conradt R, Reinelt D, Ulmer H, Leiderer P and Przyrembel M 1997 *Ann. Phys. Lpz.* **6** 425
[27] Malmqvist M 1993 *Nature* **261** 186
[28] Braguglia C M 1998 *Chem. Biochem. Eng. Q.* **12** 183
[29] Chien F C and Chen S J 2004 *Biosensors Bioelectron.* **20** 633
[30] Berndt R, Gimzewski J K and Johansson P 1991 *Phys. Rev. Lett.* **67** 3796
[31] Shea M J and Compton R N 1993 *Phys. Rev.* B **47** 9967
[32] Jin R C, Cao Y W, Mirkin C A, Kelly K L, Schatz G C and Zheng J G 2001 *Science* **294** 1901
[33] Jin R, Cao C, Hao E, Métraux G S, Schatz G C and Mirkin C 2003 *Nature* **425** 487
[34] Rothenhäusler B and Knoll W 1988 *Nature* **332** 615
[35] Flätgen G, Krischer K, Pettinger B, Doblhofer K, Junkes H and Ertl G 1995 *Science* **269** 668
[36] Gordon J G and Ernst S 1980 *Surf. Sci.* **101** 499
[37] Liedberg B, Nylander C and Lundstrom I 1983 *Sensors Actuators* **4** 299
[38] Schuster S C, Swanson R V, Alex L A Bourret R B and Simon M I 1993 *Nature* **365** 343
[39] Schuck P 1997 *Curr. Opin. Biotechnol.* **8** 498
Schuck P 1997 *Annu. Rev. Biophys. Biomol. Struct.* **26** 541
[40] Homola J, Yee S S and Gauglitz G 1999 *Sensors Actuators* B **54** 3
[41] Mendelsohn A R and Brend R 1999 *Science* **284** 1948
[42] Green R J, Frazier R A, Shakesheff K M, Davies M C, Roberts C J and Tendler S J B 2000 *Biomaterials* **21** 1823
[43] Pendry J B 1999 *Science* **285** 1687
[44] Prodan E, Radloff C, Halas N J and Nordlander P 2003 *Science* **302** 419
[45] Ebbesen T W, Lezec H J, Ghaemi H F, Thio T and Wolff P A 1998 *Nature* **391** 667
[46] Lezec H J, Degiron A, Devaux E, Linke R A, Martin-Moreno L, Garcia-Vidal F J and Ebbesen T W 2002 *Science* **297** 820
[47] Ozbay E 2006 *Science* **311** 189
[48] Barnes W L, Dereux A and Ebbesen T W 2003 *Nature* **424** 824
[49] Nomura W, Ohtsu M and Yatsui T 2005 *Appl. Phys. Lett.* **86** 181108
[50] Quinten M, Leitner A, Krenn J R and Aussenegg F R 1998 *Opt. Lett.* **23** 1331
[51] Charbonneau R, Berini P, Berolo E and Lisicka-Shrzek E 2000 *Opt. Lett.* **25** 844
[52] Lamprecht B, Krenn J R, Schider G, Ditlbacher H, Salerno M, Felid j N, Leitner A, Aussenegg F R and Weeber J C 2001 *Appl. Phys. Lett.* **79** 51
[53] Nikolajsen T, Leosson K, Salakhutdinov I and Bozhevolnyi S I 2003 *Appl. Phys. Lett.* **82** 668
[54] Krenn J R, Lamprecht B, Ditlbacher H, Schider G, Saleno M, Leitner A and Aussenegg F R 2002 *Europhys. Lett.* **60** 663
[55] Krenn J R and Weeber J C 2004 *Philos. Trans. R. Soc. Lond. Ser.* A **362** 739
[56] Maier S A, Kik P G, Atwater H A, Meltzer S, Harel E, Koel B E and Requicha A A G 2003 *Nature Mater.* **2** 229
[57] Murray W A, Astilean S and Barens W L 2004 *Phys. Rev.* B **69** 165407
[58] Maier S A, Barclay P E, Johnson T J, Friedman M D and Painter O 2004 *Appl. Phys. Lett.* **84** 3990
[59] Maier S A, Friedman M D, Barclay P E and Painter O 2005 *Appl. Phys. Lett.* **86** 071103
[60] Berini P, Charbonneau R, Lahoud N and Mattiussi G 2005 *J. Appl. Phys.* **98** 043109
[61] Novikov I V and Maradudin A A 2002 *Phys. Rev.* B **66** 035403

[62] Pile D F P and Gramotnev D K 2004 *Opt. Lett.* **29** 1069
Pile D F P and Gramotnev D K 2004 *Appl. Phys. Lett.* **85** 6323
[63] Bozhevilnyi S I, Volkov V S, Devaux E and Ebbesen T W 2005 *Phys. Rev. Lett.* **95** 046802
[64] Bozhevilnyi S I, Volkov V S, Devaux E, J.Y. Laluet and Ebbesen T W 2006 *Nature* **440** 508
[65] Krasavin A V and Zheludev N I 2004 *Appl. Phys. Lett.* **84** 1416
[66] Krasavin A V, Zayats A V and Zheludev N I 2005 *J. Opt. A: Pure Appl. Opt.* **7** S85
[67] Andrew P and Barnes W L 2004 *Science* **306** 1002
[68] Ferrell R A 1958 *Phys. Rev.* **111** 1214
[69] Brown R W, Wessel P and Trounson E P 1960 *Phys. Rev. Lett.* **5** 472
[70] Arakawa E T, Herickhoff R J and Birkhoff R D 1964 *Phys. Rev. Lett.* **12** 319
[71] Donohue J F and Wang E Y 1986 *J. Appl. Phys.* **59** 3137
Donohue J F and Wang E Y 1987 **62** 1313
[72] Teng Y-Y and Stern E A 1967 *Phys. Rev. Lett.* **19** 511
[73] Otto A 1968 *Z. Phys.* **216** 398
[74] Kretschmann E and Raether H 1968 *Z. Naturf.* A **23** 2135
[75] Bruns R and Raether H 1970 *Z. Phys.* **237** 98
[76] Kretschmann E 1971 *Z. Phys.* **241** 313
[77] Mills D L and Burstein E 1974 *Rep. Prog. Phys.* **37** 817
[78] Agranovich V M and Mills D L (ed) 1982 *Surface Polaritons* (Amsterdam: North-Holland)
[79] Boardman A D (ed) 1982 *Electromagnetic Surface Modes* (New York: Wiley)
[80] Sambles J R, Bradbery G W and Yang F Z 1991 *Contemp. Phys.* **32** 173
[81] Zayats A V and Smolyaninov I I 2003 *J. Opt. A: Pure Appl. Opt.* **5** S16
[82] Ritchie R H *PhD Thesis* 1959 University of Tennessee (unpublished)
Ritchie R H 1963 *Prog. Theor. Phys.* **29** 607
[83] Kanazawa H 1961 *Prog. Theor. Phys.* **26** 851
[84] Bennett A J 1970 *Phys. Rev.* B **1** 203
[85] Feibelman P J 1971 *Phys. Rev.* B **3** 220
[86] Harris J and Griffin A 1971 *Phys. Lett.* A **34** 51
[87] Flores F and García-Moliner F *Solid State Commun.* **11** 1295
García-Moliner F and Flores F 1979 *Introduction to the Theory of Solid Surfaces* (Cambridge: Cambridge University Press)
[88] Beck D E 1971 *Phys. Rev.* B **4** 1555
[89] Beck D E and Celli V 1972 *Phys. Rev. Lett.* **28** 1124
[90] Inglesfield J E and Wikborg E 1973 *J. Phys. C: Solid State Phys.* **6** L158
Inglesfield J E and Wikborg E 1974 *Solid State Commun.* **14** 661
[91] Lang N D and Kohn W 1970 *Phys. Rev.* B **1** 4555
Lang N D and Kohn W 1971 *Phys. Rev.* B **3** 1215
[92] Feibelman P J 1973 *Phys. Rev. Lett.* **30** 975
Feibelman P J 1974 *Phys. Rev.* B **9** 5077
Feibelman P J 1975 *Phys. Rev.* B **12** 1319
[93] Kunz C 1966 *Z. Phys.* **196** 311
[94] Bagchi A, Duke C B, Feibelman P J and Porteus J O 1971 *Phys. Rev. Lett.* **27** 998
[95] Duke C B, Pietronero L, Porteus J O and Wendelken J F 1975 *Phys. Rev.* B **12** 4059
[96] Kloos T and Raether H 1973 *Phys. Lett.* A **44** 157
[97] Krane K J and Raether H 1976 *Phys. Rev. Lett.* **37** 1355
[98] Tsuei K-D, Plummer E W and Feibelman P J 1989 *Phys. Rev. Lett.* **63** 2256
[99] Tsuei K-D, Plummer E W, Liebsch A, Kempa K and Bakshi P 1990 *Phys. Rev. Lett.* **64** 44
[100] Tsuei K-D, Plummer E W, Liebsch A, Pehlke E, Kempa K and Bakshi P 1991 *Surf. Sci.* **247** 302
[101] Sprunger P T, Watson G M and Plummer E W 1992 *Surf. Sci.* **269–270** 551
[102] Hohenberg P and Kohn W 1964 *Phys. Rev.* **136** B864
Kohn W and Sham L J 1965 *Phys. Rev.* **140** A1133
[103] Liebsch A 1987 *Phys. Rev.* B **36** 7378
[104] Contini R and Layet J M 1987 *Solid State Commun.* **64** 1179
[105] Suto S, Tsuei K-D, Plummer E W and Burstein E 1989 *Phys. Rev. Lett.* **63** 2590
Lee G, Sprunger P T, Plummer E W and Suto S 1991 *Phys. Rev. Lett.* **67** 3198
Lee G, Sprunger P T and Plummer E W 1993 *Surf. Sci.* **286** L547
[106] Rocca M and Valbusa U 1990 *Phys. Rev. Lett.* **64** 2398
Rocca M, Lazzarino M and Valbusa U 1991 *Phys. Rev. Lett.* **67** 3197

Rocca M, Lazzarino M and Valbusa U 1992 *Phys. Rev. Lett.* **69** 2122
[107] Moresco F, Rocca M, Zielasek V, Hildebrandt T and Henzler M 1997 *Surf. Sci.* **388** 1
Moresco F, Rocca M, Zielasek V, Hildebrandt T and Henzler M 1997 *Surf. Sci.* **388** 24
[108] Kim B-O, Lee G, Plummer E W, Dowben P A and Liebsch A 1995 *Phys. Rev.* B **52** 6057
[109] Tarriba J and Mochán W L 1992 *Phys. Rev.* B **46** 12902
[110] Feibelman P J 1993 *Surf. Sci.* **282** 129
Feibelman P J 1994 *Phys. Rev. Lett.* **72** 788
[111] Liebsch A 1993 *Phys. Rev. Lett.* **71** 145
Liebsch A 1993 *Phys. Rev.* B **48** 11317
Liebsch A *Phys. Rev. Lett.* **72** 789
[112] Liebsch A and Schaich W L 1995 *Phys. Rev.* B **52** 14219
[113] López-Bastidas C and Mochán W L 1999 *Phys. Rev.* B **60** 8348
[114] López-Bastidas C, Liebsch A and Mochán W L 2001 *Phys. Rev.* B **63** 165407
[115] Campillo I, Rubio A and Pitarke J M 1999 *Phys. Rev.* B **59** 12188
[116] Cazalilla M A, Dolado J S, Rubio A and Echenique P M 2000 *Phys. Rev.* B **61** 8033
[117] Gurtubay I G, Pitarke J M, Campillo I and A. Rubio 2001 *Comput. Mater. Sci.* **22** 123
[118] Silkin V M, Chulkov E V and Echenique P M 2004 *Phys. Rev. Lett.* **93** 176801
[119] Silkin V M and Chulkov E V 2006 *Vacuum* **81** 186
[120] Moresco F, Rocca M, Zielasek V, Hildebrandt T and Henzler M 1996 *Phys. Rev.* B **54** R14333
[121] Liebsch A 1998 *Phys. Rev.* B **57** 3803
[122] Levinson H J, Plummer E W and Feibelman P 1979 *Phys. Rev. Lett.* **43** 952
[123] Barman S R, Häberle P and Horn K 1998 *Phys. Rev.* B **58** R4285
[124] Barman S R, Biswas C and Horn K 2004 *Phys. Rev.* B **69** 045413
[125] Silkin V M, García-Lekue A, Pitarke J M, Chulkov E V, Zaremba E and Echenique P M 2004 *Europhys. Lett.* **66** 260
[126] Silkin V M, Pitarke J M, Chulkov E V and Echenique P M 2005 *Phys. Rev.* B **72** 115435
[127] Pitarke J M, Nazarov V U, Silkin V M, Chulkov E V, Zaremba E and Echenique P M 2004 *Phys. Rev.* B **70** 205403
[128] Diaconescu B, Pohl K, Vattuone L, Savio L, Hofmann P, Silkin V, Pitarke J M, Chulkov E, Echenique P M, Farias D and Rocca M submitted
[129] See, e.g. Bohren C F and Huffman D R 1983 *Absorption and Scattering of Light by Small Particles* (New York: Wiley)
[130] Batson P E 1982 *Phys. Rev. Lett.* **49** 936
[131] Howie A and Milne R H 1985 *Ultramicroscopy* **18** 427
[132] Ferrell T L and Echenique P M 1985 *Phys. Rev. Lett.* **55** 1526
[133] Rivacoba A Zabala N and Echenique P M 1992 *Phys. Rev. Lett.* **69** 3362
[134] McComb D W and Howie A 1995 *Nucl. Instrum. Methods* B **96** 569
[135] Rivacoba A, Zabala N and Aizpurua J 2000 *Prog. Surf. Sci.* **65** 1
[136] Klar T, Perner M, Grosse S, von Plessen G, W. Spirkl and Feldmann J 1998 *Phys. Rev. Lett.* **80** 4249
[137] Shipway A N, Katz E and Willner I 2000 *Chem. Phys. Chem.* **1** 18
[138] Lucas A A, Henrard L and Ph. Lambin 1994 *Phys. Rev.* B **49** 2888
[139] de Heer W A, Bacsa W S, Châtelain A, Gerfin T, R. Humphrey-Baker, Forro L and Ugarte D 1995 *Science* **268** 845
[140] García-Vidal F J, Pitarke J M and Pendry J B 1997 *Phys. Rev. Lett.* **78** 4289
Pitarke J M and García-Vidal F J 2001 *Phys. Rev.* B **63** 73404
García-Vidal F J and Pitarke J M 2001 *Eur. Phys. J.* B **22** 257
[141] García-Vidal F J and Pendry J B 1996 *Phys. Rev. Lett.* **77** 1163
García-Vidal F J and Pendry J B 1995 *Prog. Surf. Sci.* **50** 55
[142] García-Vidal F J, Pitarke J M and Pendry J B 1998 *Phys. Rev.* B **58** 6783
[143] Inglesfield J E, Pitarke J M and Kemp R 2004 *Phys. Rev.* B **69** 233103
Pitarke J M and Inglesfield J E submitted
[144] Aruga T and Murata Y 1989 *Prog. Surf. Sci.* **31** 61
[145] Liebsch A 1991 *Phys. Rev. Lett.* **67** 2858
[146] Ishida H and Liebsch A 1992 *Phys. Rev.* B **45** 6171
[147] Kim J-S, Chen L, Kesmodel L L and Liebsch A 1997 *Phys. Rev.* B **56** R4402
[148] Barman S R, Horn K, Häberle P, Ishida H and Liebsch A 1998 *Phys. Rev.* B **57** 6662
[149] Ishida H and Liebsch A 1998 *Phys. Rev.* B **57** 12550
[150] Ishida H and Liebsch A 1998 *Phys. Rev.* B **57** 12558

[151] Liebsch A, Kim B-O and Plummer W 2001 *Phys. Rev.* B **63** 125416
[152] Zielasek V, Rönitz N, Henzler M and Pfnür H 2006 *Phys. Rev. Lett.* **96** 196801
[153] Dobson J F 1992 *Phys. Rev.* B **46** 10163
Dobson J F 1993 *Aust. J. Phys.* **46** 391
[154] Schaich W L and Dobson J F 1994 *Phys. Rev.* B **49** 14700
[155] Zaremba E and Tso H C 1994 *Phys. Rev.* B **49** 8147
[156] Guo Q, Feng Y P, Poon H C and Ong C K 1996 *J. Phys.: Condens. Matter* **8** 9037
[157] Tokatly I V and Pankratov O 2002 *Phys. Rev.* B **66** 153103
[158] See, e.g. Parker E H C (ed) 1985 *The Technology and Physics of Molecular Beam Epitaxy* (New York: Plenum)
[159] Dempsey J and Halperin B I 1992 *Phys. Rev.* B **45** 1719
[160] Monarkha Y P, Teske E and Wyder P 2002 *Phys. Rep.* **370** 1
[161] Ritchie R H 1973 *Surf. Sci.* **34** 1
[162] Feibelman P J 1982 *Prog. Surf. Sci.* **12** 287
[163] See, e.g. Liebsch A 1997 *Electronic Excitations at Metal Surfaces* (New York: Plenum)
[164] Raether H 1980 *Excitation of Plasmons and Interband Transitions by Electrons* (*Springer Tracks in Modern Physics* vol 88) (New York: Springer)
[165] Raether H 1988 *Surface Plasmons on Smooth and Rough Surfaces and on Gratings* (*Springer Tracks in Modern Physics*) vol 111 (New York: Springer)
[166] Plummer W, Tsuei K-D and Kim B-O 1995 *Nucl. Instrum. Methods* B **96** 448
[167] Rocca M 1995 *Surf. Sci. Rep.* **22** 1
[168] Kushwaha M S 2001 *Surf. Sci. Rep.* **41** 1
[169] Jackson J D 1962 *Classical Electrodynamics* (New York: Wiley)
[170] Ritchie R H and Eldridge H B 1962 *Phys. Rev.* **126** 1935
[171] Ashcroft N W and Mermin N D 1976 *Solid State Physics* (Philadelphia: Saunders)
[172] Pettit R B, Silcox J and Vincent R 1975 *Phys. Rev.* B **11** 3116
[173] Stern F 1967 *Phys. Rev. Lett.* **18** 546
Ando T, Fowler A B and Stern F 1982 *Rev. Mod. Phys.* **54** 437
[174] Allen S J Jr, Tsui D C and Logan R A 1977 *Phys. Rev. Lett.* **38** 980
[175] Nagao T, Heldebrandt T, Henzler M and Hasegawa S 2001 *Phys. Rev. Lett.* **86** 5747
[176] See, e.g. Lundqvist S 1983 in *Theory of the Inhomogeneous Electron Gas* ed S Lundqvist and N H March (New York: Plenum) p 149
[177] Ritchie R H and Wilems R E 1969 *Phys. Rev.* **178** 372
[178] Barton G 1979 *Rep. Prog. Phys.* **42** 65
[179] Wagner D 1966 *Z. Naturf.* a **21** 634
[180] Ritchie R H and Marusak A L 1966 *Surf. Sci.* **4** 234
[181] Schmeits M 1989 *Phys. Rev.* B **39** 7567
[182] Pitarke J M, Pendry J B and Echenique P M 1997 *Phys. Rev.* B **55** 9550
[183] Pitarke J M and Rivacoba A 1997 *Surf. Sci.* **377–379** 294
[184] See, e.g. Bergman D J and Stroud D 1992 *Solid State Phys.* **46** 147
[185] Fuchs R 1974 *Phys. Lett.* A **48** 353
[186] Fuchs R 1975 *Phys. Rev.* B **11** 1732
[187] Ouyang F and Isaacson M 1989 *Phil. Mag.* B **60** 481
[188] Ouyang F and Isaacson M 1989 *Ultramicroscopy* **31** 345
[189] Lu J Q and Maradudin A A 1990 *Phys. Rev.* B **42** 11159
[190] Goloskie R, Thio T and Ram-Mohan L R 1996 *Comput. Phys.* **10** 477
[191] García de Abajo F J and Aizpurua J 1997 *Phys. Rev.* B **56** 15873
[192] Aizpurua J, Howie A and García de Abajo F J 1999 *Phys. Rev.* B **60** 11149
[193] García de Abajo F J and Howie A 1998 *Phys. Rev. Lett.* **80** 5180
[194] Bergman D J 1978 *Phys. Rep.* **43** 377
[195] Milton G 1981 *J. Appl. Phys.* **52** 5286
[196] Yablonovitch E, Gmitter T J, Meade R D, Rappe A M, Brommer K D and Joannopoulos J D 1991 *Phys. Rev. Lett.* **67** 3380
[197] Ho K M, Chan C T and Soukoulis C M 1990 *Phys. Rev. Lett.* **65** 3152
[198] Pendry J B and MacKinnon A 1992 *Phys. Rev. Lett.* **69** 2772
[199] Inglesfield J E 1998 *J. Phys. A: Math. Gen.* **31** 8495
Kemp R and Inglesfield J E 2002 *Phys. Rev.* B **65** 115103
[200] García de Abajo F J 1999 *Phys. Rev.* B **59** 3095
[201] English R A, Pitarke J M and Pendry J B 2000 *Surf. Sci.* **454–456** 1090

[202] Pitarke J M, García-Vidal F J and Pendry J B 1998 *Phys. Rev.* B **57** 15261
[203] Pitarke J M, García-Vidal F J and Pendry J B 1999 *Surf. Sci.* **433–435** 605
[204] Yannopapas V, Modinos A and Stefanou N 1999 *Phys. Rev.* B **60** 5359
[205] Riikonen S, Romero I and García de Abajo F J 2005 *Phys. Rev.* B **71** 235104
[206] Apell S P, Echenique P M and Ritchie R H 1995 *Ultramicroscopy* **65** 53
[207] Ronveaux A, Moussiaux A and Lucas A A 1977 *Can. J. Phys.* **55** 1407
[208] Östling D, Apell P and Rosén A 1993 *Europhys. Lett.* **21** 539
[209] Pines D and Nozieres 1989 *The Theory of Quantum Liquids* (New York: Addison-Wesley)
[210] Fetter A L and Walecka J D 1971 *Quantum Theory of Many-Particle Systems* (New York: McGraw-Hill)
[211] Callen H B and Welton T A 1951 *Phys. Rev.* **83** 34
[212] See, e.g. Gross E K U and Kohn W 1990 *Adv. Quantum Chem.* **21** 255
[213] Zangwill A and Soven P 1980 *Phys. Rev.* A **21** 1561
[214] Ullrich C A, Gossmann U J and Gross E K U 1995 *Phys. Rev. Lett.* **74** 872
[215] Petersilka M, Gossmann U J and Gross E K U 1996 *Phys. Rev. Lett.* **76** 1212
[216] Burke K, Petersilka M and Gross E K U 2000 A hybrid functional for the exchange-correlation kernel in time-dependent density functional theory *Recent Advances in Density Functional Methods* vol III, ed P Fantucci and A Bencini (Singapore: World Scientific)
[217] Pitarke J M and Perdew J P 2003 *Phys. Rev.* B **67** 045101
[218] Jung J, García-González P, Dobson J F and R. Godby W 2004 *Phys. Rev.* B **70** 205107
[219] Hubbard J 1958 *Proc. R. Soc. Lond. Ser.* A **243** 336
[220] Singwi K S, Tosi M P, Land R H and Sjölander A 1968 *Phys. Rev.* **176** 589
Singwi K S, Sjölander A, Tosi M P and Land R H 1970 *Phys. Rev.* B **1** 1044
[221] Vashishta P and Singwi K S 1972 *Phys. Rev.* B **6** 875
[222] Singwi K S and Tosi M P 1981 *Solid State Phys.* **36** 177
[223] Ichimaru S 1982 *Rev. Mod. Phys.* **54** 1017
[224] Iwamoto N and Pines D 1984 *Phys. Rev.* B **29** 3924
[225] Engel E and Vosko S H 1990 *Phys. Rev.* B **42** 4940
[226] Khodel V A, Shaginyan V R and Khodel V V 1994 *Phys. Rep.* **249** 1
[227] Bowen C, Sugiyama G and Alder B J 1994 *Phys. Rev.* B **50** 14838
[228] Moroni S, Ceperley D M and Senatore G 1995 *Phys. Rev. Lett.* **75** 689
[229] Corradini M, Del Sole R 1987 Onida G and Palummo M 1998 *Phys. Rev.* B **57** 14569
[230] Gross E K U and Kohn W 1985 *Phys. Rev. Lett.* **55** 2850
[231] Iwamoto N and U E K Gross. *Phys. Rev.* B **35** 3003
[232] Vignale G and Kohn W 1996 *Phys. Rev. Lett.* **77** 2037
[233] Vignale G, Ullrich C A and Conti S 1997 *Phys. Rev. Lett.* **79** 4878
[234] Nifosi R, Conti S and Tosi M P 1998 *Phys. Rev.* B **58** 12758
[235] Qian Z and Vignale G 2002 *Phys. Rev.* B **65** 235121
[236] Brosens F, Lemmens L F and Devreese J T 1976 *Phys. Status Solidi* B **74** 45
[237] Devreese J T, Brosens F and Lemmens L F 1980 *Phys. Rev.* B **21** 1349
Brosens F, Devreese J T and Lemmens L F 1980 *Phys. Rev.* B **21** 1363
[238] Richardson C F and Ashcroft N W 1994 *Phys. Rev.* B **50** 8170
[239] Sturm K and Gusarov A 2000 *Phys. Rev.* B **62** 16474
[240] Echenique P M, Bausells J and Rivacoba A 1987 *Phys. Rev.* B **35** 1521
[241] Abramowitz M and Stegun I A 1964 *Handbook of Mathematical Functions* (New York: Dover)
[242] Barrera R G and Fuchs R 1995 *Phys. Rev.* B **52** 3256
[243] Bergara A, Pitarke J M and Ritchie R H 1999 *Phys. Lett.* A **256** 405
[244] Lindhard J 1954 *K. Dan. Vidensk. Selsk. Mat.-Fys. Medd.* **28** 1
[245] García-Lekue A and Pitarke J M 2001 *Phys. Rev.* B **64** 035423
García-Lekue A and Pitarke J M 2003 *Phys. Rev.* B **67** 089902(E)
García-Lekue A and Pitarke J M *Nucl. Instrum. Methods* B **182** 56
[246] See, e.g. Lang N 1973 *Solid State Phys.* **28** 225
[247] Reuter G E H and Sonheimer E H 1948 *Proc. R. Soc. Lond. Ser.* A **195** 336
Griffin A and Harris J 1976 *Can. J. Phys.* **54** 1396
[248] Chulkov E V, Silkin V M and Echenique P M 1997 *Surf. Sci.* **391** L1217
Chulkov E V, Silkin V M and Echenique P M 1999 *Surf. Sci.* **437** 330
[249] Chulkov E V, Sarria I, Silkin V M, Pitarke J M and Echenique P M 1998 *Phys. Rev. Lett.* **80** 4947
[250] Echenique P M, Pitarke J M, Chulkov E V and Rubio A 2000 *Chem. Phys.* **251** 1
[251] Kliewer J, Berndt R, Chulkov E V, Silkin V M, Echenique P M and Crampin S 2000 *Science* **288** 1399

[252] Echenique P M, Osma J, Silkin V M, Chulkov E V and Pitarke J M 2000 *Appl. Phys.* A **71** 503
Echenique P M, Osma J, Machado M, Silkin V M, Chulkov E V and Pitarke J M 2001 *Prog. Surf. Sci.* **67** 271
[253] Eiguren A, Hellsing B, Reinert F, Nicolay G, Chulkov E V, Silkin V M, Hüfner S and Echenique P M 2002 *Phys. Rev. Lett.* **88** 066805
[254] Echenique P M, Berndt R, Chulkov E V, Th. Fauster, A. Goldmann and Höfer U 2004 *Surf. Sci. Rep.* **52** 219
[255] Crampin S 2005 *Phys. Rev. Lett.* **95** 046801
[256] Vergniory M G, Pitarke J M and Crampin S 2005 *Phys. Rev.* B **72** 193401
[257] Persson B N J and Zaremba E 1984 *Phys. Rev.* B **30** 5669
[258] Ibach H and Mills D L 1982 *Electron Energy Loss Spectroscopy and Surface Vuvrations* (New York: Academic)
[259] Mills D L 1975 *Surf. Sci.* **48** 59
[260] Gaspar J A, Eguiluz A G, Tsuei K-D and Plummer E W 1991 *Phys. Rev. Lett.* **67** 2854
[261] Forstmann F and Stenschke H 1978 *Phys. Rev.* B **17** 1489
[262] Feibelman P J 1989 *Phys. Rev.* B **40** 2752
Feibelman P J and Tsuei K D 1990 *Phys. Rev.* B **41** 8519
[263] Kempa K and Schaich W L 1988 *Phys. Rev.* B **37** 6711
[264] Chiarello G, Formoso V, Santaniello A, Colavita E and Papagno L 2000 *Phys. Rev.* B **62** 12676
[265] Eguiluz A G 1983 *Phys. Rev. Lett.* **51** 1907
Eguiluz A G 1985 *Phys. Rev.* B **31** 3303
[266] Marušić L, Despoja V and Šunjić M 2006 *J. Phys.: Condens. Matter* **18** 4253
[267] Nazarov V U, Nishigaki S and Nagao T 2002 *Phys. Rev.* B **66** 092301
[268] Beck D E and Dasgupta B B 1975 *Phys. Rev.* B **12** 1995
[269] Eguiluz A, Ying S C and Quinn J J 1975 *Phys. Rev.* B **11** 2118
[270] Eguiluz A G and Quinn J J 1976 *Phys. Rev.* B **14** 1347
[271] Schwartz C and Schaich W L 1982 *Phys. Rev.* B **26** 7008
[272] Ahlqvist P and Apell P 1982 *Phys. Scr.* **25** 587
[273] Schwartz C and Schaich W L 1984 *Phys. Rev.* B **30** 1059
[274] Dobson J F and Harris G H 1988 *J. Phys. C: Solid State Phys.* **21** L729
Dobson J J, Harris G H and O'Connor A J 1990 *J. Phys.: Condens. Matter* **2** 6461
[275] Nazarov V U and Nishigaki S 2001 *Surf. Sci.* **482** 640
[276] Sellarés J and Barberán N 1994 *Phys. Rev.* B **50** 1879
[277] Monin J and Boutry G-A 1974 *Phys. Rev.* B **9** 1309
[278] Perdew J P, Tran H Q and Smith E D 1990 *Phys. Rev.* B **42** 11627
[279] Shore H B and Rose J H 1991 *Phys. Rev. Lett.* **66** 2519
Rose J H and Shore H B 1991 *Phys. Rev.* B **43** 11605
Shore H B and Rose J H 1999 *Phys. Rev.* B **59** 10485
[280] Ishida H and Liebsch A 1996 *Phys. Rev.* B **54** 14127
[281] Rocca M, Lizzit S, Brena B, Cautero G, Comelli G and Paolucci G 1995 *J. Phys.: Condens. Matter* **7** L611
[282] Johnson P B and Christy R W 1972 *Phys. Rev.* B **6** 4370
[283] López-Bastidas C, Maytorena J A and Liebsch A 2002 *Phys. Rev.* B **65** 035417
[284] Moresco F, Rocca M, Hildebrandt T, Zielasek V and Henzler M 1998 *Europhys. Lett.* **43** 433
[285] Savio L, Vattuone L and Rocca M 2000 *Phys. Rev.* B **61** 7324
[286] Savio L, Vattuone L and Rocca M 2003 *Phys. Rev.* B **67** 045406
[287] Vehse R C, Arakawa E T and Williams M W 1970 *Phys. Rev.* B **1** 517
[288] Inglesfield J E 1982 *Rep. Prog. Phys.* **45** 223
[289] Chulkov E V, Silkin V M and Shirykalov E N 1987 *Surf. Sci.* **188** 287
[290] Chaplik A V 1972 *Zh. Eksp. Teor. Fiz.* **62** 746 (*Sov. Phys.—JETP* **35** 395)
[291] Das Sarma S and Madhukar A 1981 *Phys. Rev.* B **23** 805
[292] Silkin V M, Balasubramanian T, Chulkov E V, Rubio A and Echenique P M 2001 *Phys. Rev.* B **64** 085334
[293] Pitarke J M, Silkin V M, Chulkov E V and Echenique P M 2005 *J. Opt. A.: Pure Appl. Opt.* **7** S73
[294] Pitarke J M and Campillo I 2000 *Nucl. Instrum. Methods* B **164** 147
[295] Hedin L and Lundqvist S 1969 *Solid State Phys.* **23** 1
[296] Milne R H and Echenique P M 1985 *Solid State Commun.* **55** 909
[297] Nuñez R, Echenique P M and Ritchie R H 1980 *J. Phys. C: Solid State Phys.* **13** 4229
[298] Yubero F and Tougaard S 1992 *Phys. Rev.* B **46** 2486
[299] Chen Y F and Chen Y T 1996 *Phys. Rev.* B **53** 4980
[300] Juaristi J I, García de Abajo F J and Echenique P M 1996 *Phys. Rev.* B **53** 13839
[301] Ding Z J 1997 *Phys. Rev.* B **55** 9999
Ding Z J 1998 *J. Phys.: Condens. Matter* **10** 1733

Ding Z J 1998 *J. Phys.: Condens. Matter* **10** 1753
[302] Nagatomi T, Shimizu R and Ritchie R H 1999 *Surf. Sci.* **419** 158
[303] Song Y H, Wang Y N and Miskovic Z L 2001 *Phys. Rev.* A **63** 052902
[304] Tökési K, Tong X-M, Lemell C and Burgdörfer J 2005 *Phys. Rev.* A **72** 022901
[305] Alducin M, Silkin V M, Juaristi J I and Chulkov E V 2003 *Phys. Rev.* A **67** 032903
[306] Campillo I, Pitarke J M and Eguiluz A G 1998 *Phys. Rev.* B **58** 10307
Campillo I, Pitarke J M, Eguiluz A G and Garcí a A 1998 *Nucl. Instrum. Methods* B **135** 103
Campillo I and Pitarke J M 2000 *Nucl. Instrum. Methods* B **164** 161
[307] Mathar R J, Sabin J R and Trickey S B 1999 *Nucl. Instrum. Methods* B **155** 249
[308] García-Vergniory M, Gurtubay I G, Silkin V M and Pitarke J M in preparation
[309] Gemmell D S 1974 *Rev. Mod. Phys.* **46** 129
[310] Kimura K, Hasegawa M and Mannami M 1987 *Phys. Rev.* B **36** 7
[311] Fuji Y, Fujiwara S, Narumi K, Kimura K and Mannami M 1992 *Surf. Sci.* **277** 164
Kimura K, Kuroda H, Fritz M and Mannami M 1992 *Surf. Sci.* **277** 164
Kimura K, Kuroda H, Fritz M and Mannami M 1995 *Nucl. Instrum. Methods* B **100** 356
[312] Winter H, Wilke M and Bergomaz M 1997 *Nucl. Instrum. Methods* B **125** 124
[313] Robin A, Hatke N, Närmann A, Grether M, Plackhe D, Jensen J and Heiland W 2000 *Nucl. Instrum. Methods* B **164** 566
[314] Winter H 2002 *Phys. Rep.* **367** 387
[315] Cazalilla M A and Juaristi J I 1999 *Nucl. Instrum. Methods* B **157** 104
[316] Garcí a-Lekue A and Pitarke J M 2003 *J. Electron. Spectrosc.* **129** 223
[317] Berger S D, Bruley J, Brown L M and McKenzie D R 1989 *Ultramicroscopy* **28** 43
[318] Lecante J, Ballu Y and Newns D M 1977 *Phys. Rev. Lett.* **38** 36
[319] Warmack R J, Becker R S, Anderson V E, Ritchie R H, Chu Y T, Little J and Ferrell T 1984 *Phys. Rev.* B **29** 4375
[320] Ritchie R H and Howie A 1988 *Phil. Mag.* A **58** 753
[321] Kohl H and Rose H 1985 *Adv. Electron. Electron Phys.* **65** 173
[322] Cohen H, Maniv T, Tenne R, Rosenfeld Hacohen Y, Stephan O and Colliex C 1998 *Phys. Rev. Lett.* **80** 782
Echenique P M, Howie A and Ritchie R H 1999 *Phys. Rev. Lett.* **83** 658
Cohen H, Maniv T, Tenne R, Rosenfeld Hacohen Y, Stephan O and Colliex C 1999 *Phys. Rev. Lett.* **83** 659
[323] Rivacoba A and Echenique P M 1990 *Scanning Microsc.* **4** 73
[324] Okamoto K, Niki I, Scherer A, Narukawa Y, Mukai T and Kawakami Y 2005 *Appl. Phys. Lett.* **87** 071102
[325] Wedge S, Wasey J A E, Barnes W L and Sage I 2004 *Appl. Phys. Lett.* **85** 182
[326] Thio T, Pellerin K M, Linke R A, Lezec H J and Ebbesen T W 1972 *Opt. Lett.* **26** 1972
[327] Pendry J B, Martin-Moreno L and Garcia F J-Vidal 2004 *Science* **305** 847
[328] Barnes W L, Murray W A, Dintinger J, Devaux E and T. W. Ebbesen 2004 *Phys. Rev. Lett.* **92** 107401
[329] Beruete M, Sorolla M, Campillo I, Dolado J S, Martin-Moreno L, Bravo-Abad J and García-Vidal F J 2004 *Opt. Lett.* **29** 2500
[330] Akarca-Biyikli S S, Bulu I and Ozbay E 2004 *Appl. Phys. Lett.* **85** 1098
[331] Cao H and Nahata A 2004 *Opt. Express* **12** 3664
[332] Kik P G, Maier S A and Atwater H A 2004 *Phys. Rev.* B **69** 045418
[333] Luoa X and Ishihara T 2004 *Appl. Phys. Lett.* **84** 4780
[334] Shao D B and Chen S C 2005 *Appl. Phys. Lett.* **86** 253107
[335] Wang L, Uppuluri S M, Jin E X and Xu X F 2006 *Nano Lett.* **6** 361
[336] Pendry J B 2000 *Phys. Rev. Lett.* **85** 3966
[337] Taubner T, Korobkin D, Urzhumov Y, Shvets G and Hillenbrand R 2006 *Science* **313** 1595